Department of Physics and Astronomy
University of Heidelberg

Master thesis in Physics
submitted by

Nikolai Bolik

born in Aachen

2024

Decoherence and Dissipation in Open Quantum Systems

This Master thesis has been carried out by
Nikolai Bolik
at the
Institute for Theoretical Physics in Heidelberg
under the supervision of
Sandro Wimberger

First referee: Luca Amendola
Second referee: Sandro Wimberger

Abstract

The study of open quantum systems is crucial for understanding physics under realistic conditions given by the interaction of quantum mechanical systems with their environment. This thesis investigates the dynamics of two distinct open quantum systems, consisting of ultracold atoms in optical lattices. First, we explore symmetry properties in atom optics kicked rotor quantum walks influenced by spontaneous emissions (SE). We demonstrate that SE induces asymmetries in otherwise symmetric quantum walks. This finding is particularly interesting as it changes the typical perspective on SE, which is generally considered a nuisance. In our study, SE enables the formation of a quantum walk ratchet, illustrating how seemingly adverse effects can be beneficial under specific conditions. Second, we examine the open Bose-Hubbard model, representing a true many-body system interacting not only with its environment but also internally. This introduces significant complexity making the analysis of large interacting systems numerically infeasible. To address these challenges, we discuss the truncated Wigner method and aim to extend this methodology beyond its typical approximations.
The connection between these two studies lies in their open nature and their common experimental implementation in optical lattices: The atom optics kicked rotor describes non-interacting atoms, where each atom interacts with the environment but not with each other, while the Bose-Hubbard model deals with a true many-particle system, requiring a different analytical approach. This dual investigation enhances our understanding of dissipation in open quantum systems, improving our ability to model and interpret complex quantum phenomena under realistic conditions, such as decoherence, dissipation, and particle loss.

Die Auseinandersetzung mit offenen Quantensystemen ist entscheidend für unser Verständnis der Physik unter Annahme realistischer Bedingungen. Diese Bedingungen ergeben sich aus der Wechselwirkung quantenmechanischer Systeme mit ihrer Umwelt. Diese Studie untersucht zwei verschiedene offene Systeme; Zunächst untersuchen wir die Symmetrieeigenschaften von Quanten-Walks im „atom optics kicked rotor“ unter dem Einfluss von SE. Wir zeigen, dass diese SE induzierten Asymmetrien in ansonsten symmetrischen Walks auftreten. Dies ist ein vielversprechendes Ergebnis, da es Spontanemissionen (SE) aus einem anderen Blickwinkel betrachtet. Diese werden typischerweise als Rauschen in experimentellen Daten betrachtet. In unserer Arbeit jedoch zeigt sich, dass diese unter speziellen Bedingungen dazu genutzt werden können eine Quanten-Walk-Ratsche zu entwerfen. Somit zeigen wir, dass scheinbar nachteilige Effekte unter bestimmten Bedingungen von Vorteil sein können. Die Ergebnisse dieses Abschnitts wurden in unserem jüngsten Artikel publiziert [1].
Anschließend untersuchen wir das offene Bose-Hubbard-Modell, welches als echtes Vielteilchensystem nicht nur mit seiner Umgebung, sondern auch mit sich Selbst wechselwirkt. Dies steigert die Komplexität erheblich, wodurch die numerische Implementierung des Systems mit zunehmender Systemgröße schnell außer Reichweite gerät. Um uns dieser Problematik entgegenzuwirken, diskutieren wir die „truncated-Wigner“-Methode, mit dem Ziel diese über ihre üblichen Näherungen hinaus zu erweitern.
Der Zusammenhang zwischen den beiden Studien kommt durch die "Offenheit" beider Systeme und ihrer jeweiligen experimentellen implementierung in optischen Gittern. Der Kicked-Rotor beschreibt Atome, die mit ihrer Umwelt wechselwirken, intrinsisch aber keine Selbstwechselwirkung haben. Das offene Bose-Hubbard-Modell beschreibt dagegen ein echtes offenes Vielteilchensystem und erfordert durch seine Komplexität einen anderen Ansatz zur Lösung. Dieser Zweischritt stärt insgesamt unser Verständnis dissipativer Effekte in offenen Quantensystemen unter realistischen Konditionen, wie unter anderem Dekohärenz, Dissipation, oder Teilchenverlust.

Contents

1 Introduction

1.1 Motivation

The study of isolated quantum mechanical systems has provided profound insights into the fundamental nature of energy and matter. However, every real-world quantum system is imperfect and never truly isolated, but coupled to its external environment [1–9]. These interactions generally cause dissipation, decoherence, and energy exchange, which are beyond the framework of closed systems. The study of *open quantum systems* focuses on understanding these interactions and their effects on the system's dynamics, which is essential for theoretical and practical advancements in fields such as quantum optics or quantum computing [10–14].
Quantum systems in a Bose-Einstein condensate (BEC) represent quantum gases collapsed into a singular quantum state. When the interaction between atoms in this state is sufficiently weak, the system can be described mathematically by neglecting interactions altogether [2, 8, 9]. However, as the interaction strength increases, the system's description becomes more complex, necessitating different mathematical approaches [7, 14, 15].
In this study, we explore both interaction regimes by discussing two distinct systems that are both experimentally realized in optical lattices. The open nature of the system can significantly alter its overall behavior, compared to a closed system not interacting with its environment [1,7]. In the regime of negligible atom-atom interaction, we investigate how spontaneous emissions (SE), which represent the interaction of the system with its environment, transform the dynamics in the system [1]. Notably, we observe that this source of dissipation can be beneficial in certain scenarios, such as designing Parrondo-like games [16]. In the presence of interactions within the quantum gas, the introduction of dissipation may also change the system dynamics [7].
For the numerical investigation of this type of system, approximative methods become essential. We focus on understanding and improving the truncated-Wigner approach, which may be valuable for future studies of open quantum systems and enhance our understanding of these complex systems.
The open systems of interest find their experimental implementation in optical lattices. These are periodic potentials created by the interference pattern of intersecting laser beams, which can trap and manipulate ultracold atoms in a well-defined grid [17–20]. These lattices provide a fundamental platform for exploring quantum many-body systems.
When these systems are experimentally realized, their interaction with the environment leads to decoherence, which typically causes a nuisance in the data but can produce interesting effects under specific conditions [1,7]. Before delving into the investigation of open quantum systems in optical lattices, it is crucial to address how the fundamental dynamics of such open systems can be described.

1.2 Open Quantum Systems

A quantum system is considered to be "open" when it interacts with its surroundings. The open quantum system consists of a primary system of interest (S) interacting with an external environment (E). The total Hamiltonian of the combined system is given by:

$$H_{\text{total}} = H_S + H_E + H_{\text{int}}, \tag{1}$$

where H_S is the Hamiltonian of the system of interest, H_E is the Hamiltonian of the environment, and H_{int} represents the interaction between the system and the environment. The state of the total system is described by the density matrix ρ_{total}. The time evolution of the total system in the Schrödinger picture is captured by the Von-Neumann equation [14]:

$$\frac{d\rho_{\text{total}}}{dt} = -\frac{i}{\hbar}[H_{\text{total}}, \rho_{\text{total}}]. \tag{2}$$

To focus on the system S, we are interested in the reduced density matrix ρ_S. It is obtained by tracing out the environmental degrees of freedom:

$$\rho_S = \text{Tr}_E(\rho_{\text{total}}) \tag{3}$$

The evolution of ρ_S captures the influence of the environment on the system, leading to the necessity of a master equation that describes this evolution. The quantum optical master equation is fundamental in describing the dynamics of open quantum systems, with particular importance in quantum optics [1,6,7,21,22]. Several approximations are made for the derivation of this master equation [14, 15]:

- The Born approximation assumes weak coupling between the system and the environment, allowing to factorize the density matrix $\rho_{\text{total}} \approx \rho_S \otimes \rho_E$, where ρ_E is the density matrix of the environment.
- We assume that the environment has no memory, implying that the correlation time of the environment is much shorter than the timescale of the system's evolution. Thus, the system is described as a Markovian process.
- It is assumed that rapidly oscillating terms average out over time and are not contributing to the final equations.

With these approximations in place [14], the Lindblad form of the master equation my be derived. This equation describes the time evolution of the reduced density matrix ρ_S:

$$\frac{d\rho_S}{dt} = -\frac{i}{\hbar}[H_S, \rho_S] + \mathcal{D}[\rho_S] \tag{4}$$

where $\mathcal{D}$ is the dissipation operator, representing the dissipative processes:

$$\mathcal{D}[\rho_S] = \sum_i \left(L_i \rho_S L_i^\dagger - \frac{1}{2}\{L_i^\dagger L_i, \rho_S\} \right) \tag{5}$$

Here, L_i are the Lindblad operators that encapsulate various mechanisms of dissipation and decoherence, depending on the specific form of L_i. The quantum optical master equation is essential in understanding the behavior of quantum systems under realistic conditions. It allows us to model and predict the effects of interactions with the environment always present in every experimental situation. This understanding is crucial for developing quantum technologies, such as quantum computers and quantum communication systems [10–12], where controlling and mitigating decoherence and dissipation are essential for operational fidelity and efficiency. We are furthermore interested in the study of open quantum systems. Here, the quantum optical master equation provides the foundational framework for describing and understanding the complex dynamics of quantum systems on a theoretical level under realistic experimental conditions.

1.3 Outline

This thesis is divided into two main chapters, both circling around the dynamics of open quantum systems, both implemented in optical lattices [17–20];
The first chapter explores the dynamics of the atom optics kicked rotor (AOKR) quantum walks (QWs), which we have studied extensively in our previous work [4, 8, 9, 21]. Specifically, the symmetry properties of the walk are analyzed. The system describes a BEC which is periodically kicked by a short pulse of a standing wave laser. The interaction with the laser causes SE events. These interactions introduce dissipation to the system, however with interesting effects. We will show that moderate dissipation caused by SE changes the symmetry properties of specific quantum walks, opening the route for designing an open quantum walk ratchet. We have published the results of this chapter in our recent paper [1], which was written in the context of this thesis. The first chapter describes an open system, essentially in a single-particle picture. This means that the system is interacting with its surroundings, however the interaction between individual atoms in the system is sufficiently small that it can be neglected [19, 20]. In contrast, the second chapter investigates an open Bose-Hubbard model with dissipation, thus stretching our perspective to a many-body picture. We will delve into the semi-classical phase-space methodology of the truncated Wigner approach [7, 22–32], enabling enhanced numerical accessibility to this system. Understanding this method in detail did cost us significant time and effort. However, we aim to improve the approximations made in this approach. For both chapters, the quantum optical master equation will be the foundation for accessing the dissipative properties of the system.

2 First Chapter

2.1 Theoretical Background on Discrete-Time Quantum Walks

Over the past two decades, quantum walks (QWs) have garnered significant attention due to their potential applications to outperform classical algorithms in various computational tasks [10–12]. This has inspired us to dedicate a significant amount of work to this field [1, 2, 4, 8, 9, 21]. The unique characteristics of QWs arise from quantum interference phenomena. For instance, QWs typically exhibit two distinct peaks with ballistic expansion in opposite directions [10, 11]. This behavior contrasts to classical random walks that typically follow stochastic processes and show a normal distribution with diffusive expansion [33], or are power-law correlated in the walker space [34, 35]. In this context, a transition from quantum to classical behavior corresponds to a shift from a distribution featuring two ballistic peaks to one characterized by normal distribution and diffusive expansion.

The time representation itself can be continuous or discrete. In continuous-time models, time is represented as a continuum along the real number line, allowing events to occur at any arbitrary moment. In contrast, discrete-time models consider events to occur at distinct, separate intervals, analogous to the difference between an analog clock with continuously waving hands and a digital clock that jumps from one number to the next.

Random walk processes are typically classified as either continuous-time or discrete-time processes. The categorization between continuous-time and discrete-time walks accounts for both the classical case, but also the quantum mechanical counterpart [10]. Our investigations within this work focuses on discrete-time quantum walks. In these discrete-time processes, a sequence of random events occurs at distinct, discrete points in time. The discretization of time fundamentally affects the behavior and properties of the quantum walk, distinguishing it from its continuous-time counterpart [10]. The discrete-time variant notably introduces an additional coin degree of freedom, which determines the direction of the walker at each step. This added complexity makes the walks' dynamics an interesting subject for theoretical studies.

2.1.1 Quantum Walks

Quantum walks represent the quantum mechanical analog of classical random walks, extending the concept into the quantum domain. In classical random walks, a "walker" moves through a graph along a random path, making probabilistic decisions at each node about which subsequent node to visit. In the simplest example, a one-dimensional random walk on the integer set $\mathbb{Z}$, the walker decides to move left or right with balanced probability $p = 1/2$. The central limit theorem ensures that, over time, the probability distribution of such a walk converges to a Gaussian distribution, with diffusive expansion.

In contrast, quantum walks are described by a sequence of operators acting on a quantum state. For an in-depth introduction to quantum walks, we refer to Ref. [10]. In a quantum walk, the system can traverse all possible paths simultaneously due to the principle of superposition. This characteristic leads to interference effects, producing unique physical phenomena not present in classical walks, such as two ballistic peaks in the distribution.

The evolution of a quantum walk involves applying both a coin operator and a step operator. The quantum system must have an internal degree of freedom (DOF), such as spin, upon which the coin operator acts, and an external DOF, such as position or momentum, upon which the step operator acts. For instance, a system with an internal two-state DOF evolving on an external lattice in momentum space has been realized experimentally as described in Ref. [19]. Additional experimental implementations of quantum walk systems can be found in Refs. [36–53].

The coin operator manipulates the internal quantum states at each position, while the step operator shifts these states to new positions in the external DOF. A balanced coin maintains an equal probability distribution across the internal states after mixing. In a two-state system with internal states $|1\rangle \equiv \binom{0}{1}$ and $|2\rangle \equiv \binom{1}{0}$, common balanced coins include the Hadamard coin $\hat{H}$ and the beamsplitter matrix $\hat{Y}$:

$$\hat{H} = \frac{1}{\sqrt{2}} \begin{pmatrix} 1 & 1 \\ 1 & -1 \end{pmatrix}, \quad \hat{Y} = \frac{1}{\sqrt{2}} \begin{pmatrix} 1 & i \\ i & 1 \end{pmatrix} \tag{6}$$

Labeling the external states by $|n\rangle$, the step operator in one dimension, linking external states separated by d positions on the lattice, is expressed as:

$$\hat{S} = |2\rangle\langle 2| \otimes \sum_n |n+d\rangle\langle n| + |1\rangle\langle 1| \otimes \sum_n |n-d\rangle\langle n| \tag{7}$$

$$= \exp\left(-i\hat{n}d \cdot \sigma_z\right). \tag{8}$$

Here, σ_z represents the Pauli-z matrix. Typically, the step operator connects neighboring positions in the external DOF. Systems with additional internal DOFs can be described analogously.
To initialize a discrete-time quantum walk, a different coin operator might be used as a gate. Considering the equations above, we could write down an example for a QW protocol: $\hat{U}step = [\hat{H}\hat{S}]^t\hat{Y}$, where t is the number of time steps. Here $\hat{Y}$ is the gate and $\hat{W}$ is the coin implementing the walk. The final probability distribution is given by $P(n,t) = P_{|1\rangle}(n,t) + P_{|2\rangle}(n,t)$. Note that the coin used as a gate causes the maximal separation between the internal stats of $\exp(i\pi/2)$ in the relative phase. This is necessary so that both the internal states experience different dynamics during the walk which causes the overall walk to evolve symmetric. Symmetries of quantum walks will be of great relevance along this work.
Quantum walks exhibit ballistic expansion in the external DOF, corresponding to a quadratic speedup compared to the diffusive expansion of classical random walks. The inherent determinism of quantum mechanics introduces randomness only during the measurement process. This quadratic speedup in expansion could lead to exponential speedup in quantum computing algorithms, as discussed in Refs. [10, 54].

2.1.2 Quantum kicked rotor

The quantum kicked rotor (QKR) serves as the quantum mechanical analog to the classical kicked rotor. In the classical scenario, a particle is confined to a circular path, and a homogeneous field periodically applies a very brief impulse, or "kick," to the particle. The strength of this kick depends on the particle's position along the ring. The system is described by the Hamiltonian:

$$\mathcal{H} = \frac{1}{2}p^2 + k\cos(\theta)\sum_{n=-\infty}^{\infty}\delta(t-n\tau) \tag{9}$$

In this expression, p is the particle's momentum, k represents the kick strength, θ is the angular position related to the kicking field's direction, and τ is the interval between kicks.
The problem is typically translated on a line by transforming the periodic properties of the ring into a periodic kick potential. In this framework, the kick potential itself is periodic, making the kick strength dependent on the position θ. Experimentally, this corresponds to a periodic pulse by a standing wave laser [19, 20, 55]. For a particle moving along a line, it experiences identical kick strengths whenever it passes a full period of the potential, such that $\theta = 2\pi$. Thus, the angular position can be expressed as $\theta = x \mod (2\pi)$, where x is the position on the line. In other words, the system's interpretation changes either on a ring geometry or on a line with periodic kicking, but it is described by the same Hamiltonian framework. We typically consider the system to be constrained to a one-dimensional line with a periodic laser applied to it.

To formulate the quantum mechanical analog, we use the correspondence principle. The Hamiltonian for the quantum kicked rotor is:

$$\hat{\mathcal{H}} = \frac{1}{2}\hat{p}^2 + k\cos(\hat{\theta})\sum_{n=-\infty}^{\infty}\delta(t-n\tau) \tag{10}$$

In this quantum version, the angular position operator corresponds to $\hat{\theta} = \hat{x} \bmod 2\pi$ and typically corresponds to the position operator on a ring geometry. As already indicated, this geometry is effectively implemented by a 2π periodic standing wave potential in the experimental realization [19, 20, 55]. The one-period Floquet operator, which dictates the time evolution of the system, can be derived from this Hamiltonian. Due to the

time-dependent nature of the Hamiltonian, the Dyson series [56] is applied:

$$\begin{aligned}\hat{U}(t+\tau,t) &= \hat{\mathcal{T}}\exp\left(-i\int_t^{t+\tau}\hat{\mathcal{H}}(t'),dt'\right)\\ &= \exp\left(-i\frac{\hat{p}^2}{2}\tau\right)\cdot\exp\left(-ik\cos(\hat{\theta})\right)\end{aligned} \tag{11}$$

Here, $\hat{\mathcal{T}}$ denotes the time-ordering operator. The evolution operator for one period decomposes into two components: one representing the kick and the other representing the free evolution between kicks. Depending on the values of k and τ, the model can exhibit different behaviors: dynamical localization (where energy growth halts), anti-resonance (where the system does not evolve), and resonance (where energy grows quadratically), which can be easily tested numerically. This quadratic growth in energy corresponds to ballistic expansion in momentum space, which is again the signature of quantum walks compared to their classical counterpart. In this work we are always interested in the resonant free evolution between subsequent kicks, which means that we always have $\tau = 4\pi$, as detailed in the following section.

2.1.3 Quasimomentum - The free evolution operator

Owing to the 2π periodicity of the potential, the Bloch theorem states that a basis of wave functions exists that solve the Schrödinger equation [21]. These solutions are expressed as:

$$\psi(x,t) = e^{-i\beta x}\psi_\beta(x,t) \tag{12}$$

In this formulation, the function $\psi_\beta(x,t)$ is periodic in x, mirroring the periodicity of the potential. The theorem indicates that within our dimensionless framework, momentum can be decomposed into an integer part n and a fractional part $\beta \in [0,1)$, with β being conserved. This fractional part is referred to as the quasimomentum:

$$p = n + \beta \tag{13}$$

This establishes a lattice structure within momentum space, which is particularly evident when $\beta = 0$. The free evolution operator can be reformulated as follows:

$$\exp\left(-i\frac{\hat{p}^2}{2}\tau\right) = \exp\left(-i\frac{(\hat{n}+\beta)^2}{2}\tau\right). \tag{14}$$

For zero quasimomentum ($\beta = 0$), the free evolution operator becomes the identity if $\tau = 4\pi$. A free evolution with $\tau = 4\pi$ corresponds to a full Talbot period. In this resonant configuration, the system's evolution is governed solely by the kick operator. The introduction of quasimomentum accounts for the system's finite temperature and introduces a deviation from the resonance condition. Typically, the system's overall behavior remains largely unaffected if these deviations are sufficiently small. [1, 4, 8, 9, 21] Experimentally the BEC is distributed by a few percent around zero momentum [19, 20, 57]. However, deviations from the resonance condition naturally lead to decoherence, causing the system's quantum resonances to decay over time. Besides quasimomentum, various additional perturbations typically occur in the framework of the QKR. Typical sources of decoherence are phase noise [4, 8], finite pulse width [1, 58] or spontaneous emissions [1, 3, 21]. For a more comprehensive introduction to the quantum kicked rotor, see Refs. [2, 59].

2.1.4 Atom Optics Kicked Rotor Walks

The atom optics kicked rotor (AOKR) walk builds upon the kicked rotor model discussed in Sec. 2.1.2. To model an actual quantum walk, the system is extended to include a two-state internal degree of freedom (DOF), as outlined in Sec. 2.1.1. The Hamiltonian describing this extended system is:

$$\hat{\mathcal{H}} = \frac{1}{2}\hat{p}^2 \otimes \mathbf{1} + k\cos(\hat{\theta})\sum_{n=-\infty}^{\infty}\delta(t-n\tau)\otimes\sigma_z \tag{15}$$

In the context of the discrete-time quantum walk, the Floquet operator, which acts on the external DOF, is interpreted as the step operator. As indicated in Sec. 2.1.3, choosing $\tau = 4\pi$ and assuming $\beta = 0$ yields the resonant step operator:

$$\begin{aligned}\hat{\mathcal{U}}_{step} = \hat{\mathcal{U}}_f \hat{\mathcal{U}}_k &= \exp\left(-i\tau\frac{\hat{p}}{2}\otimes\mathbf{1}\right)\exp\left(-ik\cos(\hat{\theta})\otimes\sigma_z\right) \\ &\overset{\tau=4\pi}{=} \begin{pmatrix} \exp\left(-ik\cos(\hat{\theta})\right) & 0 \\ 0 & \exp\left(ik\cos(\hat{\theta})\right) \end{pmatrix}\end{aligned} \tag{16}$$

This formulation clarifies that the internal states experience kicks in opposite directions. Unlike the step operator for the ideal quantum walk described in Eq. (8), this operator does not exclusively couple neighboring momentum states. Instead, depending on the kick strength k, it can couple multiple momentum states simultaneously.
As reported in Ref. [21], there exists a range of k values between 0.75 and 2.75 where the operator achieves effective overlap between neighboring momentum states. For smaller values of k, the walk becomes "lazy," meaning the system exhibits minimal evolution due to the strongest coupling occurring with the onsite state. Conversely, for larger values of k, the operator involves momentum states that are too far apart, reducing similarities to the quantum walk described in Sec. 2.1.1. It is crucial to note that even within the optimal k range, the coupling is not limited to the neighboring momentum state; however, the neighboring state remains the primary coupling partner [9].
By maintaining the resonance condition, one ensures the system dynamically evolves in a manner consistent with quantum walks, thereby preserving the signature features such as ballistic expansion. [2, 3, 9, 60–62]

The system involves two internal spin states: one state is kicked to the left and the other to the right in momentum space [4, 19, 20, 57], as represented by the Pauli matrix σ_z in Eq. (16). A coin matrix then performs rotation, mixing these two states at each step of the QW [19, 20, 57].
Without external influences, both spin states would evolve identically under the influence of the evolution operator. This symmetry can be disrupted by introducing a ratchet effect through specific initial conditions in the walker's space. The initial ratchet state is established by linking at least two adjacent momentum states with a relative phase of $e^{i\pi/2}$:

$$|\psi_{\mathrm{R}}\rangle = \frac{1}{\sqrt{J}}\sum_j e^{i\cdot j\pi/2}\,|n=j\rangle\otimes|l\rangle\,, \tag{17}$$

where $|l\rangle$ signifies the ratchet state preparation, either in the internal state $|l=1\rangle$ or $|l=2\rangle$. For our purposes, the system is initialized in $|l=2\rangle$. This relative phase shift is experimentally induced via precisely timed Bragg pulses [19, 20, 63] and causes the internal states of the atom to develop mirror symmetric in opposing directions in the walkers space. The sign of the kick potential, which alternates between the two spin states, determines the mean momentum transfer. Importantly, as the number of momentum classes involved in the initial state J in Eq. (17) increases, the dispersion due to directed kicking diminishes [9]. In Ref. [9, 64], the gradient of the kick potential is identified as the primary driving force of the system. The most significant gradient, and consequently the strongest net force, occurs at the edges of the kick potential. The phase shift of $e^{i\pi/2}$ in the quantum ratchet, as described in Eq. (17), is designed to align the peak of the wave function with the position of the maximum gradient. For larger values of J the initial wave function is located more densely at these edges, thus resulting in a more uniform effective kick strength across the BEC. For $J \geq 3$, the evolution closely approximates an ideal QW [9, 63]. Unless otherwise specified, we will always assume an initial state with $J = 3$, initialized in $|2\rangle$:

$$|\psi_{\mathrm{R}}\rangle = \frac{1}{\sqrt{3}}\left(-i\,|n=-1\rangle + |n=0\rangle + i\,|n=1\rangle\right)\otimes|2\rangle\,. \tag{18}$$

The final momentum distribution significantly depends on the choice of the coin operator. This coin operation is implemented through Rabi coupling between the atom's two spin states, using resonant microwave pulses to perform a unitary rotation [19, 57, 65]. The most general form of a balanced coin matrix for a two-state system with a pseudo-spin degree of freedom is expressed using three Bloch angles: χ, γ, and α. This matrix is given by:

$$\hat{M}(\chi=\frac{\pi}{4},\gamma,\alpha)=\begin{pmatrix} e^{i\alpha}\cos(\chi=\frac{\pi}{4}) & e^{-i\gamma}\sin(\chi=\frac{\pi}{4}) \\ -e^{i\gamma}\sin(\chi=\frac{\pi}{4}) & e^{-i\alpha}\cos(\chi=\frac{\pi}{4}) \end{pmatrix} = \frac{1}{\sqrt{2}}\begin{pmatrix} e^{i\alpha} & e^{-i\gamma} \\ -e^{i\gamma} & e^{-i\alpha} \end{pmatrix}. \tag{19}$$

Here, $\chi = \frac{\pi}{4}$ ensures that the coin is balanced, meaning both internal states are weighted equally, even though with different phases. As we are only concerned about balanced QWs, we effectively have two free Bloch angles, γ and α, in the coin matrix. The QWs outlined in Refs. [19, 20, 55] consist of a series of unitary operations:

$$\hat{\mathcal{U}}^t_{\text{step}} = [\hat{\mathcal{U}}\hat{Q}_2]^t\hat{\mathcal{U}}\hat{Q}_1. \tag{20}$$

Here, $t \in \mathbb{N}$ represents the number of steps applied to the initial state. The main features of the final momentum distribution, such as symmetry and shape within the walker space, are heavily influenced by the choice of the initial coin $\hat{Q}_1$ and the coin used during the walk $\hat{Q}_2$. These coins are then specified by Eq. 19 by the choice of some α and γ. We will observe asymmetries arising from most combinations of the coin matrix parameters α and γ. Also, we will observe evolving asymmetries as a consequence of spontaneous emissions (SE) [1]. These occur for kicks with finite pulse duration, which is experimentally always the case. Typically SE is viewed as a nuisance, which makes this a particularly interesting phenomenon, as it opens a route for designing a noise-induced quantum ratchet.

2.1.5 Finite Pulse Width of the kicking Laser

In practice, the kicks imparted by the laser have a finite pulse duration, denoted as τ_p. To simulate this effect, the kick is numerically divided into h sub-kicks [3]. Each sub-kick is characterized by $\frac{1}{h}$ of the total kicking strength and is followed by a free evolution over $\frac{1}{h}$ of the total pulse duration. The choice of the parameter h is a balance between computational feasibility and accuracy. For our parameter regime, $h = 10$ is sufficient to achieve convergence. The evolution operator for the kick can thus be expressed as:

$$\hat{\mathcal{U}}_{\text{kick}} = \prod_h \exp\left(-i\frac{\hat{p}^2}{2}\frac{\tau_p}{h}\right)\exp\left(-i\frac{k}{h}\cos(\hat{\theta})\sigma_z\right). \tag{21}$$

In this study, our primary focus is on the effects of spontaneous emission (SE) that occur while the kick potential is activated [3, 19, 60, 61], rather than the consequences of the finite pulse width. It is known that a finite pulse width can introduce reflective boundaries in momentum space [60]. This is demonstrated in Fig. 1. In Fig. 1 (a) we see an AOKR-walk, implemented with δ-shaped pulses, in Fig. 1 (b) we see the

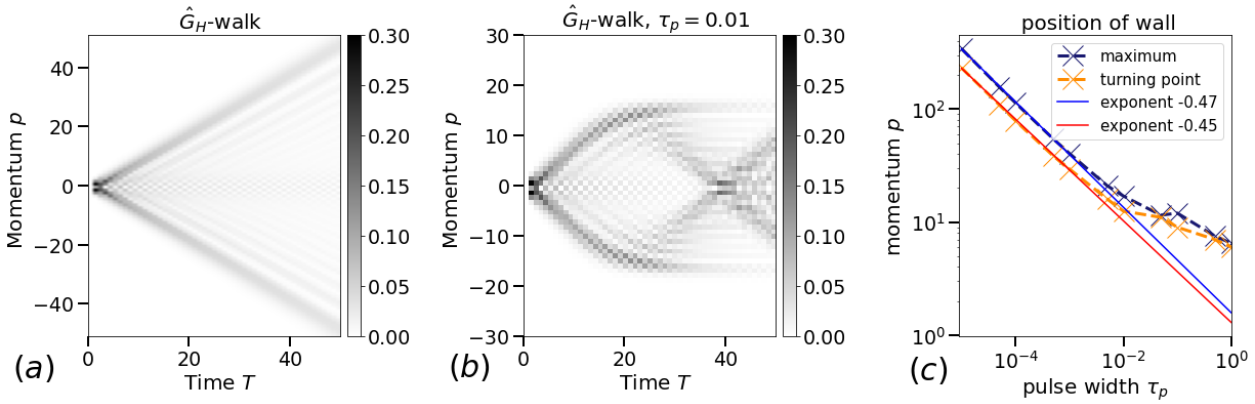

Figure 1: (a) shows the $\hat{G}_H$ walk in the ideal case. In (b) we consider a finite pulse width of $\tau_p = 0.01$ and in (c) we quantify the position of the induced reflective walls in momentum space by the method described in the text.

same walk with a finite pulse width of $\tau_p = 0.01$. We see that the finite pulse width effectively introduces

a reflective barrier in momentum space. The position of this barrier in dependency of τ_p is quantified in Fig. 1 (c). Numerically this is done by calculating the kinetic energy in the system $\langle \frac{\hat{p}^2}{2} \rangle$ and finding the first turning point and the first maximum of the energy. The ballistic expansion in momentum space seen in Fig. 1 (a) implies quadratic energy growth. A δ-kicked walk thus does not exhibit features such as a turning point or a maximum in the temporal development of the energy. These are thus induced by the "walls" in momentum space. Thus the turning point marks the time step where the gas starts to "see" these walls and the maximum marks the point where the gas "hits" the walls and is reflected, causing a loss in energy. For these two interesting time points, one may then take the momentum distribution and sum up the probabilities $|\psi_n^2|$ for increasing momentum classes n, until one hits a reasonably chosen threshold, for example 95%. This systematically quantifies the position of the wall in momentum space. These two positions in momentum space, associated with the turning point and the maximum of the energy curve, are shown in Fig. 1 (c). For a QKR without internal spin DOF one would expect a $\frac{1}{\tau_p}$ dependency [58]. We see that we observe a somewhat different dependency for our system with an additional internal DOF.

To mitigate the pertubations from these walls, we further ensure that τ_p is sufficiently short, minimizing any perturbations to the momentum-space distributions caused by the finite duration of the pulse. This way, we ensure that the finite pulse width does not significantly impact the dynamics of the system. This allows us to focus on the influences of SE, however still in an experimentally relevant framework. Numerically we will typically choose $\tau_p = 0.005$ in our simulations.

2.1.6 Spontaneous Emissions

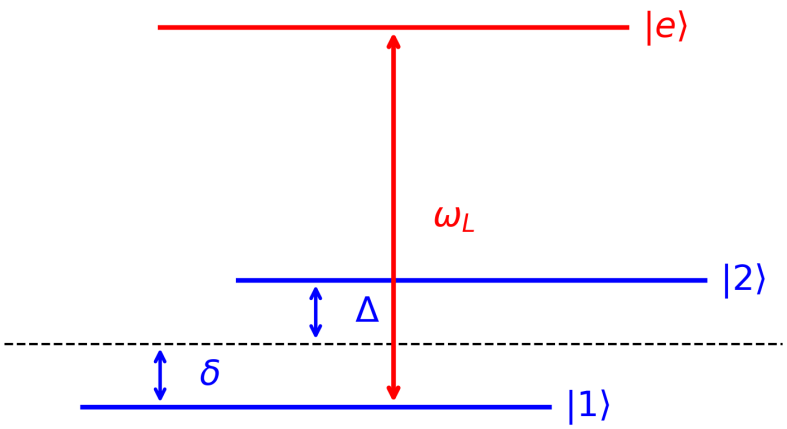

Figure 2: Shown is the level scheme for our system, showing two internal states $|1\rangle$ and $|2\rangle$. The excited state $|e\rangle$ is employed to impart kicks to the atoms using an off-resonant standing laser wave. ω_L signifies the frequency of the kicking laser, while δ and Δ represent the detunings for the two potential transitions relative to the laser frequency. The colors signify which transitions are relevant for the numerical implementation; Red implies that it is physically meaningful, however numerically only the two internal states marked in blue are relevant, as we model SE by a projection on either $|1\rangle$ or $|2\rangle$ and a shift in quasimomentum.

In the dynamics of the AOKR system, a SE event occurs when an atom is excited by a laser pulse of finite width in time and then randomly decays to the lower energy states $|1\rangle$ or $|2\rangle$. It is assumed that

these excitations are far from internal electronic resonance, in contrast to [66, 67]. During this spontaneous de-excitation, a photon is emitted, resulting in a shift of the atomic quasimomentum [3, 61].
For the AOKR, we effectively solve a quantum-optical master equation [21], introduced in Sec. 1.2, which in Lindblad form is expressed as:

$$\frac{d\hat{\rho}}{dt} = -i[\hat{\mathcal{H}}, \hat{\rho}] + \hat{\mathcal{D}}(\hat{\rho}), \tag{22}$$

where $\hat{\rho}$ is the density operator. This master equation includes a Hamiltonian part and a dissipation term, described by the operator $\hat{\mathcal{D}}(\hat{\rho})$. For non-resonant driving, we derive the effective Hamiltonian [21, 68], detailed in Chapter 5 of [21]:

$$\hat{\mathcal{H}} = \frac{1}{1+\frac{\mu^2}{4\delta^2}} \frac{\Omega_1^2}{8\delta} \left(\cos(2k_L\hat{x}) + 1\right) |1\rangle\langle 1| - \frac{1}{1+\frac{\mu^2}{4\Delta^2}} \frac{\Omega_2^2}{8\Delta} \left(\cos(2k_L\hat{x}) + 1\right) |2\rangle\langle 2|. \tag{23}$$

Let μ represent the rate of spontaneous emission (SE) events, defined as:

$$\mu = \mu_1 + \mu_2 = \frac{k_1}{\tau_p \tau_{\mathrm{SE}} |\delta|} + \frac{k_2}{\tau_p \tau_{\mathrm{SE}} |\Delta|} \tag{24}$$

Here, δ and Δ are the detunings from resonance, as illustrated in Fig. 2. Since these detunings are much smaller compared to the laser frequency, we use the approximation $k_1 = k_2 = k$ [19, 69]. This leads to the relations $\delta = -\Delta$ and $\mu_1 = \mu_2$ for the SE rates in Eq. (24). Again, τ_p denotes the pulse duration, and τ_{SE} signifies the lifetime of the transition.
The dissipation operator $\hat{\mathcal{D}}$ captures the decay from the excited state to either ground state $|1\rangle$ or $|2\rangle$ at their respective SE rates. This process is mathematically described by the Lindblad operators $\hat{\mathcal{P}}_{|1\rangle}$ and $\hat{\mathcal{P}}_{|2\rangle}$, which are projection operators onto the corresponding lower energy states.
To solve the master equation Eq. (22), we employ the quantum trajectory method as detailed in [3, 14]. This approach modifies the walk protocol to incorporate both the Hamiltonian and dissipative parts of Eq. (22), treating dissipation as a statistical event with a probability p_{SE}. By averaging over a large number of trajectories, we can obtain a comprehensive picture of the system's dynamics.
To implement this method numerically, we interpret a spontaneous emission (SE) event as a projection onto one of the internal states using projection operators $\hat{\mathcal{P}}_{|1\rangle}$ and $\hat{\mathcal{P}}_{|2\rangle}$, combined with a shift in quasimomentum, β_{SE}. This accounts for the de-excitation of the atom to either of the energetically lower states and the recoil of the emitted photon and accounts for the dissipative evolution in the walk protocol. These projection operators are defined as follows:

$$\hat{\mathcal{P}}_{|1\rangle} = \frac{1}{\mathcal{N}} \left(A|\psi_{|1\rangle}\rangle \otimes |1\rangle\langle 1| + B|\psi_{|2\rangle}\rangle \otimes |1\rangle\langle 2|\right), \tag{25}$$

$$\hat{\mathcal{P}}_{|2\rangle} = \frac{1}{\mathcal{N}} \left(C|\psi_{|1\rangle}\rangle \otimes |2\rangle\langle 1| + D|\psi_{|2\rangle}\rangle \otimes |2\rangle\langle 2|\right), \tag{26}$$

where $\mathcal{N}$ is a normalization constant, and A, B, C, D are detuning-dependent coefficients that can be approximated as $1/2$ according to [68].
Introducing SE into the simulation makes the system an open quantum system and complicates the evaluation of kicks [3, 61]. For each of the h sub-kicks described in Eq. (21), we calculate the occurrence of an SE event based on the probability $p_{\mathrm{event}} = \frac{\mathrm{p_{SE}}}{h}$. If an event occurs, we randomly choose between the projections $\hat{\mathcal{P}}_{|1\rangle}$ and $\hat{\mathcal{P}}_{|2\rangle}$ with equal likelihood. The quasimomentum shift β_{SE} is then drawn from a uniform distribution $\beta_{\mathrm{SE}} \in \mathrm{uniform}(-0.5, 0.5)$. When an SE event occurs, the modified partial kick operator is written as the following:

$$\hat{\mathcal{U}}_{\mathrm{SE}} = \hat{\mathcal{P}}_{|i\rangle} e^{-i\frac{(\hat{p}+\beta_{\mathrm{SE}})^2}{2}\frac{\tau_p}{h}} e^{-i\frac{k}{h}\cos(\hat{\theta})\sigma_z}, \tag{27}$$

where $|i\rangle$ represents either $|1\rangle$ or $|2\rangle$, selected with a $50-50$ probability. This approach captures both the finite duration of the kick and the potential for multiple SE events within a single pulse. The overall kick

can be expressed as a sequence of partial kicks, where the probability p_{SE} determines if an SE event occurs for each partial kick:

$$\hat{\mathcal{U}}_{\mathrm{SE-kick}} = \prod_h \hat{\mathcal{U}}_{\mathrm{SE}}. \tag{28}$$

During the intervals between kicks, the shift in quasimomentum also affects the free evolution over a full Talbot period, described by:

$$\hat{\mathcal{U}}_{\mathrm{SE-free}} = e^{-i\frac{(\hat{p}+\beta_{\mathrm{SE}})^2}{2}\tau_T} \tag{29}$$

Since the shift in quasimomentum is sampled from a uniform distribution and the Talbot period $\tau_T = 4\pi$ is considerably longer than the pulse duration τ_p, its impact is more pronounced during the free evolution than during the kick itself [1, 3, 61]. This long free evolution with off-resonant quasimomentum shifts due to SE causes major decoherence, effectively disrupting the quantum walk [1, 21, 55].
These shifts in quasimomentum during the lengthy free evolution periods between subsequent pulses are thus narrowing the quantum regime, dominated by resonant movement over diffusive processes. This primarily limits the range of SE event rates where SE-induced effects can be observed, which will be discussed in more detail in the following sections.
Given that the long-term behavior is not relevant due to dissipation prevalent in any experiment, our analysis of various effects will focus on the experimentally relevant timescales.

2.1.7 Spontaneous Emissions for different BECs

Inspired by previous experiments [70–73], various Bose-Einstein Condensates (BECs) have been investigated. Below there is a summary of the relevant transitions and corresponding numbers for Rubidium, Lithium and Sodium. This enlisting is supposed to give the reader a feeling for the experimental realities. Key parameters are the lifetime of the transition (τ_{SE}), the pulse duration (τ_p) of the laser, the Talbot period and the detuning between the internal energy levels. These parameters highlight the critical values needed for analyzing the expected spontaneous emission rates within these BECs.
The translation of the experimental values to our dimensionless units is made from the Talbot condition. In our units, $\tau = 4\pi$ corresponds to a full Talbot revival time.

The Talbot period itself is estimated in [74], also working with Sodium, from the condition $e^{-i\frac{p^2/2m}{\hbar}\tau_T} = 1$. Thus, the Talbot time is calculated by

$$\tau_T = \frac{\pi m}{\hbar k_L^2} = \frac{m\lambda_L^2}{4\pi\hbar}. \tag{30}$$

BEC	Transition	τ_{SE} (ns)	τ_p (ns)	τ_T (μs)	Δ (GHz)	m (kg)	λ_L (nm)	References
Rubidium	$5^2\mathrm{S}_{1/2} \rightarrow 5^2\mathrm{P}_{3/2}$	26.2	384	103	21.36	1.44×10^{-25}	780	[72, 73]
Sodium	$3^2\mathrm{S}_{1/2} \rightarrow 3^2\mathrm{P}_{3/2}$	16.2	5 100	10	5.34	0.32×10^{-25}	589	[72, 75]
Lithium	$2^2\mathrm{S}_{1/2}$ $F=2$ $\rightarrow$ $2^2\mathrm{P}_{1/2}$ $F=3$	27	50	3.95	1.8	0.12×10^{-25}	671	[30, 76]

The pulse duration (τ_p) is translated to dimensionless units using the relation $\tau_p = \frac{4\pi \times t_p}{\tau_T}$: The kick strength is given by $k \approx \frac{\Omega}{\Delta}\tau_p$. We are able to estimate an event probability p_{SE} which could be expected in the laboratory.

$$\mathrm{p_{SE}} = \frac{k}{\tau_{SE}\Delta}. \tag{31}$$

Throughout our simulations we will use $k = 1.45$, also used in [**?**, 4, 19, 20], which lies also in the regime of kick strength suitable for next neighbour coupling [21]. Notably, the calculations respect the experimental

setups, such as the 53° alignment of lasers in the Rubidium experiments [73], and consider the feasibility of achieving short pulse durations as demonstrated in [75, 77]. Again, we summarize our dimensionless values for τ_p and p_{SE} in a tabula.

BEC	Transition	τ_p	p_{SE}
Rubidium	$5^2\mathrm{S}_{1/2} \rightarrow 5^2\mathrm{P}_{3/2}$	0.047	0.26
Sodium	$3^2\mathrm{S}_{1/2} \rightarrow 3^2\mathrm{P}_{3/2}$	0.006 (5ns [75]) 0.126 (100ns [77])	0.017
Lithium	$2^2\mathrm{S}_{1/2}F = 2$ $\rightarrow$ $2^2\mathrm{P}_{1/2}F = 3$	0.016	0.03

2.2 Global Behavior of Symmetry

The following results have already been published in our recent paper [1]. The content of this article was created within this thesis. The following sections Sec. 2.2 and Sec. 2.3 cover these results with some additional details, closely along the line of [1].

In our recent work [4, 9], we explored the inconsistencies observed between experimental results of quantum walks (QWs) in momentum space [19, 20, 55] and theoretical predictions. These inconsistencies were primarily due to light shift effects on energy levels, which effectively interchanged the coin used during the walks. When this effective coin matrix was applied to a narrowly confined initial state in momentum space (restricted to two momentum classes, $J = 2$), it led to unexpected outcomes. Notably, a large fraction of the probability distribution was found to remain near the origin ($n = 0$), a behavior that is not observed for initial states with $J \geq 3$ [9]. However, the experimentally intended walk protocol did not show this behavior, even for $J = 2$. This observation suggests that the phase configuration within a balanced coin matrix can significantly influence the key characteristics of the final momentum distribution in a QW protocol. In this section, we delve into how different choices of coin parameters affect the symmetry properties of the walk, aiming to understand the underlying mechanisms and to shape intuition for the system.

In the subsequent analysis, all quantum walks will be initialized using the $\hat{Y}$-coin described in Ref. [9] and mentioned above in Sec. 2.1.1. This coin is defined in Eq. (20) by:

$$\hat{Q}_1 = \hat{Y} = \hat{M}\left(\frac{\pi}{4}, \frac{\pi}{2}, 0\right) = \frac{1}{\sqrt{2}}\begin{pmatrix} 1 & i \\ i & 1 \end{pmatrix}. \tag{32}$$

For the coin operator $\hat{Q}_2$ used in the walk protocol, we will employ either the $\hat{W}$-coin or the $\hat{G}_H$-coin [9]:

$$\hat{W} = \hat{M}\left(\frac{\pi}{4}, 0, 0\right) = \frac{1}{\sqrt{2}}\begin{pmatrix} 1 & 1 \\ -1 & 1 \end{pmatrix}, \tag{33}$$

$$\hat{G}_H = \frac{1}{\sqrt{2}}\begin{pmatrix} 1 & 1 \\ 1 & -1 \end{pmatrix} \equiv \frac{i}{\sqrt{2}}\begin{pmatrix} 1 & 1 \\ 1 & -1 \end{pmatrix} = \hat{M}\left(\frac{\pi}{4}, \frac{3\pi}{2}, \frac{\pi}{2}\right). \tag{34}$$

In Eq. (34), the equivalence is written because both forms of the $\hat{G}_H$-coin lead to identical walks, as a global phase does not affect the outcome. As detailed in Ref. [9], the dynamics of a walk governed by the $\hat{G}_H$-coin, in the absence of external perturbations, exhibit significantly different characteristics compared to those under the $\hat{W}$-coin. Specifically, there is a distinct peak around zero momentum. These are especially present for initial states with $J = 2$ [19], in contrast to Fig. 3, where an initial state with $J = 3$ is implemented. These two walk protocols will become important throughout this work.

In the following discussion, we will introduce a metric to characterize the various symmetry regimes within the parameter space defined by the Bloch angles α and γ.

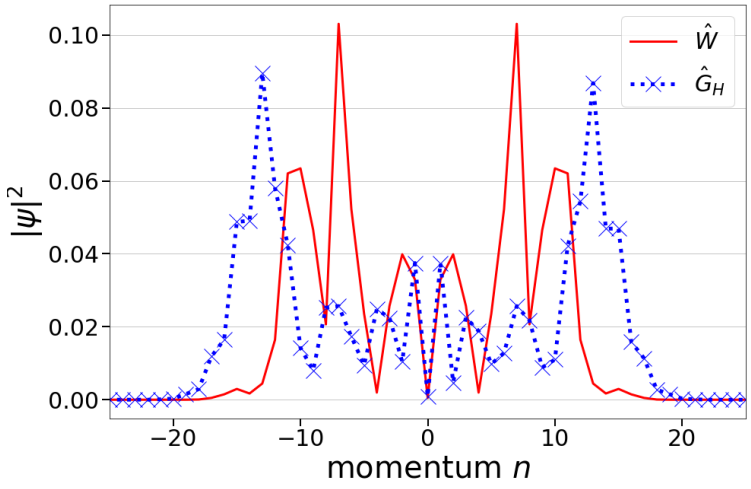

Figure 3: Depicted are two walk protocols. Both walks are initialized by the $\hat{Y}$-coin. The red curve corresponds to the momentum distribution of the walk associated with the $\hat{W}$-coin and the blue curve with the $\hat{G}_H$-coin, respectively. The distributions are shown after $T = 15$ steps of the walk. The content of this figure has been presented in Ref. [1].

2.2.1 Map of Parameter Space

To analyze the evolving asymmetries in the walk, we introduce an asymmetry observable, S. This measure, inspired by the method in [16], quantifies asymmetry by comparing the probability distribution on either side of the inversion point at momentum $n = 0$. Specifically, S is calculated by subtracting the total probability on the left from the total probability on the right:

$$S = \sum_{n>0} |\psi_n|^2 - \sum_{n<0} |\psi_n|^2. \tag{35}$$

Here, $|\psi_n|^2$ represents the probability associated with the momentum class n.
In the context of Parrondo's paradox, where two losing strategies can combine to form a winning one, the sign of S indicates whether the strategy is winning or losing. [16] In our study, we use S to measure symmetry.
In the sections that follow, we will delve into the behavior of the observable $S(\gamma, \alpha)$, providing arguments and qualitative insights to develop an intuitive understanding of how symmetry is affected by the parameters γ and α.

2.2.2 Symmetric Configurations

For certain relationships between the parameters γ and α, additional symmetries can be found within the coin matrix itself. Empirically, these additional symmetries tend to result in more symmetrical behavior in the quantum walk. We will discuss two specific cases.
In the first case, consider $\gamma = \alpha$ or $\gamma = \alpha \pm 2\pi$:

$$\hat{M}\left(\chi = \frac{\pi}{4}, \gamma, \alpha = \gamma\right) = \frac{1}{\sqrt{2}} \begin{pmatrix} e^{i\alpha} & e^{-i\alpha} \\ -e^{i\alpha} & e^{-i\alpha} \end{pmatrix} \equiv \frac{1}{\sqrt{2}} \begin{pmatrix} \phi & \rho \\ -\phi & \rho \end{pmatrix}. \tag{36}$$

In the second case, consider $\gamma = \alpha \pm \pi$:

$$\hat{M}\left(\chi = \frac{\pi}{4}, \gamma, \alpha = \gamma \pm \pi\right) = \frac{1}{\sqrt{2}} \begin{pmatrix} e^{i\alpha} & -e^{-i\alpha} \\ e^{i\alpha} & e^{-i\alpha} \end{pmatrix} \equiv \frac{1}{\sqrt{2}} \begin{pmatrix} \phi & -\rho \\ \phi & \rho \end{pmatrix}. \tag{37}$$

In these scenarios, the coin matrix features pairs of identical phases. Generally, this condition is not given. However, when the phases align in this manner, the internal states are mixed similarly at each timestep.

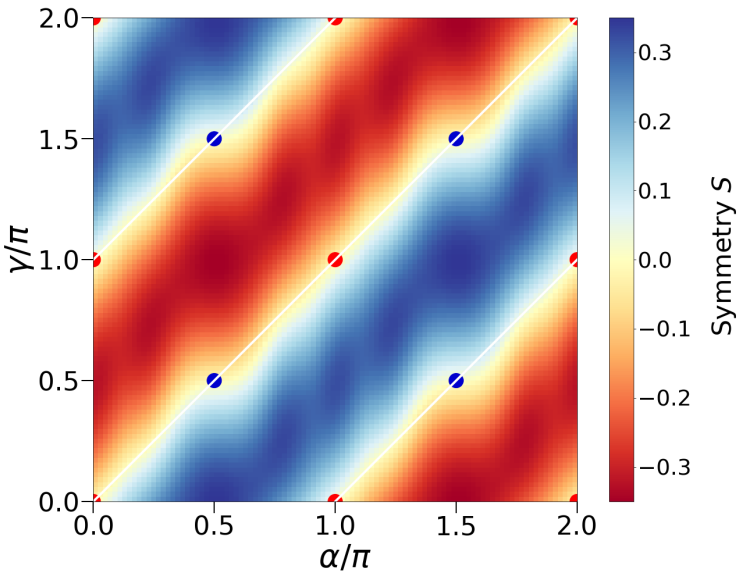

Figure 4: The colormap displays the symmetry indicator $S(\gamma, \alpha)$ as a function of the free Bloch angles α and γ, evaluated after $T = 15$ steps in the evolution. Blue dots represent the walk induced by the $\hat{G}_H$-coin, as shown in Fig. 10, while red dots represent the walk induced by the $\hat{W}$-coin. The white lines indicate the coin configurations where an additional symmetry is present, which is described in detail in Sec. 2.2.2. The content of this figure has been presented in Ref. [1].

It seems plausible that when the states are mixed with consistent phases throughout the protocol, they evolve more symmetrically, although in opposite directions due to the ratchet effect of the initial state. This consistent phase mixing likely contributes to a more balanced quantum walk.

In Fig. 4, the quantum walk evolves over $T = 15$ timesteps, and the symmetry indicator $S(\gamma, \alpha)$ is displayed as a function of the free Bloch angles. The plot reveals prominent red and blue stripes, highlighting regions where the QW leans to the left or right. The white lines between these areas, where $S = 0$, qualitatively correspond to the expected lines in parameter space. Especially at the lines $\gamma = \alpha$ and $\gamma = \alpha \pm \pi$, which reflect the additional symmetries of the coin as given by Eq. (36) and Eq. (37), respectively.

Not all quantum walks with $S = 0$ in Fig. 4 perfectly align with theoretical predictions. The deviations appear to be influenced by areas of high asymmetry, indicating more complex dynamics than initially anticipated. Nevertheless, the theory effectively predicts the qualitative behavior of balanced walks in parameter space due to the coin's phase symmetries, thereby enhancing our understanding of the system. Additionally, it has been numerically verified that the empirical lines with $S = 0$ approach the predicted lines more closely as the number of timesteps increases, which can be seen in Appendix A.

In Fig. 4, the blue and red dots denote coin types that are equivalent to $\hat{W}$ and $\hat{G}_H$ from Eqs. (33) and (34), respectively, up to a global phase. These points align perfectly with the white lines predicted by our rudimentary theory.

The parameter S indicates the direction of the walk's progression but does not provide details about the walk's overall shape. This means that while the momentum distribution can be balanced as indicated by $S = 0$, their forms may not necessarily show an inversion point, illustrating how rare true symmetry is. Only the two specific classes of walks corresponding to the $\hat{W}$ and $\hat{G}_H$ coin demonstrate a clear inversion point.

The first class, associated with the $\hat{G}_H$ walk, is shown in Fig. 10. This class repeats at parameter values where γ and α are half-integer multiples of π. It is marked by blue dots in Fig. 4. The second class, related to the $\hat{W}$-coin, occurs at integer multiples of π for the Bloch angles, depicted by red dots in Fig. 4. Walks in these classes have coins that are either entirely real or entirely complex, respectively. When initialized with the $\hat{Y}$-coin, these walks maintain the initial rotation of π between internal states.

Other configurations introduce both real and imaginary phase components, which disrupt this initial rotation, preventing a perfectly mirror-symmetric walk evolution. As a result, these other configurations are either balanced without a clear mirror axis or exhibit pronounced asymmetry.

2.2.3 Asymmetric Configurations

In Fig. 4, the broad diagonal stripes indicate regions of asymmetry, consistent with our findings in Sec. 2.2.2. To explore the deeply asymmetric regime along the stripe pattern, we express the relationship between α and γ as $\gamma = \alpha + \zeta$, where ζ is an arbitrary but fixed parameter. This yields the following expression for the coin matrix:

$$\hat{M}\left(\chi = \frac{\pi}{4}, \gamma = \alpha + \zeta, \alpha\right) = \frac{1}{\sqrt{2}} \begin{pmatrix} e^{i\alpha} & e^{-i(\alpha+\zeta)} \\ -e^{i(\alpha+\zeta)} & e^{-i\alpha} \end{pmatrix} \equiv \frac{1}{\sqrt{2}} \begin{pmatrix} \phi & \rho e^{-i\zeta} \\ -\phi e^{i\zeta} & \rho \end{pmatrix}. \tag{38}$$

From our observations in Fig. 4, we see that the walk tends to evolve asymmetrically to the left for $0 < \zeta < \pi$. In this range, the phase $e^{i\zeta}$ lies on the right half of the complex unit circle with $\mathrm{Re}(e^{i\zeta}) > 0$, while $e^{-i\zeta}$ lies on the left half with $\mathrm{Re}(e^{-i\zeta}) < 0$. Conversely, for $-\pi < \zeta < 0$, the walk evolves asymmetrically to the right, with $e^{i\zeta}$ on the left half of the complex unit circle and $e^{-i\zeta}$ on the right half.
Therefore, rotating the phase angles associated with ζ by 180° changes the direction of asymmetry in the walk. When the ζ-related phase is zero, we recover the symmetric case described from Sec. 2.2.2.
In the parameter scan depicted in Fig. 4, we identify specific points in the asymmetric regions that exhibit extreme asymmetry. These points in the $\mathcal{C} = (\alpha, \gamma)$ coordinate frame are:

$$\mathcal{C}_1^+ = \left(\alpha = \frac{1}{2}\pi, \gamma = 0\right) \rightarrow \zeta = -\frac{\pi}{2} \tag{39}$$

$$\mathcal{C}_2^+ = \left(\alpha = \frac{3}{2}\pi, \gamma = \pi\right) \rightarrow \zeta = -\frac{\pi}{2} \tag{40}$$

$$\mathcal{C}_1^- = \left(\alpha = \frac{1}{2}\pi, \gamma = \pi\right) \rightarrow \zeta = +\frac{\pi}{2} \tag{41}$$

$$\mathcal{C}_2^- = \left(\alpha = \frac{3}{2}\pi, \gamma = 2\pi\right) \rightarrow \zeta = +\frac{\pi}{2} \tag{42}$$

In these expressions, the superscript indicates the direction of asymmetry, with (+) for right and (-) for left. These points are notable for having fully complex elements along the diagonal and fully real elements off-diagonal. This trait, respective a global phase factor of i, resembles the initializing $\hat{Y}$-coin, used for all walks. This configuration effectively cancels the initial π rotation between the internal states imparted by the $\hat{Y}$-coin, leading to a pronounced asymmetry in the walk.
The emergence of either highly symmetric or highly asymmetric behaviors thus depends on the phase rotation of the internal states between the coin used during the walk, $\hat{Q}_2$, and the initial coin, $\hat{Q}_1$. Specifically, the behavior is influenced by whether this rotation is maximized at 90° (resulting in symmetry with an inversion point) or effectively nullified (resulting in maximum asymmetry) in the off-diagonal elements.

Although these results have potential applications in developing Parrondo-like games along the line of [16], our main objective moving forward is to investigate the impact of SE on the symmetry of the QWs.

2.3 Spontaneous Emissions in AOKR walks

Up to this point, we have concentrated on the asymmetries in coherent QW protocols without any stochastic noise. Asymmetries resulted only from the choice of the coin matrix and were thus inherent to the choice of the walk-protocol itself. However, asymmetries caused by nuisance are of significant interest due to their potential in developing a QW ratchet [78]. The QW ratchet discussed in this study is unique because it is driven by SE. While SE is typically associated with inducing decoherence [55], in this context, it plays a crucial role in forming a QW ratchet. This highlights a paradigm shift where SE, usually seen as an annoyance, is leveraged to create a beneficial effect. For clarity note the following; Our initial state is a ratchet

state. This is, because it breaks a symmetry, causing the momentum distribution of each internal state to evolve mirror symmetrically in opposite directions. Now we are adding additional nuisance, which breaks this mirror symmetry of the momentum distribution, causing the walk to lean towards a specific direction. This second symmetry breaking is the ratchet effect we will discuss in detail in the following section.

In the context of ^{87}Rb quantum walks [19, 20, 55], the Talbot time is 103μs, corresponding to 4π in our units. In typical AOKR experiments, pulse widths are around 100ns, although much shorter pulses are feasible, as demonstrated in studies such as [75, 77]. For our analysis, we consistently use $\tau_p = 0.005$, which translates to a pulse duration of a few tens of nanoseconds. This choice effectively reduces the potential perturbations caused by the finite pulse width [3, 79–81], particularly for longer walks extending beyond several tens of steps.

2.3.1 Spontaneous Emissions During Quantum Walks

Figure 5 illustrates how increasing SE rates influence the behavior of quantum walks. Under the $\hat{W}$ coin, the walk gradually transitions to a more classical form, displaying mild asymmetry. This is quantified by the asymmetry measure S, shown in the top right corner of each subplot, where the momentum distributions are computed using the quantum trajectory method from Sec. 2.1.6.
In contrast, the walk governed by the $\hat{G}_H$ coin exhibits a significantly more pronounced asymmetry, often an order of magnitude greater than that observed in the $\hat{W}$ walk. As SE event probabilities rise, the ballistic peaks corresponding to positive momentum classes are notably suppressed, while those for negative momentum classes are less affected.
With higher SE rates, resonant peaks diminish, and the momentum distribution increasingly resembles a Gaussian shape, signaling a quantum-to-classical transition. This transition, which leads to a reduction in asymmetry, will be further explored in detail in Section 2.4.2.

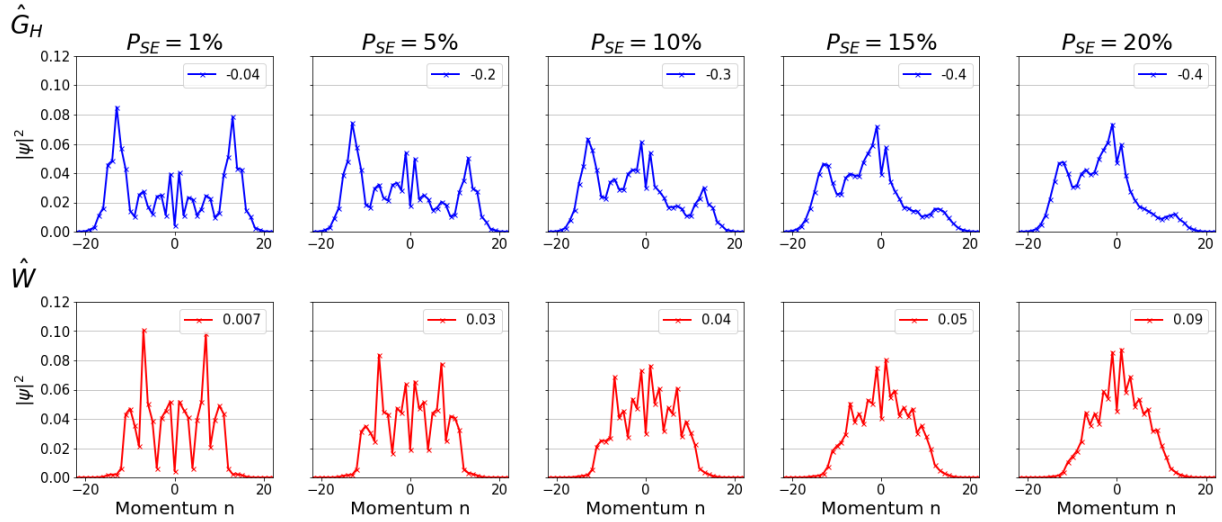

Figure 5: Comparison of two distinct walk protocols after $T = 15$ steps of evolution, with increasing SE. Both protocols start with the $\hat{Y}$-coin. The top row shows evolution under the $\hat{G}_H$-coin, while the bottom row shows evolution under the $\hat{W}$-coin. SE rates increase from left to right. The number in the upper right corner of each plot denotes the symmetry indicator S. The $\hat{G}_H$-coin walk develops significant asymmetry, whereas the $\hat{W}$-coin walk exhibits only slight asymmetry. This slight asymmetry in the $\hat{W}$-protocol could be assumed to be caused by numerical fluctuations but appears relatively stable. Each distribution is an average over 10000 realizations, with the specified SE probabilities p_{SE} per kick. The content of this figure has been partially presented in Ref. [1].

As the SE rates increase, the distinct diagonal patterns within the free Bloch angles parameter space become increasingly blurred, as shown in Fig. 6. Within this parameter space, the $\hat{W}$-walk (indicated by the

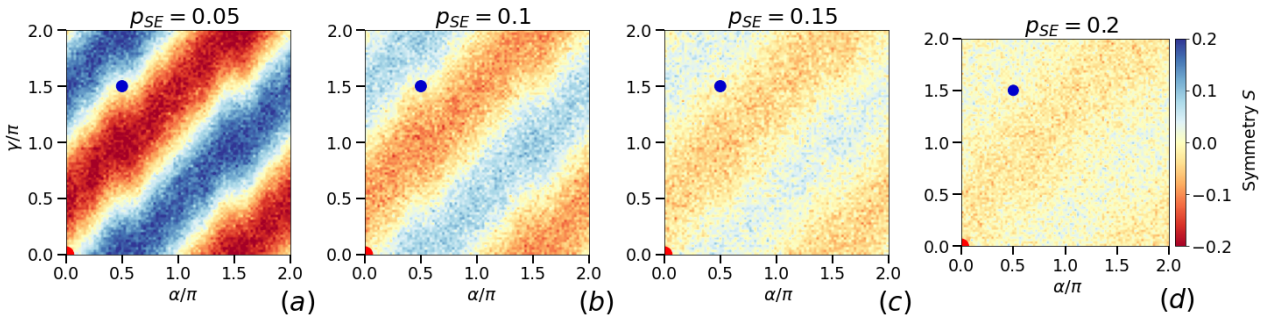

Figure 6: The figure presents a scan of the symmetry indicator $S(\gamma, \alpha)$ for the QW, evaluated after 15 steps. The walk is initiated with the $\hat{Y}$-coin and then evolves under $\hat{M}(\chi = \frac{\pi}{4}, \gamma, \alpha)$. The SE rates increase from left to right. The red dot at $(\gamma = 0, \alpha = 0)$ indicates the more symmetric walk using the $\hat{W}$-coin, while the blue dot at $(\gamma = 1.5\pi, \alpha = 0.5\pi)$ indicates the asymmetric walk using the $\hat{G}_H$-coin (refer to Fig. 4). The $\hat{G}_H$-walk appears to occupy a less stable region in parameter space concerning symmetry under SE influence, leading to an initially symmetric walk becoming asymmetric with SE introduction. Each pixel represents an average of 1000 event trajectories. The content of this figure has been partially presented in Ref. [1].

.

red dot) remains relatively stable around $S = 0$, even at high SE rates, showing only slight deviations from the initial parameter scan in Fig. 4. This results in minor asymmetries, consistent with the observations in Fig. 5.

In contrast, the $\hat{G}_H$-walk (represented by the blue dot) develops significant asymmetries as it is located in a less stable region under the introduction of SE. With rising SE rates, the regions of asymmetry, defined by $\mathcal{C}_i^{\pm}$, shift towards larger values of γ. This shift positions the $\hat{G}_H$-coin within the asymmetric region. These findings suggest a method for designing an open quantum walk ratchet.

Within the parameter space defined by γ and α, SE induces two primary changes: A transformation from distinct stripes to more subtle patterns, and a shift of the asymmetric regions toward higher values of γ. This is detailed in Appendix A. Here, we set the shift in quasimomentum during the long free evolution between subsequent pulses to zero, thus eliminating this source of decoherence. We see that the effects of the projection operations cause the stripe pattern to perform the described movement in parameter space. The resulting asymmetry in the quantum walk is contingent on the initial positioning of the coin in this parameter space. These two effects work against each other: While the shift in γ moves the $\hat{G}_H$-walk into a zone of greater asymmetry, the overall amplitude of asymmetry diminishes due to the off-resonant nature of the walk. This implies that, within certain ranges of p_{SE}, an initially symmetric quantum walk can be intentionally configured to become highly asymmetric [1], when making SE artificially large [55].

Numerically, the effects of SE are captured through two primary mechanisms: (1) projection onto one of the internal states with a 50:50 chance, and (2) a shift in quasimomentum. To better understand these mechanisms, we investigated each effect individually. When examining only the projection effect with resonant quasimomentum, we observe a shift in the stripe patterns in Fig. 4 towards higher γ values, as illustrated in Appendix A. This shift becomes prominent at SE rates around 20%, but it is also detectable at lower rates, albeit less pronounced. The $\hat{Y}$ coin, located at $(0, 0)$, remains unaffected by this shift because the $S = 0$ line consistently intersects the origin. Conversely, the $\hat{G}_H$ coin, at $(3/2\pi, 1/2\pi)$, finds itself in a region where $S \neq 0$ due to the shifted stripes.

Incorporating the effect of quasimomentum shifts, especially during the long free evolution of a full Talbot period between subsequent kicks, which are part of the numerical SE model, introduces additional noise. This noise arises because the new quasimomentum values are drawn from a broad random distribution, masking the effects of the projection in the plot. Consequently, with both SE-induced effects combined, the clarity of the stripe shifting seen in Appendix A is diminished, which becomes clear from Fig. 6. As can be seen from Fig. 6, for SE rates $p_{\mathrm{SE}} \geq 20\%$, the data becomes significantly obscured, inspiring to focus on SE rates $p_{\mathrm{SE}} \leq 15\%$ for further studies.

Note that the numerical complexity of the carpet plots demand a reduction in numerical complexity, e.g. by calculating the pixel-rows in the images as separate jobs and overall efficient programming.

2.4 Optimizing the Quantum Walk Ratchet

The asymmetry induced by SE in the $\hat{G}_H$-walk is particularly intriguing for designing a quantum walk ratchet, as the walk is initially symmetric and the addition of noise in the simulations causes the asymmetry. This section explores the engineering of an AOKR-ratchet, analyzing both quantum and classical regimes. Previous AOKR ratchets, termed Hamiltonian ratchets [82–84], achieved symmetry breaking through initial conditions while maintaining coherent evolution. Unlike these, our system exhibits a noise-induced dissipative quantum ratchet, driven by noise-induced phase space drift. This brings forth the challenge of optimizing parameters to maximize the asymmetry of the $\hat{G}_H$-walk, thus improving the effectiveness of a SE-induced ratchet. Our analysis focuses on the $\hat{G}_H$-walk because it naturally has an inversion point, making it symmetric without SE. This symmetry is disrupted only by SE, positioning our AOKR system as an ideal candidate for a purely SE-induced ratchet.

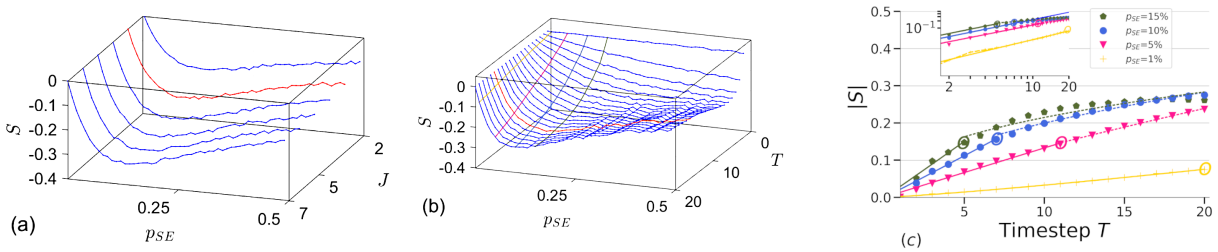

Figure 7: Dependency of the symmetry observable $S(p_{\mathrm{SE}})$ on the event probability p_{SE}. Panel (a): $S(p_{\mathrm{SE}}, J)$ for the walk conducted by the $\hat{G}_H$-coin and observed after $T = 15$ steps with an initial state of increasing width, as described by Eq. (17) and denoted by J. Panel (b): $S(p_{\mathrm{SE}}, T)$ measured at increasing numbers of timesteps T. Here the initial state is conducted by $J = 3$ momentum classes. The red curve shows the system for three momentum classes in the initial state and observed at $t = 15$ steps in the evolution, as also discussed in Fig. 10. The color coded curves represent $S(p_{\mathrm{SE}}, t)$ for fixed $p_{\mathrm{SE}} =$ 1%, 5%, 10%, 15%. These curves are shown in detail in panel (c) with their corresponding power-law fits with exponents: $a = 1$ for $p_{\mathrm{SE}} = 1\%$ for the entire time range, crossover from $a = 1$ towards $a = 0.5$ for $p_{\mathrm{SE}} = 5\% \ldots 15\%$. With increasing SE rates, the quantum regime with $a = 1$ (straight line fits) becomes shorter and shorter with respect to the crossover part (dotted lines). A circle around the corresponding data point additionally signifies the crossover. The curves and their respective fits are also shown in an inset on a double logarithmic scale. Data is obtained from averages over 10000 trajectories modeling SE [21, 68]. The content of this figure has been presented in Ref. [1].

2.4.1 Initial state dependency

The behavior of an AOKR quantum walk (QW) [9, 19, 20, 55, 57, 62, 63] fundamentally relies on the coherent Hamiltonian ratchet mechanism and the localization of initial conditions within the kicking potential [61, 63, 82, 83]. The initial state's width in momentum space, represented by the number of momentum classes J as in Eq. (17), plays a crucial role in shaping the distribution [63]. As discussed in [9] and Sec. 2.1.4, a broader initial state significantly reduces the probability accumulation near $n = 0$ for the $\hat{G}_H$-walk, resulting in a distribution with less central probability and more weight in the tails, thus enhancing asymmetry. This can be explicitly seen in Appendix A. In the walk under investigation, perfect symmetry is observed when $p_{\mathrm{SE}} = 0$. However, as SE probability continues to increases, the walk transitions to a classical behavior due to significant phase decoherence. This implies there is an optimal SE probability that maximizes asymmetry in the walk's evolution. This optimal probability exists in a regime where the walk is not yet overtaken by classical dynamics, which occurs around $p_{\mathrm{SE}} = 10\%$ and lower.

This hypothesis is supported by Fig. 7(a), which shows the dependence of the symmetry observable S on p_{SE} and J. The symmetry indicator $S(p_{\mathrm{SE}}, J)$ improves with an increasing number of momentum classes J in the initial state and reaches a maximum for $T = 15$ at approximately $p_{\mathrm{SE}} \approx 0.1$. However, from Fig. 5, we know that the regime where the resonant tails of the distribution remain visible extends up to roughly $p_{\mathrm{SE}} \approx 0.05$. This suggests that a ratchet exhibiting quantum resonance [3, 60, 61] would be most clearly observable in this regime.

The most notable enhancement in asymmetry is observed when the initial state expands from $J = 2$ to $J = 3$. This finding aligns with the results from [9] and Appendic A, as increasing J to 3 significantly reduces the probability density near $n = 0$, redistributing it towards the tails and thereby enhancing asymmetry. A similar effect is seen when increasing from $J = 3$ to $J = 4$, though the impact diminishes with broader initial states. The more localized the state is in angular θ space, the more the walks evolve with minimal dispersion. In our simulations, we generally choose $J = 3$ as it offers a balanced compromise between experimental feasibility and the magnitude of the asymmetry. It is also important to note that asymmetries do not entirely vanish, even in the classical regime.

2.4.2 Time Dependence of the Asymmetry

Exploring the temporal evolution of asymmetry is essential to determine the suitable timescales for observing this phenomenon experimentally. Figure 7(b) illustrates how $S(p_{\mathrm{SE}}, t)$ evolves over time. The red curve represents the state at $t = 15$, discussed previously in several figures. The color-coded curves show the progression of asymmetry $S(p_{\mathrm{SE}}, t)$ at various fixed p_{SE} values, detailed in Fig. 7 (c). Additionally, as the number of timesteps t increases, the maximum observable asymmetry occurs at lower p_{SE} values. This is primarily due to the influence of off-resonant quasimomentum shifts during the free evolution between subsequent pulses, which means that decoherence naturally increases over time.
The measure of S correlates with the expansion rate of the quantum walks, which is influenced by p_{SE}. Quantum walks are known for their ballistic expansion, which corresponds to an exponent of $a = 1$ in a power-law relationship, $S(t) \propto t^a$. In contrast, classical walks exhibit diffusive expansion, with an exponent of $a = 1/2$. Figure 7(c) indicates that at low SE rates $p_{\mathrm{SE}} = 1\%$, the expansion is fully quantum mechanically, characterized by $a = 1$. As p_{SE} increases, the expansion shifts from a quantum regime ($a = 1$) to a more classical regime with a reduced exponent a. At higher p_{SE} values, the behavior increasingly resembles classical diffusion, approaching an exponent of $\alpha = 1/2$. For higher event probabilities within the classical regime, the asymmetry of the walk initially increases quickly but then decreases again due to significant decoherence over time. This behavior is especially evident in the dark-green curve of Fig. 7 (c), which corresponds to an event probability of $p_{\mathrm{SE}} = 15\%$. In this case, off-resonant quasimomenta dominate the dynamics, leading to a decline in asymmetry as time progresses.
This pattern showcases the transition from quantum to classical dynamics. Increased decoherence — either due to high p_{SE} values or a combination of moderate p_{SE} and longer time intervals — results in a walk that becomes diffusive. We can identify three distinct regimes from the best-fit parameters of a power-law analysis:

- (i) The pure quantum regime, observed at $p_{\mathrm{SE}} = 1\%$.
- (ii) An intermediate regime that transitions from quantum to classical behavior over time, seen at $p_{\mathrm{SE}} = 5\%$ and 10%.
- (iii) A predominantly classical regime, evident at $p_{\mathrm{SE}} = 15\%$ and higher.

This observation is consistent with Fig. 5, where we noted the decay of resonant tails in the momentum distribution at $p_{\mathrm{SE}} = 15\%$.

2.5 Experimental Constraints

In most experimental setups, the initial state is a Bose-Einstein condensate centered around $n = 0$, but it features a quasimomentum distribution with finite width [19, 20, 77]. This is due to finite temperature of the gas, as discussed in Sec. 2.1.3. This finite quasimomentum introduces non-resonant phase effects during the time evolution of the system [3, 61]. As a result, similar to the impact of SE, quantum resonances are disturbed by these non-resonant β values.
While previous simulations assumed an initial quasimomentum of $\beta_{\mathrm{init}} = 0$, we now incorporate a more realistic Gaussian distribution for the initial quasimomentum with width β_{FWHM}, reflecting a realistic BEC at finite temperature [19, 20, 61, 77]. It turns out that a finite quasimomentum distribution without additional SE causes the asymmetric regions to concentrate around points of high asymmetry $\mathcal{C}_i^{\pm}$, as illustrated in Fig. 8(a) and (b). This leads to deviations from the original stripe pattern noted earlier in Section 2.3.1. For

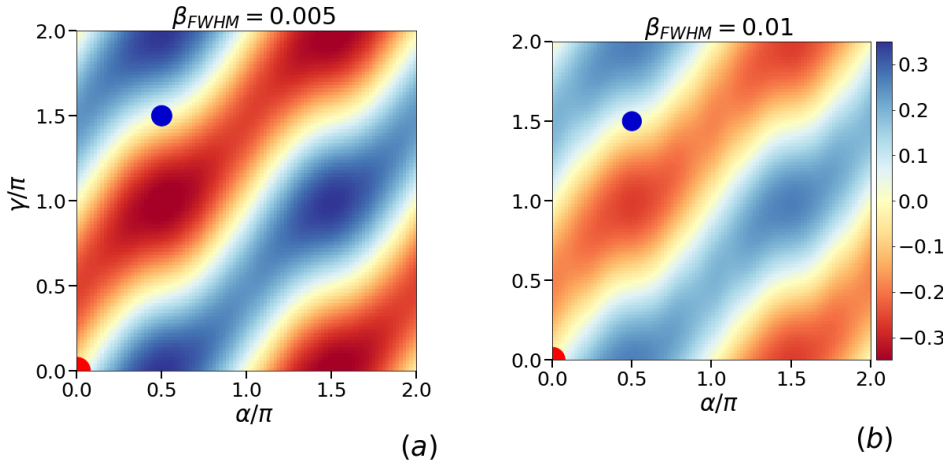

Figure 8: The symmetry indicator S is shown as a function of the free Bloch angles α and γ for different widths of the initial quasimomentum distribution. Evaluations are made after 15 steps in the walk evolution. The quasimomentum follows a Gaussian distribution with FWHM value of β_{FWHM}. Each data point in the parameter scan represents an average over 1000 trajectories. The red dot at $(\gamma = 0, \alpha = 0)$ and the blue dot at $(\gamma = 1.5\pi, \alpha = 0.5\pi)$ correspond to the $\hat{W}$-walk and $\hat{G}_H$-walk parameters, respectively The content of this figure has been presented in Ref. [1].

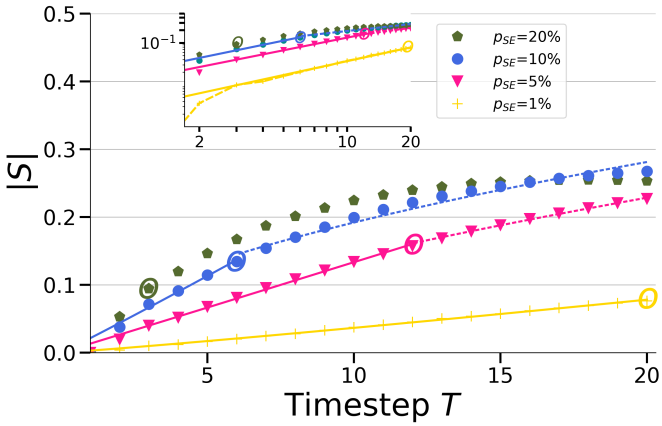

Figure 9: The figure illustrates the time evolution of the symmetry observable S, accounting for the combined influence of finite quasimomentum ($\beta_{\mathrm{FWHM}} = 0.01$) and SE. The different curves correspond to SE probabilities of $p_{\mathrm{SE}} = 1\%,\ 5\%,\ 10\%$, and 20%. Solid lines delineate the regime where a power-law fit yields an exponent of $\alpha = 1$, while dotted regions indicate the regime with $\alpha < 1$. Each curve is averaged over 200 initial quasimomenta, with each quasimomentum realized with 1000 SE trajectories. The content of this figure has been presented in Ref. [1].

broader quasimomentum distributions, shown in Fig. 8(b), the asymmetries decay, as the walks become more diffusive. However, unlike SE-induced perturbations, these broader distributions do not shift the asymmetric regions towards higher γ values. Consequently, the walks with the $\hat{G}_H$-coin and the $\hat{W}$-coin do not develop new strong asymmetries but rather become more "classical". This is numerically verified. Thus, the observed shift in asymmetric regions in Fig. 6 appears to be a unique effect to SE, not observed with other common perturbations in the AOKR framework.

The qualitative behavior of $S(\gamma, \alpha)$ under a non-resonant quasimomentum distribution is similar to the patterns observed with SE. Numerical simulations confirm that, over 20 timesteps, the quantum walk shows no significant asymmetries when influenced solely by finite quasimomentum without SE. Figure 9 illustrates the time dependence of S for different p_{SE} values, similar to Fig. 7(c), but with an added quasimomentum of $\beta_{\mathrm{FWHM}} = 0.01$. This figure demonstrates that the asymmetry effects persist even with the additional quasimomentum, which is typical in experimental settings. As in Fig. 7(c), we observe a transition from quantum to classical behavior across three distinct regimes: (i) A purely quantum mechanical regime, (ii) an initially ballistic regime that evolves into diffusive motion as decoherence sets in, and (iii) a predominantly classical regime.

Overall, this added dispersion slightly shifts the boundaries of the quantum regime (ii) compared to the scenario in Fig. 7. The other regimes (i) and (iii) are also well visible. It's worth noting that in future experimental scenarios, long pulse durations for τ_p could effectively create barriers in momentum space [60, 79, 85], also discussed in SEC. 2.1.5. This could additionally complicate the analysis for larger times when the expanding walk hits these walls. Nonetheless, quantum walks conducted with a ^{87}Rb BEC have already been observed on the discussed timescales of up to 20 timesteps [9, 19, 20, 55].

The presence of finite initial quasimomentum introduces additional dispersion, which suggests that the transition to classical behavior should occur earlier. This expectation holds only partially true. Particularly for higher event probabilities such as $p_{\mathrm{SE}} = 10\%$, the transition occurs earlier due to increased system dispersion. However for medium event probabilities $p_{SE} = 5\%$ the ballistic expansion holds for one time step longer with additional quasimomentum. It has been noted in the outlook of Ref. [4] in a different context of topological quantum walks, that little initial quasimomentum may indeed be beneficial for the stability of the system observable. There, in the so-called double kicked quantum rotor (DQKR) a quantum walk protocol is modified to have certain topological properties. In that work, phase noise within the coin was analyzed. The topological observable essentially measured the difference between the average momentum in the one internal state and the average momentum in the other internal state;

$$C(t) = \langle \psi_t | \hat{p} \otimes -\hat{\sigma}_z | \psi_t \rangle \tag{43}$$

There, it has been noted that the signal decayed under specific phase noise, but the addition of an initial quasimomentum distribution caused the topological observable to be sufficiently well visible. Unexpectedly, we have rediscovered this effect. In both cases, we have a perturbed quantum system. The decoherence destroys quantum interference, however, the addition of a different moderately small initial noise seems under certain conditions stabilizing. As we have observed this effect twice in different contexts, this is hinting towards an interesting underlying mechanism. This remains an interesting question for further research.

3 Second Chapter

3.1 Introduction

Decoherence and dissipation are inherent to the coupling of quantum systems with their environments. They pose significant challenges to the coherent control and longevity of quantum states. These interactions typically lead to the loss of quantum coherence, thus affecting applications in quantum computation and information processing [13,14]. Interestingly, further theoretical advancements highlight a counterintuitive approach: Controlled dissipation can be strategically employed to guide the dynamics of complex quantum systems, facilitating the preparation of specific quantum states critical for quantum-computational tasks [86–90] .
Ultracold atoms in optical lattices exemplify a powerful system for investigating new methods of quantum control and state engineering [91]. The precision with which both coherent dynamics and dissipative processes can be manipulated in these systems is quite notable, enabling localized control with single-site resolution [22,28–32]. This capability allows for detailed exploration of how strong interactions and controlled dissipation interplay to influence system dynamics.
In this context, phase space methods, such as the Wigner function [7, 14, 15], provide profound insights into the dynamics of quantum systems, particularly those exhibiting strong correlations. The Wigner function represents a quasi-probability distribution and serves as a cornerstone in the phase space representation of quantum mechanics [14]. It facilitates a bridge between quantum and classical descriptions by allowing quantum states to be expressed in terms of position and momentum, similar to classical phase space distributions. Utilizing the Wigner function, one can apply semiclassical approximations to complex quantum systems where exact solutions are often unfeasible [7]. This approach simplifies the dynamics into a form that resembles classical fluid dynamics, governed by a Liouvillian flow in phase space [92]. Such a representation is particularly advantageous for studying the effects of dissipation and interaction strengths on system behavior, providing a semi-classical approximation that captures essential features of the quantum dynamics.
The truncated Wigner approach [7, 23–27] proves valuable, which employs the Wigner function for systems where particle numbers are sufficiently large, thus allowing for a classical field approximation. It enables the analysis of quantum effects in a computationally accessible manner, highlighting how classical trajectories in phase space can elucidate quantum behaviors. This method effectively models how quantum systems evolve under various conditions, including the presence of strong correlations and significant dissipative effects, without the need to fully solve the complex quantum many-body problem. In this work, we will explore how the truncated Wigner approach can be applied to the many body Bose-Hubbard model to approximate the dynamics of ultracold atoms in optical lattices. By providing a detailed analysis along the line of [7] on how this method can be used to predict system behaviors under different interaction regimes and dissipative conditions, we aim to illustrate its utility in understanding this approach, discussing its limitations, and enhancing the accuracy of the approach by employing correction terms. Finding a suitable correction term for the truncated Wigner approach will be the main goal of this second part of the thesis. We will show that the solution of this approach corresponds to the mean-field solution plus additional terms. Thus the Wigner method is effectively characterized as a beyond-mean-field methodology and is therefore implicitly limited to sufficiently small atom-atom interactions and sufficiently small evolution times.

3.2 Fundamental Equations

In this section, we introduce the equations that will become relevant in the ongoing text.

3.2.1 Langevin Equation

The Langevin equation [14, 93] provides a way to describe the evolution of a system subject to both deterministic forces and random fluctuations. It's fundamental in the theory of Brownian motion [94] and more broadly in statistical mechanics. Essentially, it models the dynamics of a particle in a fluid, taking into account both friction and random forces. The equation is typically written as:

$$\frac{d\mathbf{v}}{dt} = -\gamma\mathbf{v} + \mathbf{F}(t) \tag{44}$$

where $\mathbf{v}$ is the velocity of the particle, γ is the damping coefficient, and $\mathbf{F}(t)$ represents the random force acting on the particle, which is usually modeled as a Gaussian white noise with zero mean.

3.2.2 Fokker-Planck Equation

The Fokker-Planck equation [14, 93] is a partial differential equation of second order that describes the time evolution of the probability density function of the velocity (or position) of a particle under the influence of forces, extending the description provided by the Langevin equation to a probabilistic framework. It is widely used in statistical physics, chemical kinetics, and financial mathematics. In its general form, it is expressed as:

$$\frac{\partial P}{\partial t} = -\sum_i \frac{\partial}{\partial x_i}[A_i(\mathbf{x},t)P] + \frac{1}{2}\sum_{i,j}\frac{\partial^2}{\partial x_i \partial x_j}[B_{ij}(\mathbf{x},t)P] \tag{45}$$

where P is the probability density function, A_i represents drift coefficients, and B_{ij} are diffusion coefficients. Essentially it capably describes similar processes in fluid dynamics, compared to the Langevin equation, however in a statistical ensemble picture instead of a single particle picture.

3.2.3 Korteweg de Vries Equation

The Korteweg de Vries (KdV) [95] equation is a nonlinear partial differential equation that describes the propagation of solitary waves (solitons) in a shallow water or in nonlinear wave guides. It's a fundamental equation in the study of wave phenomena and has applications in various physical contexts. The equation is given by:

$$\frac{\partial u}{\partial t} + u\frac{\partial u}{\partial x} + \frac{\partial^3 u}{\partial x^3} = 0 \tag{46}$$

where u represents the wave function, and x and t are the spatial and temporal variables, respectively. Interestingly, it is a well understood PDE of the third order which will be valuable in this work as it offers insight into equations we will recover in the ongoing work.

Korteweg-de Vries-Burgers Equation The Korteweg de Vries Burgers (KdVB) equation [96] combines the features of the KdV equation with those of the Burgers' equation, incorporating both nonlinearity and diffusion. It's used to model waves that are influenced by both nonlinear propagation effects and dissipative processes. The KdVB equation is reads as the following:

$$\frac{\partial u}{\partial t} + u\frac{\partial u}{\partial x} + \frac{\partial^3 u}{\partial x^3} = \nu\frac{\partial^2 u}{\partial x^2} \tag{47}$$

where ν is the coefficient of viscosity or diffusion, representing the dissipative effect. It will be of interest for us as it has a dissipative term, such as the Fokker-Planck equation, and an additional term of third order.

3.2.4 Gross-Pitaevskii equation

The Gross-Pitaevskii equation (GPE) [14, 97–99] is a fundamental nonlinear partial differential equation (PDE) that describes the macroscopic wave function of a Bose-Einstein condensate (BEC) at temperatures close to absolute zero. It provides a mean-field approximation for the dynamics of interacting bosons, capturing the essence of quantum coherence and superfluidity in dilute atomic gases. The equation is given by:

$$i\hbar\frac{\partial\psi(\mathbf{r},t)}{\partial t} = \left[-\frac{\hbar^2}{2m}\nabla^2 + V(\mathbf{r}) + g|\psi(\mathbf{r},t)|^2\right]\psi(\mathbf{r},t),$$

where $\psi(\mathbf{r},t)$ is the macroscopic wave function, m is the mass of the bosons, $V(\mathbf{r})$ is the external trapping potential, and $g = 4\pi\hbar^2 a/m$ characterizes the strength of the interatomic interactions with a being the scattering length.

The GPE's cubic nonlinearity, represented by $|\psi(\mathbf{r},t)|^2\psi(\mathbf{r},t)$, captures the mean-field interaction among bosons. The equation effectively describes both the ground state of the BEC and its low-energy excitations, including collective oscillations and sound modes. Furthermore, it accounts for the superfluid behavior of BECs [100], manifesting in features like quantized vortices [101, 102] and persistent currents [103].

In specific regimes, the GPE can be simplified to lower-dimensional forms [104], which is particularly useful for investigating quasi-1D systems. The equation's accessability to numerical methods [99] allows for detailed simulations of BEC mean-field dynamics under various conditions, making it a powerful tool for exploring the interplay between nonlinearity, and mean-field quantum statistics [7].

3.3 The Bose-Hubbard model

The Bose-Hubbard model offers a quintessential framework for the examination of interacting bosonic particles on a lattice, elucidating critical aspects of their quantum dynamics. Originating to explore the phenomena of superfluidity and the Mott insulator transition within condensed matter physics [105–107], its relevance extends across quantum optics, atomic physics, and the broader realm of quantum many-body physics. The model's governing Hamiltonian is then formulated by the famous Bose Hubbard Hamiltonian [14, 108]:

$$\hat{H} = -J \sum_{\langle i,j \rangle} (\hat{a}_i^\dagger \hat{a}_j + \hat{a}_j^\dagger \hat{a}_i) + \frac{U}{2} \sum_i \hat{n}_i (\hat{n}_i - 1) - \mu \sum_i \hat{n}_i \tag{48}$$

Here, $\hat{a}_i^\dagger$ and $\hat{a}_i$ denote the boson creation and annihilation operators at lattice site i, respectively, with $\hat{n}_i = \hat{a}_i^\dagger \hat{a}_i$ being the number operator. The parameter J represents the hopping amplitude, encapsulating the kinetic energy associated with particles traversing between adjacent sites i and j. The on-site interaction strength is denoted by U, and μ is the chemical potential that modulates the total number of particles. By setting $\hbar = 1$, energy is measured in frequency units.
The interplay between the kinetic term J and the interaction term U fundamentally defines the model's dynamics. Thus, U/J is the relevant system parameter. For low U/J ratios, particles exhibit delocalized wave-like behavior indicative of superfluidity [109]. Conversely, high U/J values lead to particle localization [110] at discrete lattice sites, indicating the presence of a Mott insulator phase marked by an excitation spectrum gap and diminished phase coherence [111]. Critical to the Bose-Hubbard model is its depiction of quantum phase transitions, transitions between distinct quantum states driven predominantly by quantum fluctuations. Theoretical exploration of these transitions leverages a spectrum of analytical and numerical methods, including mean-field theory [112,113], perturbation theory [114], quantum Monte Carlo simulations [115], and the density matrix renormalization group [110]. Experimental realizations of the Bose-Hubbard model using ultracold atomic gases in optical lattices have confirmed theoretical predictions and expanded the investigative scope of quantum phase transitions [17,18]. These experimental platforms offer high control over model parameters, thereby enhancing our understanding of complex quantum phenomena. The Bose-Hubbard model remains a cornerstone in the study of quantum phase transitions, providing an invaluable framework for probing the intricate balance between kinetic energy and interactions within quantum many-body systems. Its applicability to a diverse array of physical phenomena highlights its foundational role in contemporary physics. Its Hamiltonian will be the fundament for exploring ultra-cold quantum gases.

Open Bose Hubbard System Optical lattices provide exceptional control over the quantum dynamics of ultracold atoms [17, 18, 116]. Experimental parameters, such as the strength of atom-atom interactions, can be finely tuned by varying the lattice depth. Previous experiments have demonstrated the ability to locally control atomic dynamics. Single-site access can be achieved by either increasing the lattice period or enhancing the resolution of the optical imaging system. These advanced imaging systems allow measurement of the atom number per site. Higher resolution can be obtained using a focused electron beam, which, despite its dissipative nature, enables the detection of single atoms with outstanding spatial resolution. This motivates the investigation of the open Bose Hubbard system, where particle loss and decoherence are prevalent.
The coherent dynamics of ultracold atoms in deep optical lattices are described by the Bose-Hubbard Hamiltonian introduced in Sec. 3.3, where we set the chemical potential to zero $\mu = 0$:

$$\hat{H} = -J \sum_j \left(\hat{a}_{j+1}^\dagger \hat{a}_j + \hat{a}_j^\dagger \hat{a}_{j+1} \right) + \frac{U}{2} \sum_j \hat{a}_j^\dagger \hat{a}_j^\dagger \hat{a}_j \hat{a}_j. \tag{49}$$

In the context of optical lattices, this model assumes a sufficiently deep lattice, ensuring that dynamics occur within the lowest Bloch band. Throughout this work, we consider finite lattices with M sites and periodic boundary conditions, In this work we will use both open boundary conditions and also periodic boundary conditions, identifying sites $j = 0$ and $j = M$.

This work explores the non-equilibrium dynamics triggered by localized dissipation, implemented experimentally either by a resonant laser or a focused electron beam. Atoms are removed rapidly and irreversibly from the lattice, allowing the dissipative dynamics to be described by a Markovian master equation [117]:

$$\frac{d}{dt}\hat{\rho} = -i[\hat{H}, \hat{\rho}] + \mathcal{L}\hat{\rho}. \tag{50}$$

Particle loss is modeled by the Liouvillian [5–7, 117–119]:

$$\mathcal{L}_{\text{loss}}\hat{\rho} = -\frac{1}{2}\sum_j \gamma_j \left(\hat{a}_j^\dagger \hat{a}_j \hat{\rho} + \hat{\rho}\hat{a}_j^\dagger \hat{a}_j - 2\hat{a}_j \hat{\rho} \hat{a}_j^\dagger\right), \tag{51}$$

where γ_j denotes the loss rate at site j. Additionally, phase noise arises from collisions with background gas [120–122] or from photon absorption and spontaneous emission from the lattice beams [123]. This noise is described by the following Liouvillian:

$$\mathcal{L}_{\text{noise}}\hat{\rho} = -\frac{\kappa}{2}\sum_j \left(\hat{n}_j^2 \hat{\rho} + \hat{\rho}\hat{n}_j^2 - 2\hat{n}_j \hat{\rho} \hat{n}_j\right). \tag{52}$$

Phase noise can be minimized by detuning the optical lattice far from the atomic resonance, allowing us to assume $\kappa = 0$. For numerical implementations, we utilize the quantum jump method [124, 125], decomposing the density matrix $\hat{\rho}$ into state vectors:

$$\hat{\rho} = \frac{1}{L}\sum_{\ell=1}^{L} |\psi_\ell\rangle\langle\psi_\ell|, \tag{53}$$

with continuous evolution interrupted by stochastic quantum jumps. The continuous evolution follows the Schrödinger equation with the effective non-Hermitian Hamiltonian:

$$\hat{H}_{\text{eff}} = \hat{H} - \frac{i}{2}\sum_j \gamma_j \hat{a}_j^\dagger \hat{a}_j - \frac{i\kappa}{2}\sum_j \hat{n}_j^2. \tag{54}$$

Since $\hat{H}_{\text{eff}}$ is non-Hermitian, the state vector $|\psi\rangle$ must be renormalized after each time step. In the case of particle loss, the state vector undergoes a jump:

$$|\psi\rangle \to \frac{\hat{a}_j|\psi\rangle}{\|\hat{a}_j|\psi\rangle\|}, \tag{55}$$

with a probability:

$$\delta p = \gamma_j \langle\psi|\hat{a}_j^\dagger \hat{a}_j|\psi\rangle \delta t, \tag{56}$$

during a short time interval δt. In the event of particle loss, the systems particle number may reduce from 1 to M fewer particles, depending on the number of sites on which an event occours. Consequently, the basis must be recalculated with the corresponding parameters of the time-evolved system, but adjusted to the new particle number and the corresponding new system size. The full density matrix is reconstructed by use of the quantum trajectory method described in [14], by averaging over numerous random trajectories in state space.

In this work, we investigate two model systems: an open Bose-Hubbard system with loss at a single site and periodic boundary conditions, and an extended one-dimensional optical lattice with localized loss from a single site. These models allow us to explore the impact of localized dissipation and phase noise on the quantum dynamics of ultracold atoms in optical lattices along the line of [7].

We simulate the dynamics for a triple well system with decay only in the middle well and a symmetric initial BEC-state, as the system size allows to be accurately computed with reasonable numerical effort.

$$|\psi_0\rangle_\pm = \frac{1}{2^N\sqrt{N!}}(\hat{a}_1^\dagger \pm \hat{a}_2^\dagger)^N|0\rangle, \tag{57}$$

Where N represents the total particle number in the system. $|\psi\rangle_+$ is called the symmetric state and $|\psi\rangle_-$ is called the anti-symmetric state. The most obvious effect of decay is the decrease of the total particle number. The dissipation may cause the quantum state to end up in a very different state than the initial state. This behavior can be characterized by the first order correlation function between wells j and l. The first order correlation function reads as the following:

$$g_{jl}^{(1)} = \frac{\langle\hat{a}_j^\dagger \hat{a}_l\rangle}{\sqrt{\langle\hat{n}_j\rangle\langle\hat{n}_l\rangle}}. \tag{58}$$

Density fluctuations are then characterized by the second-order correlation function:

$$g_{jl}^{(2)} = \frac{\langle \hat{n}_j \hat{n}_l \rangle}{\langle \hat{n}_j \rangle \langle \hat{n}_l \rangle}. \tag{59}$$

The system's dynamics are illustrated in Fig. 10. The upper row shows the systems dynamics for the symmetric initial state and the lower row for the anti-symmetric initial state. For the symmetric initial state, the first panel shows the decay of the total particle number due to loss in the middle well. Increased onsite energy results in reduced decay for our initial symmetric BEC state, which is intuitive since particles are initially placed in the first and third sites. Higher values of U lead to a more localized system, causing atoms to transition more slowly to the dissipative middle well. In contrast, lower values of U facilitate particle hopping to adjacent wells, thereby enhancing particle loss. The correlation functions present more complex behaviors. For the symmetric state, the correlation functions exhibit only slight fluctuations. However, for the anti-symmetric state, there is a notable dependence of the observables on U/J. At both small ($U = 0.01J$) and large ($U = 0.4J$) onsite energies, there are minimal density fluctuations in g_{13}^2. Counterintuitively, at the intermediate value ($U = 0.1J$), the density fluctuations in g_{13}^2 are most pronounced. For the first-order correlation, higher values of U/J lead to a faster loss of correlation in g_{13}^1. Typically, coherent states have $g_{ij}^1 = 1$, which is the maximal obtainable correlation and $g_{ij}^2 = 1$. Thermal chaotic light with bunching can cause the second-order correlation to approach 2, where repulsive effects can cause anti-bunching with $g_{ij}^2 < 1$. A more detailed discussion can be found in [7,14]. In our simulations g_{ij}^1 and g_{ij}^1 start at 1 for $t = 0$, which is expected, as the initial states are a superposition of coherent states. Also, $g_{13}^1 \leq 1$ and $0 \leq g_{13}^1 \leq 2$ for all times, as expected. Following [7], we have chosen $U = 0.01J$ and $U = 0.1J$ for comparison, and our results are consistent with those findings. Furthermore these curves will be our reference to compare more approximate methods for the many-body Hamiltonian.

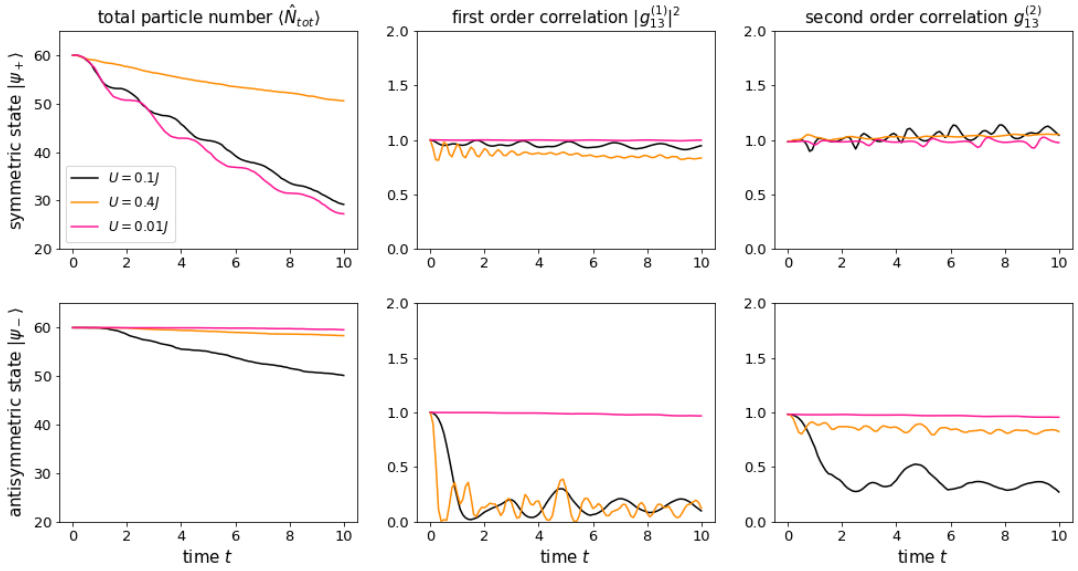

Figure 10: Presented are simulations for the open Bose-Hubbard system for different interaction strengths and different initial states. The upper row shows the observables for the symmetric initial state $|\psi\rangle_+$ and the lower row corresponds to the antisymmetric initial state $|\psi\rangle_-$. Shown is the total particle number in the system $\langle \hat{N}_{tot} \rangle$ and the first and second-order correlation $g_{13}^{(1)}$ and $g_{13}^{(2)}$. The pink line corresponds to $U = 0.01J$, the black line to $U = 0.1J$ and the yellow line to $U = 0.4J$. The decay is only present in the middle well $\gamma_2 = 0.2$. The results are in agreement with the figures from [7].

3.4 The Wigner function

The Wigner function is a fundamental concept for quantum mechanical many-body systems, representing a quasi-probability distribution in phase space for a quantum system. This statement is shown in Appendix B. Defined as the Fourier transform of the quantum characteristic function, the Wigner function provides a complete description of the quantum state. Mathematically, for a density matrix $\hat{\rho}$, the Wigner function $\mathcal{W}(\alpha, \alpha^*)$ is given by [14]:

$$\mathcal{W}(\alpha, \alpha^*) = \frac{1}{\pi^2} \int d^2\beta \, \exp(\beta^*\alpha - \beta\alpha^*) \chi_{\mathcal{W}}(\beta, \beta^*), \tag{60}$$

where

$$\chi_{\mathcal{W}}(\beta, \beta^*) = \mathrm{Tr}\left(\hat{\rho}\exp(\beta\hat{\mathrm{a}}^\dagger - \beta^*\hat{\mathrm{a}}\right) \tag{61}$$

is the characteristic function. The operator $\hat{D}(\beta) = \exp(\beta\hat{\mathrm{a}}^\dagger - \beta^*\hat{\mathrm{a}})$ is the displacement operator.
The Wigner function is particularly useful because it allows for the visualization of quantum states in a manner analogous to classical phase space distributions, bridging a gap between classical and quantum descriptions. Interestingly, it is possible to translate the system into this semiclassical framework without loss of information. This is done by the use of operator correspondences which make no additional assumptions. This way the Wigner function facilitates the analysis of quantum coherence and interference phenomena and provides insights into non-classical effects such as entanglement and squeezing [126–128]. Moreover, the Wigner function's formulation makes it applicable to various numerical methods, enabling efficient simulations of quantum dynamical systems and offering a powerful tool for studying complex quantum systems, which are otherwise quickly out of range for numerical purposes.

3.4.1 Operator Correspondence

First and foremost the Wigner function is a theoretical idea which allows to translate the viewpoint from a purely quantum mechanical perspective to a semiclassical phase space approach. Of course the most interesting question is how to calculate observables of interest in this framework. This will be discussed in detail in this chapter.
The quintessential idea is to treat the Wigner function as a quasiprobability-density (see Appendix B) and to calculate observables accordingly. Thus, to calculate the time dependence of an observable we need to evaluate the time dependence of the initial Wigner function. The master equation in Lindblad form for an open Bose Hubbard system is given by Eq. (50). One needs a mapping from this equation to an equation of motion for the Wigner function. The translation is made by the following operator correspondences, which we have calculated in Appendix D.1:

$$\left(\alpha + \frac{\partial}{\partial\alpha^*}\right)\mathcal{W} \longleftrightarrow \hat{a}\hat{\rho} \tag{62}$$

$$\left(\alpha - \frac{\partial}{\partial\alpha^*}\right)\mathcal{W} \longleftrightarrow \hat{\rho}\hat{a} \tag{63}$$

$$\left(\alpha^* - \frac{\partial}{\partial\alpha}\right)\mathcal{W} \longleftrightarrow \hat{a}^\dagger\hat{\rho} \tag{64}$$

$$\left(\alpha^* + \frac{\partial}{\partial\alpha}\right)\mathcal{W} \longleftrightarrow \hat{\rho}\hat{a}^\dagger \tag{65}$$

These correspondences allow to translate from one framework to the other without loss of information. It is important to note that the operator correspondences make no additional assumptions, thus allowing to perform this translation without loss of information.

3.4.2 Hierarchy approach - Why do we need truncated Wigner?

To understand the system's dynamics, we need to investigate the particle number and the correlation functions $g_{jl}^{(1)}$ and $g_{jl}^{(2)}$. The time evolution for the correlation functions of increasing order can be done analytically and is known as the hierarchy method. However this comes with a few problems which we will illustrate for the first-order correlation function in the noise-free scenario ($\gamma_j = 0$). To calculate the first order correlation

function g^1_{jl} we need to calculate the time evolution of the single particle reduced density matrix [113,129,130] $\sigma_{jk} = \langle \hat{a}^\dagger_j \hat{a}_k \rangle = tr(\hat{a}^\dagger_j \hat{a}_k \hat{\rho})$, given by:

$$i\frac{d\hat{\sigma}_{jk}}{dt} = tr(\hat{a}^\dagger_j \hat{a}_k [\hat{\mathcal{H}}, \hat{\rho})]). \tag{66}$$

This time evolution is explicitly calculated in the material Appendix C for the noise free scenario and reads the following:

$$i\frac{d\hat{\sigma}_{jk}}{dt} = -J\left(\sigma_{j,k+1} + \sigma_{j,k-1} - \sigma_{j+1,k} - \sigma_{j-1,k}\right) + U\left(\Delta_{kkkj} + \sigma_{kk}\sigma kj - \Delta_{jjjk} - \sigma_{jj}\sigma_{jk}\right), \tag{67}$$

where we defined:

$$\Delta_{jklm} = \langle \hat{a}^\dagger_j \hat{a}_k \hat{a}^\dagger_l \hat{a}_m \rangle - \langle \hat{a}^\dagger_j \hat{a}_k \rangle \langle \hat{a}^\dagger_l \hat{a}_m \rangle = \langle \hat{a}^\dagger_j \hat{a}_k \hat{a}^\dagger_l \hat{a}_m \rangle - \sigma_{jk}\sigma_{lm}. \tag{68}$$

By employing operator correspondences in these equations, we can translate these equations in the phase space picture and evaluate the systems observable in the context of the Wigner function.

Now the issue becomes obvious: The trace effectively "kills" two operators which means that in the calculation of the time evolution of $\hat{\sigma}_{jk}$ terms of the order Δ_{jklm} are involved. Thus, when employing the operator correspondences from Eqs. (62)-(65) in the hierarchy, we realize that the calculations involve fourth-order derivatives already for the first-order correlatios. Similarly, the time evolution for $\hat{\Delta}_{jklm}$, necessary for the second order correlation function $g^{(2)}_{jl}$, would involve already sixth order derivatives, which becomes clear by the calculations in Appendix C. This complexity continues to escalate with higher-order correlations. As already stated above, this is because the trace operation effectively reduces the number of operators by two, amplifying the order of the derivatives required when using the operator identities. Consequently, the computational effort to evaluate the correlation functions grows rapidly, making them challenging to solve and quickly exceeding the limits of numerical feasibility. Practically, to obtain a closed set of evolution equations, the equations are truncated [5, 129].

In contrast, the so-called truncated Wigner approach [7, 23–27] offers a more tractable solution. In contrast to the hierarchy approach, the system is translated in the semiclassical phase space framework of the Wigner function. The time evolution of the Wigner function is translated into a set of stochastic differential equations (SDEs). Therefore higher order terms are truncated, which gives the method its name. These equations can be straightforwardly solved using straightforward numerical methods, making the approach significantly more accessible for practical computations.

3.5 Truncated Wigner approach

Understanding the dynamics of strongly correlated systems, such as those described by the Hubbard model, is essential for uncovering the underlying mechanisms A direct attempt to solve the master equation as described in Sec. 3.3, while precise, faces significant computational hurdles, limiting the applicability of the approach to small systems or requiring approximations that may overlook critical phenomena. The truncated Wigner approach [7, 23–27] represents a methodological advancement, enabling the study of larger systems and non-equilibrium dynamics within the Hubbard model. By simplifying the quantum dynamics into a form amenable to numerical simulation, this method retains essential quantum mechanical characteristics, allowing for the exploration of the temporal evolution in a computationally efficient manner.

To achieve this the approach one translates the master equation Eq. (50) into the context of the quasi-probabilistic Wigner picture, using the operator correspondences from Eqs.(62)-(65). From here one truncates everything that goes beyond the second order, allowing to map the system on a Fokker-Planck equation. Instead of solving the time evolution of the probability density function itself, one goes from an "ensamble-pictue" into a "single-particle-picture", by mapping the Fokker-Planck equation onto stochastic Langevin-equations. These describe the time evolution for one point in the distribution. The time-evolved distribution of the probability density is then recovered by taking an average over a sufficiently large ensemble of time-evolved points, where the initial value of those points was sampled from the initial Wigner function. The stochastic equations themselves will correspond to the discrete Gross-Pitaevskii-equation plus an additional stochastic term, which means that the truncated Wigner approach will take a grasp of the physics beyond

the mean-field solution.

This chapter focuses on the application of the truncated Wigner approach to the Hubbard model, aiming to elucidate its capability in capturing the dynamics of correlated atoms. We discuss the theoretical foundation of the method and its implementations.

3.5.1 Time evolution of the Wigner function

We use the operator correspondences from above Eqs.(62)-(65), which are now true for each well independently:

$$\hat{a}_j \rho \longleftrightarrow \left(\alpha_j + \frac{1}{2}\frac{\partial}{\partial \alpha_j^*}\right)\mathcal{W} \tag{69}$$

$$\rho \hat{a}_j \longleftrightarrow \left(\alpha_j - \frac{1}{2}\frac{\partial}{\partial \alpha_j^*}\right)\mathcal{W} \tag{70}$$

$$\hat{a}_j^\dagger \rho \longleftrightarrow \left(\alpha_j^* - \frac{1}{2}\frac{\partial}{\partial \alpha_j}\right)\mathcal{W} \tag{71}$$

$$\rho \hat{a}_j^\dagger \longleftrightarrow \left(\alpha_j^* + \frac{1}{2}\frac{\partial}{\partial \alpha_j}\right)\mathcal{W}. \tag{72}$$

Here the index j denotes the operator correspondence for the $j\acute{}$th well. These correspondences are used to translate the master equation into a dynamical equation for the Wigner function. We insert the operator correspondences in the masterequation and recover the following result:

$$\begin{aligned}
&\frac{d}{dt}\hat{\rho}(t) = -i[\hat{\mathcal{H}}, \rho(t)] + \hat{\mathcal{L}}_{\text{loss}}\hat{\rho}(t) \\
&\leftrightarrow \partial_t \mathcal{W} = 2J \sum_j \text{Im}\left[\left(\alpha_j - \frac{\partial}{\partial \alpha_j^*}\right)\left(\alpha_{j+1}^* + \frac{\partial}{\partial \alpha_{j+1}}\right) - \left(\alpha_{j+1}^* - \frac{\partial}{\partial \alpha_{j+1}}\right)\left(\alpha_j + \frac{\partial}{\partial \alpha_j^*}\right)\right]\mathcal{W} \\
&+ U \sum_j \text{Im}\left[\left(\alpha_j^* - \frac{\partial}{\partial \alpha_j}\right)^2\left(\alpha_j + \frac{\partial}{\partial \alpha_j^*}\right)^2\right]\mathcal{W} - \sum_j \frac{\gamma_j}{2}\left[\left(\alpha_j^* - \frac{\partial}{\partial \alpha_j}\right)\left(\alpha_j + \frac{\partial}{\partial \alpha_j^*}\right)\right. \\
&\left. + \left(\alpha_j^* + \frac{\partial}{\partial \alpha_j}\right)\left(\alpha_j - \frac{\partial}{\partial \alpha_j^*}\right) - 2\left(\alpha_j + \frac{\partial}{\partial \alpha_j^*}\right)\left(\alpha_j^* + \frac{\partial}{\partial \alpha_j}\right)\right]\mathcal{W}.
\end{aligned} \tag{73}$$

A step by step derivation is presented in Appendix D.2. When splitting α and α^* into real and imaginary part

$$\alpha = x + iy \tag{74}$$

$$\alpha^* = x - iy, \tag{75}$$

we recover the following dynamical equation:

$$\begin{aligned}\frac{d}{dt}\hat{\rho}(t) \leftrightarrow \partial_t \mathcal{W} = &\sum_j \left[\frac{\partial}{\partial x_j}\left(2J(y_{j+1}+y_{j-1}) - 2U(x_j^2 y_j + y_j^3) + \frac{\gamma_j}{2}x_j\right)\right]\mathcal{W} \\ &+ \sum_j \left[\frac{\partial}{\partial y_j}\left(-2J(x_{j+1}+x_{j-1}) + 2U(x_j y_j^2 + x_j^3) + \frac{\gamma_j}{2}y_j\right)\right]\mathcal{W} \\ &+ \frac{1}{2}\sum_j \gamma_j \left(\frac{\partial^2}{\partial x_j^2} + \frac{\partial^2}{\partial y_j^2}\right)\mathcal{W} \\ &+ U\sum_j \left[y_j\left(\frac{\partial^2}{\partial x_j^3} + 3\frac{\partial}{\partial x_j}\frac{\partial^2}{\partial y_j^2}\right) - x_j\left(\frac{\partial^3}{\partial y_j^3} + 3\frac{\partial^2}{\partial x_j^2}\frac{\partial}{\partial y_j}\right)\right]\mathcal{W},\end{aligned} \tag{76}$$

which involves up to third order terms for the derivatives. If we would allow phase noise for our system up to fourth-order derivatives would be possible. As this effect can be controlled we deem this version of the Wigner function sufficient. Detailed derivations along the line of [7] are also found in Appendix D.2. Eq. (76) describes the time evolution of the Wigner function and is thus the fundament for our ongoing analysis.

3.5.2 Mapping on Stochastic Equations

In the context of the Truncated Wigner approximation, we omit higher-order interaction terms, including the final summation containing higher-order derivatives, retaining terms only up to the second order. Thereby reducing the complexity of our problem to a second order, which enables the following methodology. When truncating the higher-order interaction terms we recover the following differential equation:

$$\begin{aligned}\frac{d}{dt}\hat{\rho}(t) \leftrightarrow \partial_t \mathcal{W} = &\sum_j \left[\frac{\partial}{\partial x_j}\left(2J(y_{j+1}+y_{j-1}) - 2U(x_j^2 y_j + y_j^3) + \frac{\gamma_j}{2}x_j\right)\right]\mathcal{W} \\ &+ \sum_j \left[\frac{\partial}{\partial y_j}\left(-2J(x_{j+1}+x_{j-1}) + 2U(x_j y_j^2 + x_j^3) + \frac{\gamma_j}{2}y_j\right)\right]\mathcal{W} \\ &+ \frac{1}{2}\sum_j \gamma_j \left(\frac{\partial^2}{\partial x_j^2} + \frac{\partial^2}{\partial y_j^2}\right)\mathcal{W}.\end{aligned} \tag{77}$$

Consequently, this approximation yields a multi-dimensional Fokker-Planck equation [93], which is in its most general form described as:

$$\partial_t \mathcal{W} = -\sum_i \frac{\partial}{\partial z_i} A_i(\vec{z},t)\mathcal{W} + \frac{1}{2}\sum_{i,k}\frac{\partial}{\partial z_i}\frac{\partial}{\partial z_k}[B(\vec{z},t)B^T(\vec{z},t)]\mathcal{W}. \tag{78}$$

Here, the diffusion matrix $D(\vec{z},t)$ is defined as $D(\vec{z},t) = \frac{1}{2}B(\vec{z},t)B^T(\vec{z},t)$. The mapping to the Truncated Wigner equation's formalism is accomplished through the identification of:

$$\vec{z}_j = (x_j, y_j)^T \tag{79}$$

$$\vec{A}_j(t) = \begin{pmatrix} 2J(y_{j+1}+y_{j-1}) - 2U(x_j^2 y_j + y_j^3) + \frac{\gamma_j}{2}x_j \\ -2J(x_{j+1}+x_{j-1}) + 2U(x_j y_j^2 + x_j^3) + \frac{\gamma_j}{2}y_j \end{pmatrix} \tag{80}$$

$$B_j(\vec{z},t) = \sqrt{\gamma_j}\mathbf{1}. \tag{81}$$

The aim is to reformulate the system into a series of stochastic equations, utilizing Ito's theorem as the foundation. The Fokker-Planck equation and stochastic differential equations are linked via the Feynman-Kac formula, utilizing Ito's theorem. A derivation for the Feynman-Kac formula can be found in chapter 4.3 of [93]. Similarly one can derive a connection between the Stradonovitch SDE and the Fokker Planck equation. (See chapter 4.3 of [93].) One way or the other we find the following connection between the Fokker-Planck equation and the stochastic Ito-equation;

$$\frac{d\vec{z}}{dt} = \vec{A}(\vec{z},t) + B(\vec{z},t)\vec{E}(t). \tag{82}$$

In this framework, the noise sources $E_j(t)$ are modeled as a Wiener process with zero mean, characterized by their temporal and spatial uncorrelated nature, satisfying $\langle E_j(t)E_k(t')\rangle = \delta_{jk}\delta(t-t')$. Consequently, these noise terms are expressed as:

$$\vec{E}_j = (\zeta_j, \eta_j), \tag{83}$$

where ζ_j and η_j adhere to the aforementioned statistical properties. With these definitions in place, we decompose our system into a collection of stochastic equations:

$$\frac{dx_j}{dt} = -2J(y_{j+1}+y_{j-1}) + 2U(x_j^2 y_j + y_j^3) - \frac{\gamma_j}{2}x_j + \sqrt{\gamma_j}\zeta_j \tag{84}$$

$$\frac{dy_j}{dt} = 2J(x_{j+1}+x_{j-1}) - 2U(x_j y_j^2 + x_j^3) - \frac{\gamma_j}{2}y_j + \sqrt{\gamma_j}\eta_j. \tag{85}$$

The transition from a Fokker-Planck to a Langevin framework might be understood more intuitively in the context of fluid dynamics, which historically emerged in the context of Brownian motion. The Langevin equation originally described the trajectory of a single particle in a fluid, influenced by random collisions manifesting as a stochastic force. Conversely, the Fokker-Planck equation conceptualizes similar physical phenomena across an ensemble of particles, portraying the collective behavior as a diffusive process. The inherent mathematical linkage between these two descriptions underscores their complementary nature.
The noise terms may be interpreted as the influence of the operator commutation relations, as opposed to particle collisions. This distinction highlights the theoretical underpinnings of our model, emphasizing the role of quantum mechanical principles in shaping the behavior of the system under this semi-classical investigation.
We also see that these Langevinian equations are effectively discrete mean-field Gross-Piteavskii equations [129,131,132] plus an additional stochastic term. Solving the system using this mapping on the Langevin equations enables a granular analysis at the "particle" level, facilitating a Monte Carlo simulation strategy. By initializing a set of particles based on a predefined distribution, we can iteratively compute their temporal evolution. In our context this means to sample the real and complex part of the amplitude operator expectation values from an according initial distribution and calculate their trajectory in time. This methodology yields a numerical approximation of the system's final state distribution by a statistical approach.

3.5.3 Initial state sampling

We translated the quantum mechanical master equation into an equation of motion for a quasiprobability, representing the system's dynamics in phase space. Furthermore we have truncated this equation, allowing the mapping on a Fokker-Planck equation. Then we translated the many-particle ensemble picture to stochastic equations of motion for singular points within this ensemble. The resulting equations only involve first-order derivatives and are numerically trivial to solve. Since we are still challenged by computing the time evolution, not just for singular points, but the complete probability distribution we are taking a Monte-Carlo approach. Given some initial state one is challenged to find the corresponding Wigner function and create random sample values in accordance with this initial distribution. Each point in the sample may then be evolved according to Eqs.(84)-(85).

Remember that in Sec. 3.3 we have described the initial state by a symmetric BEC-state of the form:

$$\psi_0 = \frac{1}{2^N\sqrt{N!}}\left[\sum_{j=1}^{M} w_j \hat{a}_j^\dagger\right]^N |0\rangle. \tag{86}$$

Here N reflects the total particle number, M is the number of wells and w_j is the amplitude in the $j´$th well. In Sec. 3.3 we discussed an initial state with $M = 3$ and $w_1 = w_3 = 1$ and $w_2 = 0$. This state may be interpreted by a superposition of all combinatorial possibilities for distributing N particles on M wells, where each well is weighted by w_j in the final state. Thus, for every individual site, one may interpret this state similar to a Poisson distribution in Fock space, which for large enough N approaches a Gaussian distribution. Thus the distribution in Fock space for each site individually can easily be approximated by a coherent state, who has very similar features in terms of its distribution in Fock space. Thus, we are starting from an initial state expressed as a product state:

$$|\psi(t=0)\rangle = |\psi_1\rangle|\psi_2\rangle...|\psi_M\rangle, \tag{87}$$

where $|\psi_j\rangle$ represents a Glauber coherent state in the $j´$th well. This state configuration is characteristic of a pure Bose-Einstein Condensate (BEC) within the grand canonical framework, attributable to its coherent state nature. The Wigner function for a coherent state, $\rho = |\psi_j\rangle\langle\psi_j|$, is straightforward to calculate. A step by step computation is presented in Appendix D.3. As presented in [14] and evident from the calculations in the Appendix material, the Wigner function for a Glauber coherent state is a Gaussian:

$$\mathcal{W}(\alpha, \alpha^*) = \frac{2}{\pi}\exp(-2|\alpha_j - \psi_j|^2). \tag{88}$$

Eqs. (84) and (85) are our equations of motion for sample points within phase space. Without the noise term, these correspond to the free Gross-Pitaevskii equation. For a BEC in a Bloch state with quasimomentum k, the solution to the free Gross-Pitaevskii equation is well known to be:

$$\psi_j = e^{ikj}\sqrt{\frac{N_j}{M}}, \tag{89}$$

with N_j being the weighted particle number in the $j´$th well. This centers our Gaussian around this value ψ_j. Since we are analyzing a symmetric BEC state instead of an anti-symmetric BEC state we have no relative phase rotation of 180° between our functionals in the occupied wells. Thus, the BEC is located at k=0 in the Brillouin zone. (For an anti-symmetric state as also analyzed in [7] one should use $k = \pi$.)

Continuing from the initial setup, we sample initial values for $\alpha_j = x_j + iy_j$ from a Gaussian distribution. The mean of this distribution is set with ψ_j, and the standard deviation given by 1/2, which becomes evident from Eq. (88). (Note that the equation given above corresponds to a complex or two-dimensional Gaussian.)

$$\alpha_j \in \mathcal{N}\left(\psi_j, (\sigma = \frac{1}{2})^2\right) \tag{90}$$

Once the initial values are sampled, we proceed to evolve x_j and y_j according to their respective stochastic differential equations Eqs. (84) and (85). We implement a simple Euler integration scheme with a sufficiently small step size to ensure convergence. This approach allows us to effectively propagate the initial distribution through the dynamical system, thereby obtaining a sampled representation of the final distribution as a numerical average. This method leverages the power of Monte Carlo simulations to approximate the evolution of the Wigner function, thus providing a practical means to explore the system's behavior over time. Now one could start to reconstruct the final distribution of the Wigner function, using some sort of a kernel function. From there we could again treat the Wigner function as a probability function and calculate desired observables accordingly. This would be numerically intensive. However we can push it even further, so we never need the final form of the Wigner function itself.

3.5.4 Observables

As discussed in Sec. (B) the Wigner function serves as a semiclassical phase-space probability distribution. We utilize the Wigner method to compute the time-dependent expectation values of symmetrized observables by integrating over the entire phase space, treating the Wigner function as the probability density at time T. If we wanted to perform this integration directly we would have to reconstruct the time-dependent Wigner function based on our time-evolved sample values, which would be numerically expansive. Therefore, this integration is performed using a Monte Carlo approach.
We sample from the initial state Wigner function and then evolve these samples according to the time

evolution equations provided earlier. Since the initial values are already correctly weighted by the initial Wigner function and then evolved, we can simply reconstruct the observables based on the time-evolved sample and calculate the stochastic average over these quantum trajectories.

$$\begin{aligned}\langle O_1...O_m\rangle_{\mathrm{sym}}(t) &= \int\prod_{i=1}^{M} d\alpha^2 O_1...O_m\mathcal{W}(\alpha_1,\alpha_1^*,...\alpha_M,\alpha_M^*)\\ &= \lim_{T\to\infty}\frac{1}{T}\sum_{l=1}^{T}\tilde{O}_1(t)...\tilde{O}_m(t),\end{aligned} \tag{91}$$

where T is the number of trajectories, O_j are either α or α^*, and $\tilde{O}_j(t)$ represents the time-evolved sample values.
We will now present an example for calculating a specific observable illustrate the utility of this method: When we were interested in the expectation value of the number operator $\langle\hat{n}_j\rangle = \langle\hat{a}_j^\dagger\hat{a}_j\rangle$, we were about to perform the following calculation:

$$\langle\hat{n}_j\rangle = \langle\hat{a}_j^\dagger\hat{a}_j\rangle = \lim_{T\to\infty}\frac{1}{T}\sum_{l=1}^{T}\tilde{\alpha}_j^*(t)\tilde{\alpha}_j(t) = \lim_{T\to\infty}\frac{1}{T}\sum_{l=1}^{T}(\tilde{x}_j^2(t)+\tilde{y}_j^2(t)). \tag{92}$$

Here $\tilde{x}_j(t)$ and $\tilde{y}_j(t)$ are the time-evolved sample values. This is where the power of the method truly shines; We have reduced the complexity of the problem to a simple time-integration according to Eq. (84) and Eq. (85) of a set of sample values and are capable of calculating the desired expectation values by a simple stochastic average. The price to pay are the trajectories. There is no universal answer for how many trajectories are required, thus this parameter depends heavily on one's experience with the system. Empirically one could do the following;
Start with a number of trajectories T_0 and calculate the observable. Double the number of trajectories $T_{i+1} = 2T_i$ and calculate the variance of the two results for the observable. Repeat this until the variance is below a reasonably chosen threshold. This may give you a feeling for the convergence of the system.

3.5.5 Numerical results

Due to the immense reduction of the complexity of the problem we can easily expand system size, compared to the method presented in Sec. 3.3, which requires the calculation of the full Fock-space, which in contrast is exponentially growing with system size. This allows us to investigate physical phenomena in larger systems. To show that the truncated Wigner approach gives meaningful approximations, we compare numerical results between the direct solution of the Bose-Hubbard model with the solution from the truncated Wigner approach for the three-well system.

The results of this comparison are shown in Fig. 12. We find that the results overall capture the dynamics of the the Bosonic-Hubbard model. Surely, we also see that the method is imperfect. We see that the results get worse for stronger on-site energy U. Especially for $g_{13}^2(U = 0.4J)$, we observe bunching, which seems to be more a relic of the approximations than a physical phenomenon, as it is not expected from the Bose-Hubbard simulation. However, $g_{13}^1 \leq 1$ and $0 \leq g_{13}^1 \leq 2$ for all times. Thus the result is meaningful in our context.

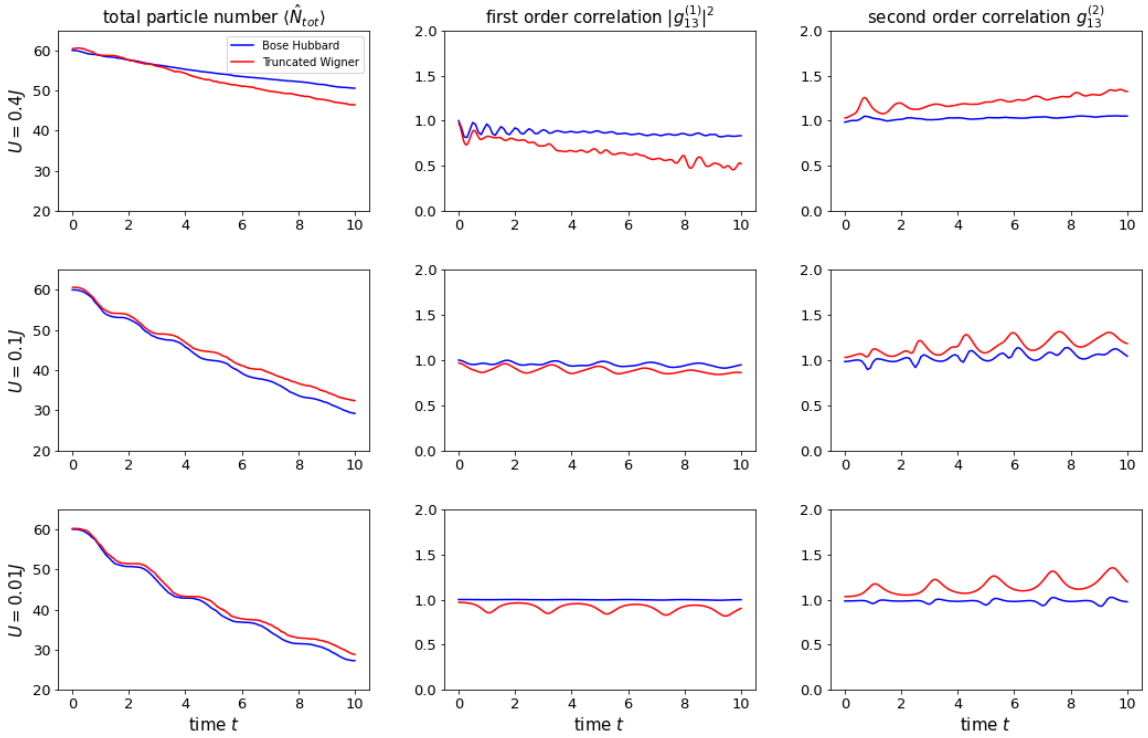

Figure 11: Shown is a comparison between the Bose-Hubbard simulations as reference and the results from the truncated Wigner approach. The blue lines represent the Bose-Hubbard simulations. The red lines represent the truncated Wigner simulations. The onsite interaction decreases from top to bottom. Shown are again three observables which are the total particle number $\langle \hat{N}_{tot} \rangle$ and the first and second order correlation $g_{13}^{(1)}$ and $g_{13}^{(2)}$. The initial state is the symmetric state $|\psi_0\rangle_+$. The system is implemented for periodic boundary conditions.

3.6 Something is rotten in the state of Denmark - comparison to literature

Even though our computations are along the line of the relevant literature [7, 14], there are some deviations in the details that have been understood and will be described in all facets within this section.

3.6.1 Operator correspondence

The computation of the Wigner function is based on the operator correspondences Eqs.(62)-(65). However, the operator correspondences used above deviates by a factor of $\frac{1}{2}$ in front the derivatives of the correspondences listed in Ref. [14]. Let us understand step by step where this deviation comes from by following the line of argument presented in [14];

Ref. [14] first rewrites the Wigner function in the well known representation in terms of local and momentum variables x and p:

$$W(x,p) = \frac{1}{\pi\hbar}\int dy \langle x+y|\rho|x-y\rangle \exp(-2iyp/\hbar). \tag{93}$$

This form may be rewritten in the momentum state basis vectors as shown in Appendix E.1:

$$\mathcal{W}(x,p) = \frac{1}{\pi\hbar}\int\int dv\ \langle p+v|\rho|p-v\rangle \exp(-2ixv/\hbar). \tag{94}$$

As described in Ref. [14], it is indeed easy to show the operator correspondences for the Wigner function $\mathcal{W}(x,p)$.

$$\left(x + \frac{i\hbar}{2}\frac{\partial}{\partial p}\right) W(x,p) \longleftrightarrow \hat{x}\rho \tag{95}$$

$$\left(x - \frac{i\hbar}{2}\frac{\partial}{\partial p}\right) W(x,p) \longleftrightarrow \rho\hat{x} \tag{96}$$

$$\left(p - \frac{i\hbar}{2}\frac{\partial}{\partial x}\right) W(x,p) \longleftrightarrow \hat{p}\rho \tag{97}$$

$$\left(p + \frac{i\hbar}{2}\frac{\partial}{\partial x}\right) W(x,p) \longleftrightarrow \rho\hat{p} \tag{98}$$

A detailed derivation showing that these operator correspondences are in fact true is found in Appendix E.2. Ref. [14] then presents a relation between x, p and α;

$$\alpha = \frac{1}{\sqrt{2}}(x + \frac{i}{\hbar}p). \tag{99}$$

From this relation it is indeed possible to compute the operator correspondences for $\mathcal{W}(\alpha,\alpha^*)$. For example:

$$\begin{aligned}
\hat{a}\rho = \frac{1}{\sqrt{2}}(\hat{x} + i\hat{p}) &\longleftrightarrow \frac{1}{\sqrt{2}}\left(\left(x + \frac{i\hbar}{2}\frac{\partial}{\partial p}\right) + \frac{i}{\hbar}\left(p - \frac{i\hbar}{2}\frac{\partial}{\partial x}\right)\right)\mathcal{W}(\alpha,\alpha^*) \\
&= \frac{1}{\sqrt{2}}(x + \frac{i}{\hbar}p) + \frac{1}{\sqrt{2}}\left(\frac{1}{2}\frac{\partial}{\partial x} + \frac{i\hbar}{2}\frac{\partial}{\partial p}\right)\mathcal{W}(\alpha,\alpha^*) \\
&= \left(\alpha + \frac{\partial}{\partial \alpha^*}\right)\mathcal{W}(\alpha,\alpha^*).
\end{aligned} \tag{100}$$

However Ref. [14] writes

$$\hat{a}\rho = \left(\alpha + \frac{1}{2}\frac{\partial}{\partial \alpha^*}\right)\mathcal{W}(\alpha,\alpha^*). \tag{101}$$

This is wrong, scince the rules of the complex Wirtinger differentiation [133] used in [14] state that for a variable $z = x + iy$ the derivative is of the form

$$\frac{\partial}{\partial z} = \frac{1}{2}\left(\frac{\partial}{\partial x} - i\frac{\partial}{\partial y}\right). \tag{102}$$

Thus Ref. [14] forgets that the factor $\frac{1}{2}$ is absorbed in the complex derivative. Thus the operator correspondences for $\mathcal{W}(\alpha,\alpha^*)$ we have shown above are correct, since they agree with Ref. [14], when neglecting the wrong factor $\frac{1}{2}$. When neglecting this wrong pre-factor, the results also agree with similar relations in chapter 2.8 of [15].

3.6.2 Wigner function

All this might seem somewhat pedantic, however, these operator correspondences are the fundament of the truncated Wigner approach. Our reference paper [7] has used the operator correspondences as they are written in Ref. [14]. Why are the results in [7] still good, even though wrong operator correspondences were used?

To answer this question it is helpful to think about how the factor $\frac{1}{2}$ would change the result. The factor appears infront of the derivative, so the result has to be multiplied by a factor of $\frac{1}{2^{\mathcal{O}}}$, where $\mathcal{O}$ notes the order of the derivatives in the final equation. Modifying Eq. (76) by this prefactor, we arrive at a result for the Wigner function which should only be considered for comparison with the true result from Eq. (76).

The only purpose for this calculation is the attempt to understand weather our result agrees with the literature [7], when making the assumptions made there. Under the assumption of wrong operator correspondences from [14] we arrive at:

$$\begin{aligned}\frac{d}{dt}\hat{\rho}(t) \leftrightarrow \partial_t \mathcal{W} = &\sum_j \left[\frac{\partial}{\partial x_j}\left(J(y_{j+1}+y_{j-1}) - U(x_j^2 y_j + y_j^3) + \frac{\gamma_j}{4}x_j\right)\right]\mathcal{W} \\ &+ \sum_j \left[\frac{\partial}{\partial y_j}\left(-J(x_{j+1}+x_{j-1}) + U(x_j y_j^2 + x_j^3) + \frac{\gamma_j}{4}y_j\right)\right]\mathcal{W} \\ &+ \frac{1}{2}\sum_j \frac{\gamma_j}{4}\left(\frac{\partial^2}{\partial x_j^2} + \frac{\partial^2}{\partial y_j^2}\right)\mathcal{W}.\end{aligned} \tag{103}$$

Here, we only considered the truncated solution, as it is the one calculated in [7]. Directly quoting from Ref. [7] we have:

$$\begin{aligned}\frac{d}{dt}\hat{\rho}(t) \leftrightarrow \partial_t \mathcal{W} = &\sum_j \left[\frac{\partial}{\partial x_j}\left(J(y_{j+1}+y_{j-1}) - U(x_j^2 y_j + y_j^3 - y_j) + \frac{\gamma_j}{2}x_j\right)\right]\mathcal{W} \\ &+ \sum_j \left[\frac{\partial}{\partial y_j}\left(-J(x_{j+1}+x_{j-1}) + U(x_j y_j^2 + x_j^3 - x_j) + \frac{\gamma_j}{2}y_j\right)\right]\mathcal{W} \\ &+ \frac{1}{2}\sum_j \frac{\gamma_j}{4}\left(\frac{\partial^2}{\partial x_j^2} + \frac{\partial^2}{\partial y_j^2}\right)\mathcal{W}.\end{aligned} \tag{104}$$

When looking closely, the attentive reader may notice even further deviations in the details between Eq. 103 and Eq. 104. To understand what is going on we will start discussing these deviations of these two equations to each other. Since [7] truncated the third order, it is thus reasonable only to compare up to the truncated solution.

3.6.3 Energy shift in the Wigner function

In contrast to our analysis, the formulation presented by [7] introduces an additional term not discussed so far that is linear in x and y in the first order term. We will show that this additional term has no physical meaning, as it corresponds to a global energy shift of the system of U. The calculations presented in Ref. [7] use the following Hamiltonian:

$$\mathcal{H} \equiv \mathcal{H}_{\text{jump}} + \mathcal{H}_{\text{int}} = -J\sum_j (\hat{a}_{j+1}^\dagger \hat{a_j} + \hat{a}_j^\dagger \hat{a}_{j+1}) + \frac{U}{2}\sum_j \hat{a}_j^\dagger \hat{a}_j^\dagger \hat{a}_j \hat{a}_j, \tag{105}$$

which is exactly the same Hamiltonian we have used above. Therefore, it appears that the results from [7] do not align consistently with the Hamiltonian defined in this work.
However, adding a global energy shift to the Hamiltonian, commonly associated with the chemical potential, does not alter the physical implications:

$$\mathcal{H} \equiv \mathcal{H}_{\text{jump}} + \mathcal{H}_{\text{int}} + \mathcal{H}_{\text{chem}} = -J\sum_j (\hat{a}_{j+1}^\dagger \hat{a_j} + \hat{a}_j^\dagger \hat{a}_{j+1}) + \frac{U}{2}\sum_j \hat{a}_j^\dagger \hat{a}_j^\dagger \hat{a}_j \hat{a}_j - \mu\sum_j n_j \tag{106}$$

Similarly to above we start to calculate the time evolution of this additional term in the context of the Wigner function, by employing the operator correspondences. Note that we now explicitly use the wrong

operator correspondences from [14], since these are the ones which were used in [7] which's results we aim to understand;

$$
\begin{aligned}
[\mathcal{H}_{\text{chem}}, \hat{\rho}(t)] &= -\mu \sum_j (\hat{a}_j^\dagger \hat{a}_j \rho - \rho \hat{a}_j^\dagger \hat{a}_j) \\
&\leftrightarrow -\mu \sum_j \left(\left(\alpha_j^* - \frac{1}{2} \frac{\partial}{\partial \alpha_j} \right) \left(\alpha_j + \frac{1}{2} \frac{\partial}{\partial \alpha_j^*} \right) - \left(\alpha_j^* + \frac{1}{2} \frac{\partial}{\partial \alpha_j} \right) \left(\alpha_j - \frac{1}{2} \frac{\partial}{\partial \alpha_j^*} \right) \right) \mathcal{W} \\
&= \mu \sum_j \left(x_j \frac{\partial}{\partial y_j} - y_j \frac{\partial}{\partial x_j} \right) \mathcal{W}.
\end{aligned}
\tag{107}
$$

Where the last step is explicitely calculated in Appendix E.3.
If we choose $U = -\mu$ we recover for the truncated Wigner formula;

$$
\begin{aligned}
\partial_t \mathcal{W} = &\sum_j \left[\frac{\partial}{\partial x_j} \left(J(y_{j+1} + y_{j-1}) + U(y_j - x_j^2 y_j - y_j^3) + \frac{\gamma_j}{2} x_j \right) \right] \mathcal{W} \\
&+ \sum_j \left[\frac{\partial}{\partial y_j} \left(-J(x_{j+1} + x_{j-1}) - U(x_j - x_j y_j^2 - x_j^3) + \frac{\gamma_j}{2} y_j \right) \right] \mathcal{W} \\
&+ \frac{1}{2} \sum_j \frac{\gamma_j}{4} \left(\frac{\partial^2}{\partial x_j^2} + \frac{\partial^2}{\partial y_j^2} \right) \mathcal{W}.
\end{aligned}
\tag{108}
$$

Again, Eq. (108) aims to understand [7] and is technically wrong. Setting $U = -\mu$ allows us to recover the terms present in [7] and absent in our calculations. This showcases that these terms not present in our result correspond to an implicitly added global energy shift. Our meticulous review indicates that [7] incorporated an additional global shift in energy, diverging from the Hamiltonian employed in the work. Where this oversight originates from in either of the calculations remains ambiguous. Furthermore, an apparent discrepancy in an intermediate step in the sign has been found, as highlighted in red along the calculations in Appendix D.2. This seems to stem from a typographical error, given that our findings for the corresponding terms align.
In conclusion, the global energy shift, while not present in our result and most likely mathematically not present for the Hamiltonian introduced, holds no physical significance in our investigation. Hence, it will be disregarded in further analyses, reinforcing the consistency and integrity of our approach relative to the established Hamiltonian framework.

3.6.4 Decay term

Comparing Eq. (103) with Eq. (104) one may note that in the first order term, the one features $\frac{\gamma_j}{4}$ and the other [7] features $\frac{\gamma_j}{2}$. As demonstrated in detail in Appendix E.4 this is indeed an error occurring in [7], when employing the operator correspondences used in this work. Under the assumption of the wrong operator correspondences, we should not recover this result. However, this error is essential to achieve good results, when implementing the wrong operator correspondences from [14].

Compared to our result presented in Eq. (76), we realize that the first-order term aligns with the results from Ref. [7], presented in Eq. (104), besides a factor 2 upfront of J and U. This factor is however irrelevant since the strength of the system parameters is only meaningful relative to each other. So the system variables J and U are effectively rescaled by a factor of 2, the fraction U/J determining the systems dynamics is the same. For the decay term this is a different story since it essentially corresponds to an event rate. The error,

meaning $\frac{\gamma_j}{2}$ instead of $\frac{\gamma_j}{4}$, occurring in the result of [7] thus makes the calculations accurate to the first order, hiding the impact of the wrong operator correspondences from [14].

For the second-order term, this looks a little different. Here our result differs by a factor of 4 which is explained by the wrong operator correspondences. This means that accordingly, the second-order term is too small by a factor of $\frac{1}{4}$ compared to the true result due to the wrong factor $\frac{1}{2}$ in the operator correspondence in [14]. In the final equations of motion Eq. (84) and Eq. (85) this means a deviating factor of $\frac{1}{2}$ compared to our results. (Second-order factors enter the equation of motion by the square root, as described in Sec. 3.5.2.) Thus we implement Eq. 84 and Eq. 85 which are repeated for direct comparison:

$$\frac{dx_j}{dt} = -2J(y_{j+1} + y_{j-1}) + 2U(x_j^2 y_j + y_j^3) - \frac{\gamma_j}{2}x_j + \sqrt{\gamma_j}\zeta_j \tag{109}$$

$$\frac{dy_j}{dt} = 2J(x_{j+1} + x_{j-1}) - 2U(x_j y_j^2 + x_j^3) - \frac{\gamma_j}{2}y_j + \sqrt{\gamma_j}\eta_j. \tag{110}$$

In contrast, Ref. [7] implemented the following equations:

$$\frac{dx_j}{dt} = -J(y_{j+1} + y_{j-1}) - U(y_j - x_j^2 y_j - y_j^3) - \frac{\gamma_j}{2}x_j + \frac{\sqrt{\gamma_j}}{2}\zeta_j \tag{111}$$

$$\frac{dy_j}{dt} = J(x_{j+1} + x_{j-1}) + U(x_j - x_j y_j^2 - x_j^3) - \frac{\gamma_j}{2}y_j + \frac{\sqrt{\gamma_j}}{2}\eta_j. \tag{112}$$

As already said, the deviating factor 2 upfront J and U is irrelevant due to the relative scaling of these variables. The linear term in x_j and y_j is also irrelevant, as it corresponds to a global shift in energy. The first term involving γ_j is accidentally correct, even though this is a computational error in [7] when following the calculations presented there and the last term deviates by a factor of $\frac{1}{2}$, which makes indeed a difference. However, from here it becomes obvious why [7] achieved good results, as the mean-field part of the dynamical equations is implemented correctly. Our solution implies that [7] used effectively only half of the noise that should have been used. We would expect that the correct implementation reveals overall similar results, with weaker fluctuations as these would be damped by the "stronger" influence of the noise.

For the higher order terms, the impact of the wrong operator correspondences from [14] become more dramatic. However, higher order terms were not considered in the original paper [7] anyways. In summary both [14] and [7] made errors along the computations, compensating each other in the dominant terms.

3.6.5 Numerical comparison

In Fig. 12 we compare our solution with the dynamical equations Eq. (84) and Eq. (85) with the solutions obtained with the equations presented in [7] and quoted in Eq. (111) and Eq. (112). We take the simulations of the Bose-Hubbard model as a reference, to see which equations are closer to the true result. For the total particle number $\langle \hat{N}_{tot} \rangle$, we see for the higher onsite energy $U = 0.4J$, the approach underestimates the correct result, while they tend to overestimate for smaller U/J. Thus there must be a U/J where they align almost perfectly, which is the case for the equations from [7] at $U = 0.1J$. This seems only little surprising, as this value for U/J was purposefully chosen in this paper, to show that the equations from [7] recover good results. For the second order correlation $g_{13}^{(2)}$ we see that our effectively more dominant noise leads to less extreme oscillations, which was expected. This also means that the unexpected bunching observed in the Wigner simulations is less extreme. Overall, our corrected results are either better or only slightly worse than the ones calculated with the equations from [7]. Thus, it is little surprising that the errors made in this calculation were never noticed in the original paper. Altogether, understanding our deviations from the literature raised our confidence in the correctness of our solution.

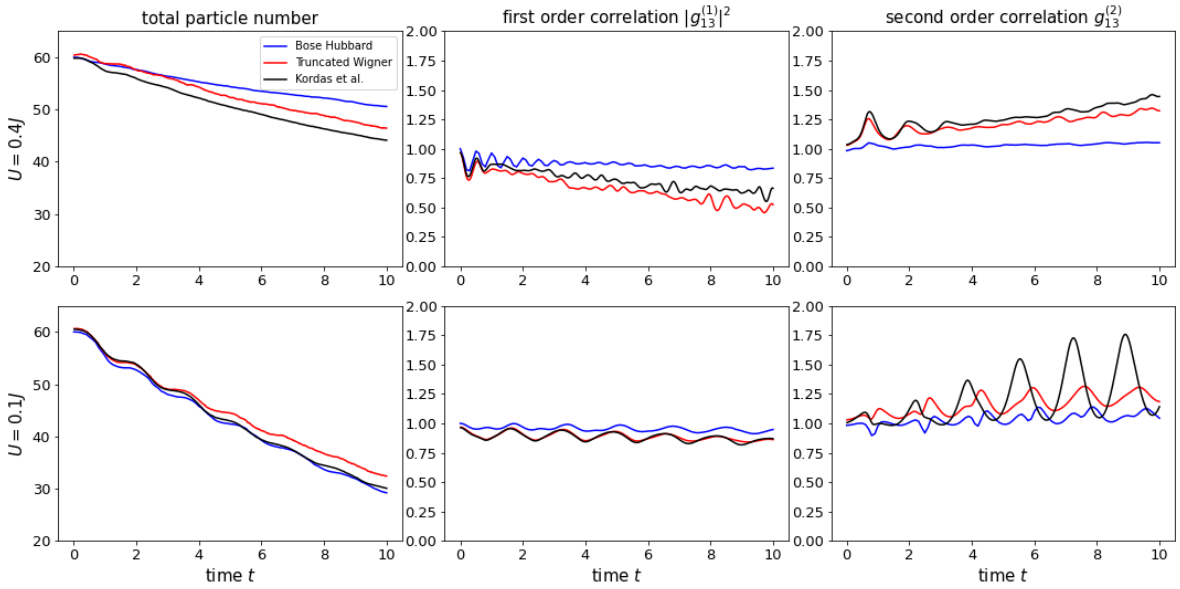

Figure 12: Shown is a comparison between the Bose-Hubbard simulations (blue lines) as a reference, our truncated Wigner simulations (red lines) and the results calculated with the equations from [7] (black lines). The top row corresponds to $U = 0.4J$ and the bottom row corresponds to $U = 0.1J$. Shown are again three observables which are the total particle number $\langle \hat{N}_{tot} \rangle$ and the first and second order correlation $g_{13}^{(1)}$ and $g_{13}^{(2)}$. The initial state is the symmetric state $|\psi_0\rangle_+$. The system is implemented for periodic boundary conditions.

3.7 Beyond truncated Wigner

3.7.1 Higher derrivatives

In our model, the noise terms are interpreted as manifestations of the underlying operator commutation relations, introducing the influence of quantum mechanical interactions within the system. This interpretation reveals a critical insight: eliminating the decay term, γ_j, nullifies the effects attributed to the commutation relations. Such a scenario poses a physical inconsistency, underscoring a potential misalignment with our approximation. This prompts a reevaluation of our approach, particularly the exclusion of higher-order terms in the Truncated Wigner approximation. These higher-order Terms will now be considered in the formalism.

Our Truncated Wigner formulation encompasses derivatives up to the second order, representing drift and diffusion components. This simplification, achieved by disregarding terms beyond the second order, allows for an analogy with the Fokker-Planck equation. However, the presence of a third-order derivative term in the full equation introduces complexities not accounted for in the conventional Fokker-Planck framework. The interpretation of this third-order term remains elusive, suggesting a gap in our interpretation of the underlying dynamics. For an analogical understanding, we consider the Korteweg-de Vries (KdV) equation, since it incorporates a third-order derivative term interpreted as nonlinear dispersion effects. This term, emblematic of the KdV equation, delineates the variation in diffusion strength relative to wavelength, thereby encapsulating dispersive phenomena. In an analogy of wave dynamics which is the field of the KdV equation, dispersion arises because the speed of the waves also depends on their wavelength. This term ensures that the equation accounts for the spreading of the wave packet over time, which is a critical aspect of wave behavior in mediums that exhibit dispersive characteristics. In that sense, it is not so unsimilar to the diffusion present in the Fokker-Planck equation. In our case, the third-order dispersion term is of the following form:

$$U \sum_j \left[y_j \left(\frac{\partial^2}{\partial x_j^3} + 3 \frac{\partial}{\partial x_j} \frac{\partial^2}{\partial y_j^2} \right) - x_j \left(\frac{\partial^3}{\partial y_j^3} + 3 \frac{\partial^2}{\partial x_j^2} \frac{\partial}{\partial y_j} \right) \right] \mathcal{W}. \tag{113}$$

We see that dispersive effects are modulated by the amplitude's real and imaginary components within each well. This observation underscores the significance of including higher-order dynamics in our analysis, as they may offer critical insights into the dispersion mechanisms in the system.

Initial attempts aimed to find an approximation that reduces the third-order structure to a second-order equation and to identify the result with a Fokker-Planck equation. The goal was to map the resulting equation onto the Langevin equation, as done above in the truncated Wigner approach. However, these attempts were unsuccessful and are discussed in Appendix F as negative results. The primary objective was to motivate a different stochastic process in the SDE that reflects the higher-order nature of the equations of motion for the PDE, similar to the approach in [134]. Recently, a new paper [135] appeared, that introduced a promising approach to include terms in the stochastic process that account for an underlying third-order PDE. Due to time constraints, we were unable to achieve conclusive results. However, we are optimistic about future progress. Therefore, we will discuss the implications of this paper for our problem.

3.7.2 Multiplicative noise - A new approach

The paper mentioned above [135] opens with the following SDE:

$$\frac{dx}{dt} = -\omega x + f(t) - \epsilon x \zeta(t), \tag{114}$$

which is essentially the Langevin equation with an additional random term. The new ζ-random term is called the multiplicative noise, as it is multiplied with the position. $\zeta(t)$ is a Gaussian stochastic process and $f(t)$ again resembles a white noise contribution. In Ref. [135], this SDE is mapped onto the corresponding PDE, where the stochastic current is given by:

$$J(x) = \left[(\omega\tau + \delta^2)x/\tau + (D_\zeta(x) + D_f)\partial_x + D_f D_\zeta(x)\theta\partial_x^2\right] P(x,t) \tag{115}$$

and the probability $P(x,t)$ follows the conservation law

$$\partial_t P(x,t) = \partial_x J(x). \tag{116}$$

The variable θ is given by:

$$\theta = \frac{1}{\omega\tau}(\tau - \hat{\phi}(2\omega)), \tag{117}$$

with $\hat{\phi}$ being the Laplace transform of the autocorrelation function $\phi(t) = \langle\zeta(t)\zeta(0)\rangle/\langle\zeta^2\rangle$:

$$\hat{\phi} = \int_0^\infty du \phi(u) \exp(-su). \tag{118}$$

Also, $D_\zeta(x)$ and D_f are the diffusion matrices for the underlying random process. $\delta = \epsilon\tau$ is the effective perturbation strength and $\tau = \int_0^\infty \phi(u)du$. In other words, the mapping between the two equations depends on numerous details. Nonetheless, the connection between Eq. (115) and Eq. (114) is particularly significant. It demonstrates that the presence of both additive and multiplicative noise introduces a third-order term in the time evolution of the probability density. The presence of either multiplicative or additive noise alone results in a second-order partial differential equation (PDE). It is important to note that a stochastic process is either described by a PDE of second order or infinite order [93]. Consequently, when utilizing Eq. (114), the process can only be accurately described by a PDE of infinite order. However, Ref. [135] states, that the process can be sufficiently approximated by a third-order PDE.
Returning to our problem, we aim to solve the system in Eq. (76) within the framework of the trajectory method, incorporating the third-order term. We intend to use a modified version of Eq. (84) and Eq. (85). The addition of a multiplicative noise term effectively introduces infinite orders to the PDE describing the dynamical evolution of the Wigner function (Eq. (76)). However, as discussed in [135], the multiplicative noise predominantly introduces a third-order term. Thus, while this approach is inherently an approximation, it aims to capture the influence of quantum fluctuations more precisely than the truncated Wigner method. Effectively this approach comes with numerous challenges; From Eq. (114) we see that when introducing an additional multiplicative random process into our equations Eq. (84) and Eq. (85), we would effectively also change the terms of lower order in Eq. (76). Of course, this is not our intention. The issue is, that

Ref. [135] starts with a SDE and wants to find the PDE, describing the process. In our problem, however, we know the PDE (which is Eq. (76)) and want to find a stochastic process that resembles the dynamics of the system. Thus, we effectively have to do some backwards-engineering, which is somewhat complicated, due to the dependencies of the lower order terms on the autocorrelation function of the multiplicative stochastic process.
An alternative attempt more closely along the line of [135] would be to add a multiplicative stochastic process to Eq. (84) and Eq. (85), then understand how this would change Eq. (76). Then we would need to control the influence of the additional stochastic process on the lower orders.

Also, there are additional complications. Ref. [135] describes a 1D problem. However, we are in a 2D scenario. Additionally, we have also mixed derivatives in x and y, which make the problem significantly more complicated. Also, an additional complication is that the third-order term in Eq. (76) includes third-order derivatives but also a dependency on the position x and y, which is not present in Eq. (115). Thus, it could be possible that the process on the SDE level becomes inherently unstable. It could be the case, that this is not unphysical, as additional influence from quantum fluctuations additionally perturbs the system.
Either way, we would have to be way more attentive in the integration of the stochastic process. We stated above that the equations are sufficiently simple that they may be integrated by simple methods. The addition of another noise term requires a better numerical treatment, which accounts for the stochastic process. As an example for Gaussian noise suitable for the multiplicative "third-order process", [135] explicitly calculates the Ornstein-Uhlenbeck process, which would have to be integrated as an Ito-process. It is important to choose a more accurate integration scheme, as the process is now of higher order.

3.7.3 A practical attempt

Given the constraints of time, we are unable to present definitive results but rather offer a conceptual approach for incorporating a multiplicative stochastic term. We employ the Ornstein-Uhlenbeck process as a form of Gaussian noise, defined as:

$$dO = O\sigma dt + \sqrt{2\sigma}dW, \tag{119}$$

where dW represents stochastic white noise. Typically, the Ornstein-Uhlenbeck process involves several free parameters, but we have effectively reduced the complexity to a single free parameter, $\sigma = 1\times10^{-6}$. This value of σ was empirically chosen to ensure the process generates values of comparable amplitude to the white noise in Eqs. (84) and (85). Initial attempts revealed that a straightforward addition of a multiplicative process to our SDEs caused highly divergent results. The most stable results were achieved by preserving the symmetry $\mathcal{F}(x,y) = -\mathcal{F}(y,x)$ of the third order term in Eq. (76). Other less symmetric multiplicative processes led to unphysical phenomena, such as an increase in particle numbers. We implemented the following SDEs:

$$\frac{dx_j}{dt} = -2J(y_{j+1} + y_{j-1}) + 2U(x_j^2 y_j + y_j^3) - \frac{\gamma_j}{2}x_j + \sqrt{\gamma_j}\zeta_j + (x_j dO_j^x - y_j dO_j^y)\sqrt{U}\epsilon, \tag{120}$$

$$\frac{dy_j}{dt} = 2J(x_{j+1} + x_{j-1}) - 2U(x_j y_j^2 + x_j^3) - \frac{\gamma_j}{2}y_j + \sqrt{\gamma_j}\eta_j + (y_j dO_j^y - x_j dO_j^x)\sqrt{U}\epsilon, \tag{121}$$

where dO_j^x and dO_j^y are two identical Ornstein-Uhlenbeck processes for each well. The parameter ϵ is an empirically chosen variable to ensure that the correction term remains sufficiently small so that numerical stability is maintained. Here we choose $\epsilon = 1 \times 10^{-5}$. Essentially, we introduced a multiplicative stochastic process to our equations, modeling a third-order term while empirically ensuring non-diverging numerical results. Indeed, we observe that the changes introduced in Fig. 13 are minimal, attributable to our choices of ϵ and σ. It is important to note, that the numerical stability is quite sensitive to these parameters. For $U = 0.4J$, one might even argue that the addition of multiplicative noise resulted in some minor improvements. Conversely, for weaker U/J, it seems that any observed benefits may be somewhat lucky. These findings emphasize the necessity of incorporating multiplicative noise to model a third-order term in our equations with attention to the details. This neglected aspect will be the subject of our ongoing research efforts.

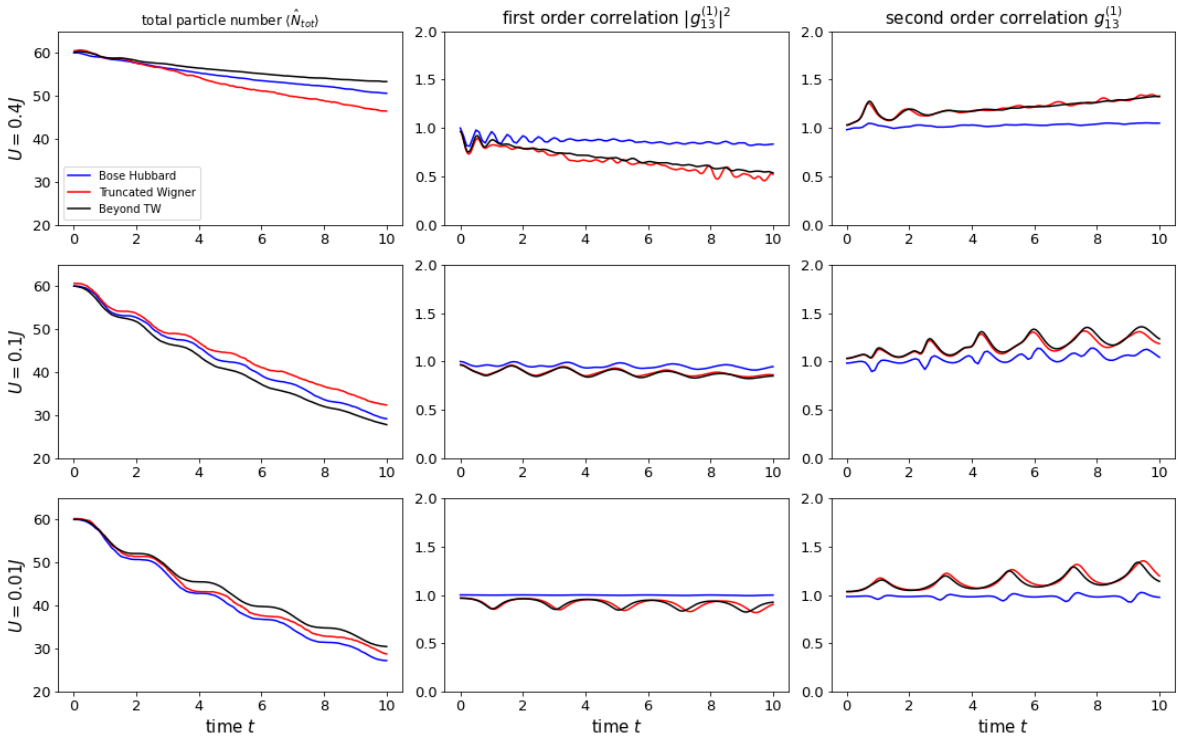

Figure 13: Shown is a comparison between the Bose-Hubbard simulations (blue lines) as a reference, our truncated Wigner simulations (red lines) and the results calculated with an additional multiplicative stochastic process modeling a third order term (black lines). The onsite energy decreases from top to bottom. Shown are again three observables which are the total particle number $\langle \hat{N}_{tot} \rangle$ and the first and second order correlation $g_{13}^{(1)}$ and $g_{13}^{(2)}$. The initial state is the symmetric state $|\psi_0\rangle_+$. The system is implemented for periodic boundary conditions.

4 Conclusion

4.1 Summary

In this thesis we investigated two open quantum systems. Both systems are experimentally realized as a Bose-Einstein condensate (BEC) in an optical lattice [17–20], of which we considered in the first chapter BEC in a time dependent potential with neglectable interaction and in the second chapter a BEC that is explicitly subject to atom-atom interactions. The dynamics turn explicitly time-dependent due to interactions in the system. In both cases, the dynamics are described with the quantum optical master equation and the system is solved utilizing the quantum trajectory method.

In the first chapter, the system of interest was the atom optics quantum kicked rotor (AOKR), where we discussed the dynamics of quantum walks (QWs). In contrast to the second chapter where we discussed the many body Bose-Hubbard system, we assumed that the interaction between the atoms in the BEC is neglectable. The system became an open quantum system with the introduction of spontaneous emissions (SE).
In our research, we unveiled the intricate dynamics between symmetry and the significant impact of the coin's selection on system behavior. Introducing SE has proven essential for breaking initial symmetry in a QW, thus enabling the development of a QW ratchet. While SE typically introduces detrimental effects, we have shown that under specific conditions, it can play a beneficial role [3, 66, 136] and produce interesting effects. Our study of the symmetry observable S over time reveals a clear transition from quantum to classical behavior as the strength of SE increases. This transition is evidenced by fitting a power-law to $S(t)$, highlighting

a change from ballistic to sub-ballistic expansion, corresponding to the quantum-to-classical transition in the walk. The asymmetry observed arises from interference effects, stemming from particular choices of the coin matrix and non-resonant free evolution due to SE-induced shifts in quasimomentum. Our results also show the robustness of SE-induced asymmetries, even when considering finite initial quasimomentum, which is expected in experimental setups due to finite temperatures. This robustness underscores the potential for experimental realization of a SE-induced QW ratchet. Our study offers a comprehensive understanding of the dynamics and symmetries of AOKR QWs and the influence of SE. By revealing the unexpected utility of SE in creating an AOKR ratchet and demonstrating the system's resilience against variations in quasimomentum, our work provides valuable insights for future experimental research or for designing Parrondo-like games along the line of [16, 19, 20, 55]. We published these findings within the context of this thesis [1].

In the second chapter, we explored the many-body Bose-Hubbard system. We presented a standard method for solving the system using the quantum trajectory method, providing results that serve as a reference for further advancements. Direct computation of the system is numerically intensive, with computational effort growing exponentially with system size, which necessitates the use of approximative methods such as the truncated Wigner method. In this context, we gained a detailed understanding of the truncated Wigner method, often casually written down in the literature. We explicitly derived the operator correspondences that allow us to translate the equations of motion from a fully quantum mechanical framework in Fock space to the quasi-probabilistic phase-space picture of the Wigner function. During this process, we identified and understood an error in the literature [7, 14]. Using these operator correspondences, we translated the Bose-Hubbard system into the framework of the Wigner function. By truncating the resulting third-order term, we were able to map the system onto the Fokker-Planck equation. Employing the Feynman-Kac relation, we translated the probabilistic ensemble picture into a stochastic single-particle picture described by a set of Langevin equations. These equations essentially contained the mean-field solution plus an additional noise term, which we interpreted as quantum fluctuations. This approach allows the numerically expensive Bose-Hubbard model to be approximately solved by calculating the time evolution of these equations. The observables are now calculated as a simple statistical average over trajectories. Our calculations were along the line of [7], but we provided all the details omitted in that reference, leading to a nuanced understanding of the method. In doing so, we uncovered some errors in the literature, which essentially stemmed from incorrect operator correspondences in [14]. Comparing the results, we found that equations from [7] did not cause significant deviations from our corrected results, explaining why errors were previously unnoticed. The main goal was to advance the truncated Wigner method by incorporating higher-order terms. We found a promising approach in [135], which may enable the inclusion of higher-order derivatives in the system's time evolution as modified noise. Successfully applying this approach to our system might shine some light on the more nuanced details of quantum fluctuations within the truncated Wigner framework, providing a better approximation of the true solution of the many-body Hamiltonian. This opens a promising route for developing a more refined method when solving the system in the context of the Wigner picture.

4.2 Outlook

In our study of the atom optics kicked rotor (AOKR) with additional spontaneous emissions (SE), we observed a notable phenomenon: the introduction of SE induces asymmetries in an initially symmetric quantum walk (QW). Over time, increasing decoherence causes the system to undergo a quantum-to-classical transition. Remarkably, some sufficiently small non-zero initial quasimomentum, analogous to a Bose-Einstein condensate (BEC) at finite temperature, delays this transition when SE rates are sufficiently low. This finding is counterintuitive, as one might expect additional off-resonances to enhance decoherence and thereby accelerating the transition. However, our results indicate that this intuition is only partially correct under certain conditions. Interestingly, a similar effect was noted in the outlook of our previous work [4], however in a different context. This suggests the possibility of an underlying mechanism where the introduction of small initial noise acts stabilizing on the system, potentially preserving information stored in quantum mechanical resonances more effectively.

In the second chapter, we examined the many-body Bose-Hubbard system. Due to the numerically expensive nature of directly solving this system, approximative methods are of high interest. We focused on the truncated Wigner approach, which truncates higher-order terms in the dynamical equations beyond the

second order. This truncation allows mapping the system onto a Fokker-Planck equation, which can subsequently be mapped on a set of stochastic Langevin equations. The latter facilitates solving the system as a stochastic average over trajectories. These Langevin equations incorporate the mean-field solution with an additional noise term, representing quantum fluctuations. However, truncating higher-order terms omits the finer details of quantum fluctuations. A recent paper [135] introduced an intriguing method where an additional "multiplicative" stochastic process in the stochastic differential equation (SDE) models a third-order term in the partial differential equation (PDE) describing the process. While the dynamical equations for the Wigner function could be directly solved, we aim to maintain the numerical simplicity of the approach in our advancements of the method. Given that our dynamical equations for the Wigner function are of third order, the method described in [135] is of significant interest. Here, an additional stochastic process in the SDE models a PDE of third order. Incorporating this additional stochastic term into the SDEs describing our system also affects the lower orders of the corresponding PDE, necessitating care and attention when applying this method. Moreover, Ref. [135] addresses a 1D problem, whereas we are dealing with a 2D problem, adding further complexity to this mapping. Despite these challenges, we are confident that this method offers a promising direction for future research in developing a more refined version of the Wigner method.
The Wigner picture describes the system as a time-dependent semiclassical probability density. When the time evolution is not done accurately, we expect divergent behavior at some time as the methodology is sensible to the approximations, as seen in Appendix F. The advantage of the solution obtained from the Wigner method is that it contains the mean-field solution plus additional terms. These additional terms capture the dynamics of the system beyond the mean-field approximations. However, this implies that the system should diverge when the approximations of the beyond mean-field solution do not hold, meaning for large times and large U/J which complicates analyzing the quality of any additional terms.

Appendix

A Chapter 1 - Additional Details

In the text it has been stated that the convergence of the symmetric regions with $S = 0$ onto the predictions from Sec. 2.2.2 increases for increasing timesteps. This can be seen for example from Fig. 14 (a), where the symmetry map is shown for $T = 20$ steps, instead of $T = 15$, revealing better convergence of the points with $S = 0$ on the white lines, indicating the predicted symmetry regions. The points of high asymmetry are also clearly visible at the expected spots.

Furthermore, the stripe pattern shifts towards larger γ when SE rates increase, as a consequence of the projection operations. This could not be seen clearly from Fig. 6, due to the noise in the image. To prove this statement, we artificially switch off the shift in quasimomentum during the free evolution between subsequent pulses to reduce decoherence. Indeed we can see from Fig. 14 that the stripe pattern performs a slight shift, situating the $\hat{G}_H$-coin (blue dot) in a more asymmetric region.

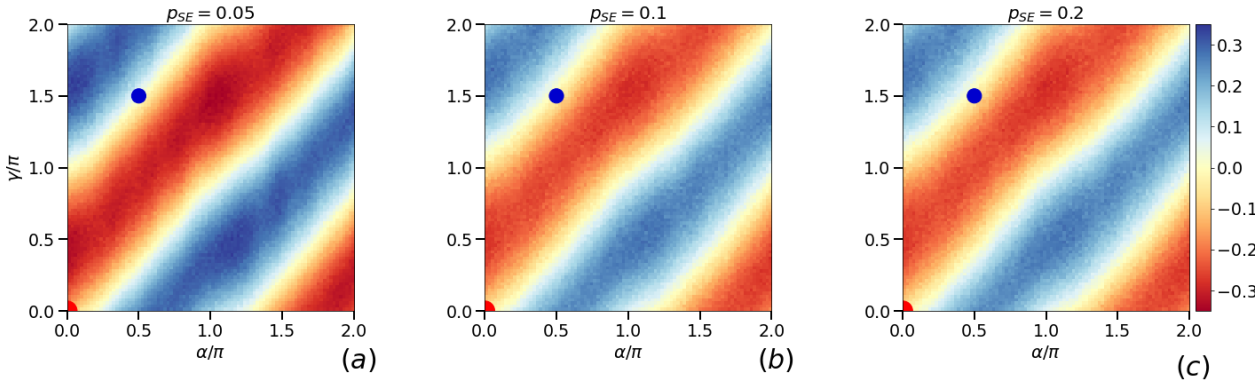

Figure 14: Similarly to Fig. 6, the figure presents a scan of the symmetry indicator $S(\gamma, \alpha)$ for the QW, however evaluated after 20 steps. Also, the shift in quasimomentum is artificially set to zero in the free evolution between subsequent pulses. The walk is initiated with the $\hat{Y}$-coin and then evolved under $\hat{M}(\chi = \frac{\pi}{4}, \gamma, \alpha)$ during the walk. The SE rates increase from left to right. The red dot at $(\gamma = 0, \alpha = 0)$ indicates the more symmetric walk using the $\hat{W}$-coin, while the blue dot at $(\gamma = 1.5\pi, \alpha = 0.5\pi)$ indicates the asymmetric walk using the $\hat{G}_H$-coin (refer to Fig. 4). At $T = 20$ the lines of $S = 0$ match better with the predictions from Sec. 2.2.2 and we also observe a shifting of the stripe pattern towards higher γ for increasing SE.

Broadening the initial state in Eq. (17), the QW experiences a more coherent movement (Sec. 2.1.4). For the $\hat{G}_H$-coin, the central part of the momentum distribution vanishes and the probability is prevalent in the ballistic peaks, thus contributing to the asymmetry effect. This is discussed for the asymmetry in Sec. 2.4.1. We explicitly show the momentum distributions for $p_{\mathrm{SE}} = 5\%$ and $p_{\mathrm{SE}} = 10\%$ to undermine this statement.

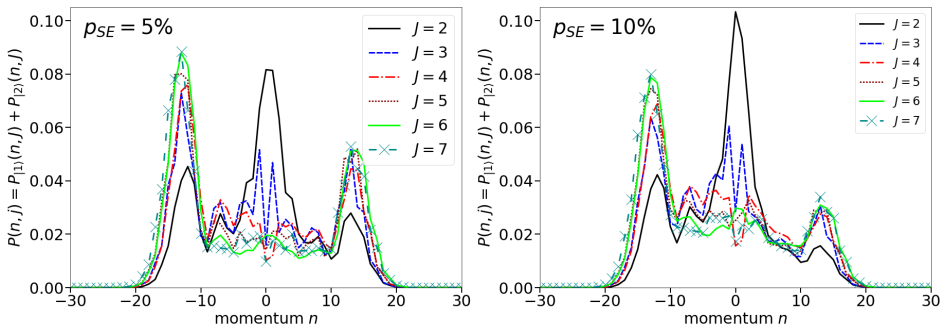

Figure 15: The figure shows the dependency of the momentum distribution of the walk evolved under $\hat{G}_H$ on the width J of the initial state for two different SE rates. The figure shows that the central part of the distribution diminishes for increasing J, thus increasing probability in the peaks. This way S increases with larger J, as discussed in Fig. 7 (a).

B Chapter 1 - Motivation Wigner function

The Wigner function is a quasiclassical phase space function.
To underscore this statement we present an argument starting with the classical definition of taking an average and concluding that the Wigner function can indeed be interpreted as a quantum mechanical probability function in phase space.
A classical average over a quantity χ in a phase space which is spanned by some complex quantity α is calculated by [93]

$$\langle \chi \rangle_{\text{classic}} = \int d^2\beta P_{\text{classic}}(\beta)\chi(\beta), \tag{122}$$

where $d^2\beta$ denotes the integration over the full complex phase space and P_{classic} is the classical probability density in phase space. A quantum average is taken in contrast as an average of an observable $\hat{O}$ over the full system:

$$\langle \hat{O} \rangle_\psi = \langle \psi | \hat{O} | \psi \rangle = Tr[\hat{\rho}\hat{O}], \tag{123}$$

where ρ is the density operator $\hat{\rho} = |\psi\rangle\langle\psi|$. Now let $\hat{O}$ be a functional of the amplitude operators;

$$\hat{O} \to \hat{O}(\hat{\alpha}, \hat{\alpha}^\dagger), \tag{124}$$

with the complex-valued amplitudes α and α^*, for which we have $\hat{\alpha}|\alpha\rangle = \alpha|\alpha\rangle$ and $\langle\alpha|\hat{\alpha}^\dagger = \alpha^*\langle\alpha|$. Here $|\alpha\rangle$ is a Glauber coherent state [14]. Also, We define the two quantities

$$\begin{aligned} \alpha &= \alpha\text{`} + i\alpha\text{``} \\ \beta &= -(y - ix)/2. \end{aligned} \tag{125}$$

By definition of the delta function we can write;

$$\begin{aligned} \delta(\alpha) = \delta(\alpha\text{`})\delta(\alpha\text{``}) &= \frac{1}{(2\pi)^2}\int dxdy\ \mathrm{e}^{i(\alpha\text{`}x + \alpha\text{``}y)} \\ &= \frac{1}{(2\pi)^2}\int dxdy\ \mathrm{e}^{-[(-\frac{\alpha\text{`}y}{2} - \frac{i\alpha\text{``}y}{2} - \frac{i\alpha\text{`}x}{2} + \frac{\alpha\text{``}x}{2}) - (-\frac{\alpha\text{`}y}{2} + \frac{i\alpha\text{``}y}{2} + \frac{i\alpha\text{`}x}{2} + \frac{\alpha\text{``}x}{2})]} \\ &= \frac{1}{(2\pi)^2}\int dxdy\ \mathrm{e}^{\alpha\beta(x,y)^* - \alpha^*\beta(x,y)} \\ &= \frac{1}{\pi^2}\int d^2\beta\ \mathrm{e}^{\alpha\beta^* - \alpha^*\beta} \equiv \frac{1}{\pi}\int d^2\beta\ \mathrm{e}^{\alpha^*\beta - \alpha\beta^*}. \end{aligned} \tag{126}$$

This is an interesting result, because for a functional O depending on α and $\alpha*$ we can similarly write;

$$\begin{aligned}\langle O(\gamma,\gamma^*)\rangle &= \int d^2\gamma\ \delta(\gamma-\alpha)O(\alpha,\alpha^*)\\ &= \frac{1}{\pi^2}\int d^2\beta d^2\gamma\ \mathrm{e}^{(\gamma-\alpha)\beta^*-(\gamma^*-\alpha^*)\beta}O(\gamma,\gamma^*).\end{aligned} \tag{127}$$

Now we write a quantized version of this equation by replacing γ and γ^* by the operators $\hat{a}$ and $\hat{a}^\dagger$.

$$\begin{aligned}\langle \hat{O}(\hat{a},\hat{a}^\dagger)\rangle &= \int d^2\alpha\ \hat{\delta}(\hat{a}-\alpha)O(\alpha,\alpha^*)\\ &= \frac{1}{\pi^2}\int d^2\beta d^2\alpha\ \mathrm{e}^{(\hat{a}^\dagger-\alpha^*)\beta-(\hat{a}-\alpha)\beta*}O(\alpha,\alpha^*).\end{aligned} \tag{128}$$

Here we should actually write for the delta function the following expression:

$$\hat{\delta}(\hat{a}-\alpha) = \mathrm{e}^{(\hat{a}^\dagger-\alpha^*)\beta-(\hat{a}-\alpha)\beta*} = \mathrm{e}^{\alpha\beta^*-\alpha^*\beta}\mathrm{e}^{\hat{a}^\dagger\beta-\hat{a}\beta} = \mathrm{e}^{\alpha\beta^*-\alpha^*\beta}\hat{D}(\beta), \tag{129}$$

where $\hat{D}(\beta)$ is the displacement operator. In analogy to the classical phase space average we can now write:

$$\langle \hat{O}(\hat{a},\hat{a}^\dagger)\rangle = \int d^2\beta\ \mathcal{W}(\alpha,\alpha^*)O(\beta,\beta^*), \tag{130}$$

where we have defined the quantum mechanical phase space probability density to be

$$\mathcal{W}(\alpha,\alpha^*) = \int d^2\beta\ \mathrm{e}^{\alpha\beta^*-\alpha^*\beta}\hat{D}(\beta) = \langle\hat{\delta}(\hat{a}-\alpha)\rangle = Tr[\hat{\rho}\hat{\delta}(\hat{a}-\alpha)]. \tag{131}$$

This is exactly the Wigner function. Thus we have recovered our statement that the Wigner function is a semiclassical phase space probability density.

C Chapter 2 - Hierarchy method

We present the computation for the time evolution for first-order correlation functions in the Hubbard model. We have:

$$\sigma_{jk} = \langle\hat{a}_j^\dagger\hat{a}_k\rangle = tr(\hat{a}_j^\dagger\hat{a}_k\hat{\rho}) \Rightarrow i\frac{d\hat{\sigma}_{jk}}{dt} = tr(\hat{a}_j^\dagger\hat{a}_k[\hat{\mathcal{H}},\hat{\rho})]). \tag{132}$$

We now calculate $[\hat{\mathcal{H}},\hat{a}_j^\dagger\hat{a}_k)]$, step by step. First, we aim to calculate the commutation relation with the interaction part. We will use the following relations:

$$[\hat{o},\hat{b}\hat{c}] = [\hat{o},\hat{b}]\hat{c}+\hat{b}[\hat{o},\hat{c}], \qquad [\hat{o}\hat{b},\hat{c}] = \hat{o}[\hat{b}\hat{c}]+[\hat{b}\hat{o}]\hat{c}, \tag{133}$$

$$[\hat{a}_i,\hat{a}_j^\dagger] = \delta_{ij}, \qquad [\hat{a}_i^\dagger,\hat{a}_j^\dagger] = 0, \tag{134}$$

where $\hat{o}$, $\hat{b}$ and $\hat{c}$ are arbitrary operators. We find:

$$\begin{aligned}-J[\hat{a}_{l+1}^\dagger\hat{a}_l,\hat{a}_j^\dagger\hat{a}_k] &= -J\left(a_{l+1}^\dagger[\hat{a}_l,\hat{a}_j^\dagger\hat{a}_k]+[\hat{a}_{l+1}^\dagger,\hat{a}_j^\dagger\hat{a}_k]\hat{a}_l\right)\\ &= -J\left(\hat{a}_{l+1}^\dagger\left([\hat{a}_l,\hat{a}_j^\dagger]\hat{a}_k+\hat{a}_j^\dagger[\hat{a}_l,\hat{a}_k]\right)+\left([\hat{a}_{l+1}^\dagger,\hat{a}_j^\dagger]\hat{a}_k+\hat{a}_j^\dagger[\hat{a}_{l+1}^\dagger,\hat{a}_k]\right)\hat{a}_l\right)\\ &= -J\left(a_{l+1}^\dagger\delta_{lj}\hat{a}_k-\hat{a}_j^\dagger\delta_{l+1,k}\hat{a}_l\right)\\ &= -J\left(a_{j+1}^\dagger\hat{a}_k-\hat{a}_j^\dagger\hat{a}_{k-1}\right)\end{aligned} \tag{135}$$

$$
\begin{aligned}
-J[\hat{a}_l^\dagger \hat{a}_{l+1}, \hat{a}_j^\dagger \hat{a}_k] &= -J\left(a_l^\dagger [\hat{a}_{l+1}, \hat{a}_j^\dagger \hat{a}_k] + [\hat{a}_l^\dagger, \hat{a}_j^\dagger \hat{a}_k]\hat{a}_{l+1}\right) \\
&= -J\left(a_l^\dagger \left([\hat{a}_{l+1}, \hat{a}_j^\dagger]\hat{a}_k + \hat{a}_j^\dagger [\hat{a}_{l+1}, \hat{a}_k]\right) + \left([\hat{a}_l^\dagger, \hat{a}_j^\dagger]\hat{a}_k + \hat{a}_j^\dagger [\hat{a}_l^\dagger, \hat{a}_k]\right)\hat{a}_{l+1}\right) \\
&= -J\left(a_l^\dagger \delta_{l+1,j}\hat{a}_k - \hat{a}_j^\dagger \delta_{l,k}\hat{a}_{l+1}\right) \\
&= -J\left(a_{j-1}^\dagger \hat{a}_k - \hat{a}_j^\dagger \hat{a}_{k+1}\right).
\end{aligned} \tag{136}
$$

Similarly we calculate for the interaction term:

$$
\frac{U}{2}[\hat{a}_l^\dagger \hat{a}_l^\dagger \hat{a}_l \hat{a}_l, \hat{a}_j^\dagger \hat{a}_k] = \frac{U}{2}\left([\hat{a}_l^\dagger \hat{a}_l^\dagger \hat{a}_l \hat{a}_l, \hat{a}_j^\dagger]\hat{a}_k + \hat{a}_j^\dagger [\hat{a}_l^\dagger \hat{a}_l^\dagger \hat{a}_l \hat{a}_l, \hat{a}_k]\right). \tag{137}
$$

With

$$
\begin{aligned}
[\hat{a}_l^\dagger \hat{a}_l^\dagger \hat{a}_l \hat{a}_l, \hat{a}_j^\dagger] &= \hat{a}_l^\dagger [\hat{a}_l^\dagger \hat{a}_l \hat{a}_l, \hat{a}_j^\dagger] + [\hat{a}_l^\dagger, \hat{a}_j^\dagger]\hat{a}_l^\dagger \hat{a}_l \hat{a}_l \\
&= \hat{a}_l^\dagger \left(\hat{a}_l^\dagger [\hat{a}_l \hat{a}_l, \hat{a}_j^\dagger] + [\hat{a}_l^\dagger, \hat{a}_j^\dagger]\hat{a}_l \hat{a}_l\right) \\
&= \hat{a}_l^\dagger \hat{a}_l^\dagger \left(\hat{a}_l [\hat{a}_l, \hat{a}_j^\dagger] + [\hat{a}_l, \hat{a}_j^\dagger]\hat{a}_l\right) = 2\hat{a}_j^\dagger \hat{a}_j^\dagger \hat{a}_j
\end{aligned} \tag{138}
$$

and

$$
\begin{aligned}
[\hat{a}_l^\dagger \hat{a}_l^\dagger \hat{a}_l \hat{a}_l, \hat{a}_k] &= \hat{a}_l^\dagger [\hat{a}_l^\dagger \hat{a}_l \hat{a}_l, \hat{a}_k] + [\hat{a}_l^\dagger, \hat{a}_k]\hat{a}_l^\dagger \hat{a}_l \hat{a}_l \\
&= \hat{a}_l^\dagger \left(\hat{a}_l^\dagger [\hat{a}_l \hat{a}_l, \hat{a}_k] + [\hat{a}_l^\dagger, \hat{a}_k]\hat{a}_l \hat{a}_l\right) - \hat{a}_k^\dagger \hat{a}_k \hat{a}_k = -2\hat{a}_k^\dagger \hat{a}_k \hat{a}_k
\end{aligned} \tag{139}
$$

And thus we find for the interaction term:

$$
\begin{aligned}
\frac{U}{2}[\hat{a}_l^\dagger \hat{a}_l^\dagger \hat{a}_l \hat{a}_l, \hat{a}_j^\dagger \hat{a}_k] &= U\left(\hat{a}_j^\dagger \hat{a}_j^\dagger \hat{a}_j \hat{a}_k - \hat{a}_j^\dagger \hat{a}_k^\dagger \hat{a}_k \hat{a}_k\right) \\
&= U\left(\hat{a}_j^\dagger (1 - \hat{a}_j \hat{a}_j^\dagger)\hat{a}_k - \hat{a}_j^\dagger (1 - \hat{a}_k \hat{a}_k^\dagger)\hat{a}_k\right) \\
&= U\left(\hat{a}_j^\dagger \hat{a}_j \hat{a}_j^\dagger \hat{a}_k - \hat{a}_j^\dagger \hat{a}_k \hat{a}_k^\dagger \hat{a}_k\right).
\end{aligned} \tag{140}
$$

When we put all this information together we find:

$$
[\hat{\mathcal{H}}, \hat{a}_j^\dagger \hat{a}_k)] = -J\left(\hat{a}_{j+1}^\dagger \hat{a}_k + \hat{a}_{j-1}^\dagger \hat{a}_k - \hat{a}_j^\dagger \hat{a}_{k+1} - \hat{a}_j^\dagger \hat{a}_{k-1}\right) + U\left(\hat{a}_j^\dagger \hat{a}_j \hat{a}_j^\dagger \hat{a}_k - \hat{a}_j^\dagger \hat{a}_k \hat{a}_k^\dagger \hat{a}_k\right). \tag{141}
$$

Defining

$$
\Delta_{jklm} = \langle \hat{a}_j^\dagger \hat{a}_k \hat{a}_l^\dagger \hat{a}_m \rangle - \langle \hat{a}_j^\dagger \hat{a}_k \rangle \langle \hat{a}_l^\dagger \hat{a}_m \rangle = \langle \hat{a}_j^\dagger \hat{a}_k \hat{a}_l^\dagger \hat{a}_m \rangle - \sigma_{jk}\sigma_{lm} \tag{142}
$$

we find:

$$
\begin{aligned}
i\frac{d\sigma_{jk}}{dt} &= tr\left(\hat{a}_j^\dagger \hat{a}_k[\hat{\mathcal{H}},\hat{\rho}]\right) \\
&= tr\left([\hat{\mathcal{H}},\hat{a}_j^\dagger \hat{a}_k\hat{\rho}]\right) - tr\left([\hat{\mathcal{H}},\hat{a}_j^\dagger \hat{a}_k]\hat{\rho}\right) \\
&= tr\left([\hat{\mathcal{H}},\hat{a}_j^\dagger \hat{a}_k\hat{\rho}]\right) - \langle[\hat{\mathcal{H}},\hat{a}_j^\dagger \hat{a}_k]\rangle \\
&= -J\left(\sigma_{j,k+1}+\sigma_{j,k-1}-\sigma_{j+1,k}-\sigma_{j-1,k}\right)+U\left(\Delta_{kkkj}+\sigma_{kk}\sigma kj-\Delta_{jjjk}-\sigma_{jj}\sigma_{jk}\right),
\end{aligned}
\tag{143}
$$

which is the desired result. Here we have used that $tr\left([\hat{\mathcal{H}},\hat{a}_j^\dagger \hat{a}_k\hat{\rho}]\right)=0$ due to the linearity and commutativity of the trace.

D Chapter 2 - Operator Correspondences and Wigner functions

In this chapter of the Appendix material we present detailed calculations necessary for the truncated Wigner approach. We calculate the operator correspondences required to translate between the purely quantum mechanical framework and the phase space picture. Then we calculate the time evolution of the Wigner function for the many body Hamiltonian and also the Wigner function for a coherent state, as it is necessary for the initial state sampling.

D.1 Operator correspondences

In this section of the Appendix we will calculate the operator correspondences. As the calculations are somewhat analogous and lengthy, we derive two operator correspondences explicitly. For these explicit calculations we have to compute the derivative of the Wigner function, which we will do step by step.

D.1.1 Derivative of the Bra and Ket

Consider;

$$
|\alpha\pm\frac{\beta}{2}|^2=(\alpha\pm\frac{\beta}{2})(\alpha^*\pm\frac{\beta}{2}^*)=\alpha\alpha^*+\frac{1}{4}\beta\beta^*\pm\frac{1}{2}\alpha\beta^*\pm\frac{1}{2}\alpha^*\beta \tag{144}
$$

And thus

$$
\frac{\partial}{\partial\alpha}|\alpha\pm\frac{\beta}{2}|^2=\alpha^*\pm\frac{\beta}{2}^* \tag{145}
$$

$$
\frac{\partial}{\partial\alpha^*}|\alpha\pm\frac{\beta}{2}|^2=\alpha\pm\frac{\beta}{2} \tag{146}
$$

Now we compute the derivatives of the bra and ket;

$$\begin{aligned}
\frac{\partial}{\partial\alpha}|\alpha\pm\frac{\beta}{2}\rangle &= \frac{\partial}{\partial\alpha}\left[\exp(-\frac{1}{2}|\alpha\pm\frac{\beta}{2}|^2)\sum_{n=0}^{\infty}\frac{(\alpha\pm\frac{\beta}{2})^n}{\sqrt{n!}}|n\rangle\right] \\
&= \frac{\partial}{\partial\alpha}\left[\exp(-\frac{1}{2}|\alpha\pm\frac{\beta}{2}|^2)\right]\sum_{n=0}^{\infty}\frac{(\alpha\pm\frac{\beta}{2})^n}{\sqrt{n!}}|n\rangle + \exp(-\frac{1}{2}|\alpha\pm\frac{\beta}{2}|^2)\frac{\partial}{\partial\alpha}\sum_{n=0}^{\infty}\frac{(\alpha\pm\frac{\beta}{2}a)^n}{\sqrt{n!}}|n\rangle \\
&= -\frac{1}{2}(\alpha^*\pm\frac{\beta}{2}^*)|\alpha\pm\frac{\beta}{2}\rangle + \exp(-\frac{1}{2}|\alpha\pm\frac{\beta}{2}|^2)\sum_{n=0}^{\infty}n\frac{(\alpha\pm\frac{\beta}{2})^{n-1}}{\sqrt{n!}}|n\rangle \\
&= -\frac{1}{2}(\alpha^*\pm\frac{\beta}{2}^*)|\alpha\pm\frac{\beta}{2}\rangle + \exp(-\frac{1}{2}|\alpha\pm\frac{\beta}{2}|^2)\sum_{n=0}^{\infty}\frac{(\alpha\pm\frac{\beta}{2})^{n-1}}{\sqrt{(n-1)!}}\sqrt{n}|n\rangle \\
&= -\frac{1}{2}(\alpha^*\pm\frac{\beta}{2}^*)|\alpha\pm\frac{\beta}{2}\rangle + \exp(-\frac{1}{2}|\alpha\pm\frac{\beta}{2}|^2)\sum_{m=0}^{\infty}\frac{(\alpha\pm\frac{\beta}{2})^{m}}{\sqrt{m!}}\sqrt{m}|m+1\rangle \\
&= -\frac{1}{2}(\alpha^*\pm\frac{\beta}{2}^*)|\alpha\pm\frac{\beta}{2}\rangle + \hat{a}^\dagger|\alpha\pm\frac{\beta}{2}\rangle
\end{aligned} \tag{147}$$

And thus by complex conjugation we also know that;

$$\frac{\partial}{\partial\alpha^*}\langle\alpha\pm\frac{\beta}{2}| = -\frac{1}{2}(\alpha+\frac{\beta}{2})\langle\alpha\pm\frac{\beta}{2}| + \langle\alpha\pm\frac{\beta}{2}|\hat{a} \tag{148}$$

Furthermore;

$$\begin{aligned}
\frac{\partial}{\partial\alpha^*}|\alpha\pm\frac{\beta}{2}\rangle &= \frac{\partial}{\partial\alpha^*}\left[\exp(-\frac{1}{2}|\alpha\pm\frac{\beta}{2}|^2)\right]\sum_{n=0}^{\infty}\frac{(\alpha\pm\frac{\beta}{2})^n}{\sqrt{n!}}|n\rangle + \exp(-\frac{1}{2}|\alpha\pm\frac{\beta}{2}|^2)\frac{\partial}{\partial\alpha^*}\sum_{n=0}^{\infty}\frac{(\alpha\pm\frac{\beta}{2})^n}{\sqrt{n!}}|n\rangle \\
&= \frac{\partial}{\partial\alpha^*}\left[\exp(-\frac{1}{2}|\alpha\pm\frac{\beta}{2}|^2)\right]\sum_{n=0}^{\infty}\frac{(\alpha\pm\frac{\beta}{2})^n}{\sqrt{n!}}|n\rangle \\
&= -\frac{1}{2}(\alpha\pm\frac{\beta}{2})|\alpha\pm\frac{\beta}{2}\rangle
\end{aligned} \tag{149}$$

And thus by complex conjugation;

$$\frac{\partial}{\partial\alpha}\langle\alpha\pm\frac{\beta}{2}| = -\frac{1}{2}(\alpha^*\pm\frac{\beta}{2}^*)\langle\alpha\pm\frac{\beta}{2}| \tag{150}$$

D.1.2 Derivative of the Wigner Function

$$\begin{aligned}
\frac{\partial}{\partial\alpha}\mathcal{W} &= \frac{1}{\pi}\frac{\partial}{\partial\alpha}\int d^2\beta \mathrm{e}^{(\alpha\beta^*-\alpha^*\beta)}\langle\alpha-\frac{\beta}{2}|\rho|\alpha+\frac{\beta}{2}\rangle \\
&= \frac{1}{\pi}\int d^2\beta\left[\left(\frac{\partial}{\partial\alpha}\mathrm{e}^{(\alpha\beta^*-\alpha^*\beta)}\right)\langle\alpha-\frac{\beta}{2}|\rho|\alpha+\frac{\beta}{2}\rangle + \mathrm{e}^{(\alpha\beta^*-\alpha^*\beta)}\left(\frac{\partial}{\partial\alpha}\langle\alpha-\frac{\beta}{2}|\right)\rho|\alpha+\frac{\beta}{2}\rangle\right. \\
&\left.+\mathrm{e}^{(\alpha\beta^*-\alpha^*\beta)}\langle\alpha-\frac{\beta}{2}|\rho\left(\frac{\partial}{\partial\alpha}|\alpha+\frac{\beta}{2}\rangle\right)\right] \\
&= \frac{1}{\pi}\int d^2\beta\left[\beta^*\cdot\mathrm{e}^{(\alpha\beta^*-\alpha^*\beta)}\langle\alpha-\frac{\beta}{2}|\rho|\alpha+\frac{\beta}{2}\rangle - \frac{1}{2}(\alpha^*-\frac{\beta}{2}^*)\cdot\mathrm{e}^{(\alpha\beta^*-\alpha^*\beta)}\langle\alpha-\frac{\beta}{2}|\rho|\alpha+\frac{\beta}{2}\rangle\right. \\
&\left.+\mathrm{e}^{(\alpha\beta^*-\alpha^*\beta)}\langle\alpha-\frac{\beta}{2}|\rho\hat{a^\dagger}|\alpha+\frac{\beta}{2}\rangle - \frac{1}{2}(\alpha^*+\frac{\beta}{2}^*)\cdot\mathrm{e}^{(\alpha\beta^*-\alpha^*\beta)}\langle\alpha-\frac{\beta}{2}|\rho|\alpha+\frac{\beta}{2}\rangle\right] \\
&= \langle\beta^*\rangle_{\mathcal{W}} - \alpha^*\mathcal{W} + \frac{1}{\pi}\int d^2\beta\mathrm{e}^{(\alpha\beta^*-\alpha^*\beta)}\langle\alpha-\frac{\beta}{2}|\rho\hat{a^\dagger}|\alpha+\frac{\beta}{2}\rangle
\end{aligned} \tag{151}$$

Next we have to calculate $\langle\beta\rangle_{\mathcal{W}}$, which represents the expectation value of the Wigner function as quasiprobability. We define

$$f(\beta) = \mathrm{e}^{(\alpha\beta^*-\alpha^*\beta)}\langle\alpha-\frac{\beta}{2}|\rho|\alpha+\frac{\beta}{2}\rangle. \tag{152}$$

Note that $f(-\beta) = f(\beta)^*$, since:

$$\begin{aligned}
f(\beta)^* &= \mathrm{e}^{(\alpha^*\beta-\alpha\beta^*)}\langle\alpha+\frac{\beta}{2}|\rho^\dagger|\alpha-\frac{\beta}{2}\rangle \\
&= \mathrm{e}^{(\alpha^*\beta-\alpha\beta^*)}\langle\alpha+\frac{\beta}{2}|\rho|\alpha-\frac{\beta}{2}\rangle = f(-\beta).
\end{aligned} \tag{153}$$

And thus the integration $\langle\beta^*\rangle$ vanishes for reasons of symmetry. This proves:

$$\left(\alpha^*+\frac{\partial}{\partial\alpha}\right)\mathcal{W} \longleftrightarrow \hat{\rho}\hat{a}^\dagger \tag{154}$$

We repeat the calculations with the derrivative for α^*;

$$\begin{aligned}
\frac{\partial}{\partial\alpha^*}\mathcal{W} &= \frac{1}{\pi}\frac{\partial}{\partial\alpha^*}\int d^2\beta \mathrm{e}^{(\alpha\beta^*-\alpha^*\beta)}\langle\alpha-\frac{\beta}{2}|\rho|\alpha+\frac{\beta}{2}\rangle \\
&= \frac{1}{\pi}\int d^2\beta\left[\left(\frac{\partial}{\partial\alpha^*}\mathrm{e}^{(\alpha\beta^*-\alpha^*\beta)}\right)\langle\alpha-\frac{\beta}{2}|\rho|\alpha+\frac{\beta}{2}\rangle + \mathrm{e}^{(\alpha\beta^*-\alpha^*\beta)}\left(\frac{\partial}{\partial\alpha^*}\langle\alpha-\frac{\beta}{2}|\right)\rho|\alpha+\frac{\beta}{2}\rangle\right. \\
&\left.+\mathrm{e}^{(\alpha\beta^*-\alpha^*\beta)}\langle\alpha-\frac{\beta}{2}|\rho\left(\frac{\partial}{\partial\alpha^*}|\alpha+\frac{\beta}{2}\rangle\right)\right] \\
&= \frac{1}{\pi}\int d^2\beta\left[\beta\cdot\mathrm{e}^{(\alpha\beta^*-\alpha^*\beta)}\langle\alpha-\frac{\beta}{2}|\rho|\alpha+\frac{\beta}{2}\rangle - \frac{1}{2}(\alpha-\frac{\beta}{2})\cdot\mathrm{e}^{(\alpha\beta^*-\alpha^*\beta)}\langle\alpha-\frac{\beta}{2}|\rho|\alpha+\frac{\beta}{2}\rangle\right. \\
&\left.+\mathrm{e}^{(\alpha\beta^*-\alpha^*\beta)}\langle\alpha-\frac{\beta}{2}|\hat{a}\rho|\alpha+\frac{\beta}{2}\rangle - \frac{1}{2}(\alpha+\frac{\beta}{2})\cdot\mathrm{e}^{(\alpha\beta^*-\alpha^*\beta)}\langle\alpha-\frac{\beta}{2}|\rho|\alpha+\frac{\beta}{2}\rangle\right] \\
&= \langle\beta^*\rangle_{\mathcal{W}} - \alpha\mathcal{W} + \frac{1}{\pi}\int d^2\beta\mathrm{e}^{(\alpha\beta^*-\alpha^*\beta)}\langle\alpha-\frac{\beta}{2}|\hat{a}\rho|\alpha+\frac{\beta}{2}\rangle.
\end{aligned} \tag{155}$$

This gives us:

$$\left(\alpha+\frac{\partial}{\partial\alpha^*}\right)\mathcal{W} \longleftrightarrow \hat{a}\hat{\rho}. \tag{156}$$

This result is also in perfect alignment with [15]. The other two operator correspondences are not obvious in the coherent state basis. In Sec. 3.6 we follow the approach taken in [14] we closely follow the approach taken in [14] for the computation of the operator correspondences. The details of the calculation are found in Appendix E. With this approach, one easily gets all four operator correspondences, necessary to translate the system into the quasi-probabilistic framework of the Wigner function.

D.2 Computation of the time evolution for the Wigner function

We intend to translate the master equation describing the time evolution of the quantum mechanical system into the context of the phase space methods. The master equation reads the following:

$$\frac{d}{dt}\hat{\rho}(t) = -i[\hat{\mathcal{H}},\rho(t)] + \hat{\mathcal{L}}_{\text{loss}}\hat{\rho}(t). \tag{157}$$

With the Hamiltonian being the Hubbard Hamiltonian and the loss term given by;

$$\mathcal{H} \equiv \mathcal{H}_{\text{jump}} + \mathcal{H}_{\text{int}} = -J\sum_j(\hat{a}_{j+1}^\dagger\hat{a_j} + \hat{a}_j^\dagger\hat{a}_{j+1}) + \frac{U}{2}\sum_j\hat{a}_j^\dagger\hat{a}_j^\dagger\hat{a}_j\hat{a}_j \tag{158}$$

and the loss term is given by

$$\hat{\mathcal{L}}_{\text{loss}}\hat{\rho}(t) = -\sum_j\frac{\gamma_j}{2}(\hat{a}_j^\dagger\hat{a}_j\hat{\rho} + \hat{\rho}\hat{a}_j^\dagger\hat{a}_j - 2\hat{a}_j\hat{\rho}\hat{a}_j^\dagger). \tag{159}$$

Step by step we will introduce the operator correspondences, translating the master equation into an equation of motion for the Wigner function.

$$
\begin{aligned}
[\hat{\mathcal{H}_{\text{jump}}}, \hat{\rho}(t)] &= -J \sum_j \left(\hat{a}_{j+1}^\dagger \hat{a_j} \hat{\rho} + \hat{a}_j^\dagger \hat{a}_{j+1} \hat{\rho} - \hat{\rho} \hat{a}_{j+1}^\dagger \hat{a_j} - \hat{\rho} \hat{a}_j^\dagger \hat{a}_{j+1} \right) \\
&\leftrightarrow -J \sum_j \left[\left(\alpha_{j+1}^* - \frac{\partial}{\partial \alpha_{j+1}} \right) \left(\alpha_j + \frac{\partial}{\partial \alpha_j^*} \right) + \left(\alpha_j^* - \frac{\partial}{\partial \alpha_j} \right) \left(\alpha_{j+1} + \frac{\partial}{\partial \alpha_{j+1}^*} \right) \right. \\
&\quad \left. - \left(\alpha_{j+1}^* + \frac{\partial}{\partial \alpha_{j+1}} \right) \left(\alpha_j - \frac{\partial}{\partial \alpha_j^*} \right) - \left(\alpha_j^* + \frac{\partial}{\partial \alpha_j} \right) \left(\alpha_{j+1} - \frac{\partial}{\partial \alpha_{j+1}^*} \right) \right] \mathcal{W} \\
&\equiv -J \sum_j \left[A_j + B_j - C_j - D_j \right] \mathcal{W}
\end{aligned}
\tag{160}
$$

We then find;

$$
A_j^* = \left(\alpha_{j+1}^* - \frac{\partial}{\partial \alpha_{j+1}} \right)^* \left(\alpha_j + \frac{\partial}{\partial \alpha_j^*} \right)^* = \left(\alpha_{j+1} - \frac{\partial}{\partial \alpha_{j+1}^*} \right) \left(\alpha_j^* + \frac{\partial}{\partial \alpha_j} \right) = D_j \tag{161}
$$

$$
B_j^* = \left(\alpha_j^* - \frac{\partial}{\partial \alpha_j} \right)^* \left(\alpha_{j+1} + \frac{\partial}{\partial \alpha_{j+1}^*} \right)^* = \left(\alpha_j - \frac{\partial}{\partial \alpha_j^*} \right) \left(\alpha_{j+1}^* + \frac{\partial}{\partial \alpha_{j+1}} \right) = C_j. \tag{162}
$$

Thus,

$$
\begin{aligned}
[\hat{\mathcal{H}_{\text{jump}}}, \hat{\rho}(t)] &= -J \sum_j \left[A_j + B_j - C_j - D_j \right] \mathcal{W} \\
&= +J \sum_j \left[A_j^* + C_j - C_j^* - A_j \right] \mathcal{W} \\
&= 2i \cdot J \sum_j \text{Im} \left[C_j - A_j \right] \mathcal{W} \\
&= 2i \cdot J \sum_j \text{Im} \left[\left(\alpha_j - \frac{\partial}{\partial \alpha_j^*} \right) \left(\alpha_{j+1}^* + \frac{\partial}{\partial \alpha_{j+1}} \right) - \left(\alpha_{j+1}^* - \frac{\partial}{\partial \alpha_{j+1}} \right) \left(\alpha_j + \frac{\partial}{\partial \alpha_j^*} \right) \right] \mathcal{W}.
\end{aligned}
\tag{163}
$$

Similarly we find for the interaction term;

$$
\begin{aligned}
[\hat{\mathcal{H}}_{\text{int}}, \hat{\rho}(t)] &= \frac{U}{2} \sum_j \left(\hat{a}_j^\dagger \hat{a}_j^\dagger \hat{a}_j \hat{a}_j \hat{\rho} - \hat{\rho} \hat{a}_j^\dagger \hat{a}_j^\dagger \hat{a}_j \hat{a}_j \right) \\
&\leftrightarrow \frac{U}{2} \sum_j \left[\left(\alpha_j^* - \frac{\partial}{\partial \alpha_j} \right)^2 \left(\alpha_j + \frac{\partial}{\partial \alpha_j^*} \right)^2 - \left(\alpha_j^* + \frac{\partial}{\partial \alpha_j} \right)^2 \left(\alpha_j - \frac{\partial}{\partial \alpha_j^*} \right)^2 \right] \mathcal{W} \\
&= iU \sum_j \text{Im} \left[\left(\alpha_j^* - \frac{\partial}{\partial \alpha_j} \right)^2 \left(\alpha_j + \frac{\partial}{\partial \alpha_j^*} \right)^2 \right] \mathcal{W}.
\end{aligned}
\tag{164}
$$

And for the loss term we find;

$$\hat{L}_{\text{loss}}\hat{\rho}(t) = -\sum_j \frac{\gamma_j}{2}(\hat{a}_j^\dagger \hat{a}_j \hat{\rho} + \hat{\rho}\hat{a}_j^\dagger \hat{a}_j - 2\hat{a}_j \hat{\rho} \hat{a}_j^\dagger)$$

$$\leftrightarrow -\sum_j \frac{\gamma_j}{2}\left[\left(\alpha_j^* - \frac{\partial}{\partial \alpha_j}\right)\left(\alpha_j + \frac{\partial}{\partial \alpha_j^*}\right) + \left(\alpha_j^* + \frac{\partial}{\partial \alpha_j}\right)\left(\alpha_j - \frac{\partial}{\partial \alpha_j^*}\right) - 2\left(\alpha_j + \frac{\partial}{\partial \alpha_j^*}\right)\left(\alpha_j^* + \frac{\partial}{\partial \alpha_j}\right)\right]\mathcal{W} \tag{165}$$

We put all these terms into the master equation;

$$\frac{d}{dt}\hat{\rho}(t) = -i[\hat{\mathcal{H}}, \rho(t)] + \hat{\mathcal{L}}_{\text{loss}}\hat{\rho}(t)$$

$$\leftrightarrow \partial_t \mathcal{W} = 2J\sum_j \text{Im}\left[\left(\alpha_j - \frac{\partial}{\partial \alpha_j^*}\right)\left(\alpha_{j+1}^* + \frac{\partial}{\partial \alpha_{j+1}}\right) - \left(\alpha_{j+1}^* - \frac{\partial}{\partial \alpha_{j+1}}\right)\left(\alpha_j + \frac{\partial}{\partial \alpha_j^*}\right)\right]\mathcal{W}$$

$$+ U\sum_j \text{Im}\left[\left(\alpha_j^* - \frac{\partial}{\partial \alpha_j}\right)^2\left(\alpha_j + \frac{\partial}{\partial \alpha_j^*}\right)^2\right]\mathcal{W} - \sum_j \frac{\gamma_j}{2}\left[\left(\alpha_j^* - \frac{\partial}{\partial \alpha_j}\right)\left(\alpha_j + \frac{\partial}{\partial \alpha_j^*}\right)\right. \tag{166}$$

$$\left. + \left(\alpha_j^* + \frac{\partial}{\partial \alpha_j}\right)\left(\alpha_j - \frac{\partial}{\partial \alpha_j^*}\right) - 2\left(\alpha_j + \frac{\partial}{\partial \alpha_j^*}\right)\left(\alpha_j^* + \frac{\partial}{\partial \alpha_j}\right)\right]\mathcal{W},$$

which gives us an equation of motion for the Wigner function. One term is highlighted in red, as it deviates with relative signs from the results of Ref. [7], which there appears to be a typo.

We continue to describe this equation by the real and imaginary part of α and α^*. Due to the rules of complex Wirtinger differentiation we have;

$$\alpha_j = x_j + iy_j \tag{167}$$

$$\alpha_j^* = x_j - iy_j \tag{168}$$

$$\frac{\partial}{\partial \alpha_j} = \frac{1}{2}\left(\frac{\partial}{\partial x_j} - i\frac{\partial}{\partial y_j}\right) \tag{169}$$

$$\frac{\partial}{\partial \alpha_j^*} = \frac{1}{2}\left(\frac{\partial}{\partial x_j} + i\frac{\partial}{\partial y_j}\right). \tag{170}$$

For the hopping term we find;

$$\begin{aligned}
\text{HOPPING} &= 2J\sum_j \text{Im}\left[\left(\alpha_j - \frac{\partial}{\partial\alpha_j^*}\right)\left(\alpha_{j+1}^* + \frac{\partial}{\partial\alpha_{j+1}}\right) - \left(\alpha_{j+1}^* - \frac{\partial}{\partial\alpha_{j+1}}\right)\left(\alpha_j + \frac{\partial}{\partial\alpha_j^*}\right)\right]\mathcal{W} \\
&\leftrightarrow 2J\sum_j \text{Im}\left[\left(x_j + iy_j - \frac{1}{2}\frac{\partial}{\partial x_j} - i\frac{1}{2}\frac{\partial}{\partial y_j}\right)\left(x_{j+1} - iy_{j+1} + \frac{1}{2}\frac{\partial}{\partial x_{j+1}} - i\frac{1}{2}\frac{\partial}{\partial y_{j+1}}\right)\right. \\
&\quad \left. - \left(x_{j+1} - iy_{j+1} - \frac{1}{2}\frac{\partial}{\partial x_{j+1}} + i\frac{1}{2}\frac{\partial}{\partial y_{j+1}}\right)\left(x_j + iy_j + \frac{1}{2}\frac{\partial}{\partial x_j} + i\frac{1}{2}\frac{\partial}{\partial y_j}\right)\right]\mathcal{W} \\
&= 2J\sum_j \left[\left(-x_jy_{j+1} + y_jx_{j+1} - \frac{x_j}{2}\frac{\partial}{\partial y_{j+1}} + \frac{y_j}{2}\frac{\partial}{\partial x_{j+1}} - \frac{x_{j+1}}{2}\frac{\partial}{\partial y_j} + \frac{y_{j+1}}{2}\frac{\partial}{\partial x_j} + \frac{1}{4}\frac{\partial}{\partial x_j}\frac{\partial}{\partial y_{j+1}} - \frac{1}{4}\frac{\partial}{\partial y_j}\frac{\partial}{\partial x_{j+1}}\right)\right. \\
&\quad \left. - \left(-x_jy_{j+1} + y_jx_{j+1} + \frac{x_j}{2}\frac{\partial}{\partial y_{j+1}} - \frac{y_j}{2}\frac{\partial}{\partial x_{j+1}} + \frac{x_{j+1}}{2}\frac{\partial}{\partial y_j} - \frac{y_{j+1}}{2}\frac{\partial}{\partial x_j} + \frac{1}{4}\frac{\partial}{\partial x_j}\frac{\partial}{\partial y_{j+1}} - \frac{1}{4}\frac{\partial}{\partial y_j}\frac{\partial}{\partial x_{j+1}}\right)\right]\mathcal{W} \\
&= 2J\sum_j \left[\left(-x_j\frac{\partial}{\partial y_{j+1}} + y_j\frac{\partial}{\partial x_{j+1}} - x_{j+1}\frac{\partial}{\partial y_j} + y_{j+1}\frac{\partial}{\partial x_j}\right)\right]\mathcal{W} \\
&= 2J\sum_j \left[\frac{\partial}{\partial x_j}\left(y_{j+1} + y_{j-1}\right) - \frac{\partial}{\partial y_j}\left(x_{j+1} + x_{j-1}\right)\right]\mathcal{W}
\end{aligned} \tag{171}$$

For the interaction term we find;

$$\text{INT} = U\sum_j \text{Im}\left[\left(\alpha_j^* - \frac{\partial}{\partial\alpha_j}\right)^2\left(\alpha_j + \frac{\partial}{\partial\alpha_j^*}\right)^2\right]\mathcal{W} \equiv U\sum_j \text{Im}[A_j^2 \cdot B_j^2]\mathcal{W} \tag{172}$$

The equations frequently show the symmetry

$$\left[x\frac{\partial}{\partial x} - y\frac{\partial}{\partial y}\right]\mathcal{W}(x,y) = \left[\frac{\partial}{\partial x}x - \frac{\partial}{\partial y}y\right]\mathcal{W}(x,y), \tag{173}$$

which simplifies the calculations and is used in the following calculations.

$$\begin{aligned}
A_j^2 &= \left(\alpha_j^* - \frac{\partial}{\partial\alpha_j}\right)^2 = \left(x_j - iy_j - \frac{1}{2}\frac{\partial}{\partial x_j} + i\frac{1}{2}\frac{\partial}{\partial y_j}\right)^2 \\
&= x_j^2 - 2ix_jy_j - y_j^2 + iy_j\frac{\partial}{\partial x_j} - x_j\frac{\partial}{\partial x_j} + y_j\frac{\partial}{\partial y_j} + ix\frac{\partial}{\partial y_j} - \frac{i}{2}\frac{\partial}{\partial x_j}\frac{\partial}{\partial y_j} + \frac{1}{4}\frac{\partial^2}{\partial x_j^2} - \frac{1}{4}\frac{\partial^2}{\partial y_j^2}
\end{aligned} \tag{174}$$

$$\begin{aligned}
B_j^2 &= \left(\alpha_j + \frac{\partial}{\partial\alpha_j^*}\right)^2 = \left(x_j + iy_j + \frac{1}{2}\frac{\partial}{\partial x_j} + i\frac{1}{2}\frac{\partial}{\partial y_j}\right)^2 \\
&= x_j^2 + 2ix_jy_j - y_j^2 + iy_j\frac{\partial}{\partial x_j} + x_j\frac{\partial}{\partial x_j} - y_j\frac{\partial}{\partial y_j} + ix\frac{\partial}{\partial y_j} + \frac{i}{2}\frac{\partial}{\partial x_j}\frac{\partial}{\partial y_j} + \frac{1}{4}\frac{\partial^2}{\partial x_j^2} - \frac{1}{4}\frac{\partial^2}{\partial y_j^2}
\end{aligned} \tag{175}$$

In the following we have to multiply $Im(A_j^2 B_j^2)$. This multiplication produces many terms. We sort them by order to achieve some level of overview. $\mathcal{O}_i$ are all terms that produce terms of order i in the multiplication.

$$\mathcal{O}_0(\mathrm{Im}(A_j^2 B_j^2)) = 2x_j^3 y_j - 2x_j y_j^2 - 2x_j^3 y_j + 2x_j y_j^2 = 0 \tag{176}$$

$$\begin{aligned}\mathcal{O}_1(\mathrm{Im}(A_j^2 B_j^2)) = &\left(x_j^2 y_j \frac{\partial}{\partial x_j} + x_j^3 \frac{\partial}{\partial y_j} - 2x_j^2 y_j \frac{\partial}{\partial x_j} + 2x_j y_j^2 \frac{\partial}{\partial y_j} - y_j^3 \frac{\partial}{\partial x_j} - x_j y_j^2 \frac{\partial}{\partial y_j} + \right. \\ &\left. + x_j^2 y_j \frac{\partial}{\partial x_j} + x_j^3 \frac{\partial}{\partial y_j} - 2x_j^2 y_j \frac{\partial}{\partial x_j} + 2x_j y_j^2 \frac{\partial}{\partial y_j} - y_j^3 \frac{\partial}{\partial x_j} - x_j y_j^2 \frac{\partial}{\partial y_j} \right) \\ = &-2\frac{\partial}{\partial x_j}(+x_j^2 y_j + y_j^3) + 2\frac{\partial}{\partial y_j}(x_j y_j^2 + x_j^3)\end{aligned} \tag{177}$$

$$\begin{aligned}\mathcal{O}_2(\mathrm{Im}(A_j^2 B_j^2)) = &\frac{x_j^2}{2}\frac{\partial}{\partial x_j}\frac{\partial}{\partial y_j} - \frac{x_j y_j}{2}\frac{\partial^2}{\partial x_j^2} + \frac{x_j y_j}{2}\frac{\partial^2}{\partial y_j^2} - \frac{y_j^2}{2}\frac{\partial}{\partial x_j}\frac{\partial}{\partial y_j} \\ &- \frac{x_j^2}{2}\frac{\partial}{\partial x_j}\frac{\partial}{\partial y_j} + \frac{x_j y_j}{2}\frac{\partial^2}{\partial x_j^2} - \frac{x_j y_j}{2}\frac{\partial^2}{\partial y_j^2} + \frac{y_j^2}{2}\frac{\partial}{\partial x_j}\frac{\partial}{\partial y_j} \\ &+ 2x_j y_j \frac{\partial^2}{\partial x_j^2} - 2y_j^2 \frac{\partial}{\partial x_j}\frac{\partial}{\partial y_j} - 2x_j y_j \frac{\partial^2}{\partial x_j^2} - 2x_j^2 \frac{\partial}{\partial x_j}\frac{\partial}{\partial y_j} \\ &+ 2y_j^2 \frac{\partial}{\partial x_j}\frac{\partial}{\partial y_j} + 2x_j y_j \frac{\partial^2}{\partial y_j^2} + 2x_j^2 \frac{\partial}{\partial x_j}\frac{\partial}{\partial y_j} - 2x_j y_j \frac{\partial^2}{\partial y_j^2} \\ = &\,0\end{aligned} \tag{178}$$

$$\begin{aligned}\mathcal{O}_3(\mathrm{Im}(A_j^2 B_j^2)) = &\frac{y_j}{2}\frac{\partial^2}{\partial x_j^3} - \frac{y_j}{2}\frac{\partial}{\partial x_j}\frac{\partial^2}{\partial y_j^2} - 2x_j \frac{\partial}{\partial^2 x_j^2}\frac{\partial}{\partial y_j} + 2y_j \frac{\partial}{\partial x_j}\frac{\partial^2}{\partial y_j^2} + \frac{x_j}{2}\frac{\partial^2}{\partial x_j^2}\frac{\partial}{\partial y_j} - \frac{x_j}{2}\frac{\partial^3}{\partial y_j^3} \\ &+ \frac{y_j}{2}\frac{\partial^2}{\partial x_j^3} - \frac{y_j}{2}\frac{\partial}{\partial x_j}\frac{\partial^2}{\partial y_j^2} - 2x_j \frac{\partial}{\partial^2 x_j^2}\frac{\partial}{\partial y_j} + 2y_j \frac{\partial}{\partial x_j}\frac{\partial^2}{\partial y_j^2} + \frac{x_j}{2}\frac{\partial^2}{\partial x_j^2}\frac{\partial}{\partial y_j} - \frac{x_j}{2}\frac{\partial^3}{\partial y_j^3} \\ &+ \frac{3}{4}\frac{\partial}{\partial x_j}\frac{\partial}{\partial y_j} - \frac{3}{4}\frac{\partial}{\partial x_j}\frac{\partial}{\partial y_j} \\ = &\, y_j \frac{\partial^2}{\partial x_j^3} - y_j \frac{\partial}{\partial x_j}\frac{\partial^2}{\partial y_j^2} + 4y_j \frac{\partial}{\partial x_j}\frac{\partial^2}{\partial y_j^2} - 4x_j \frac{\partial}{\partial^2 x_j^2}\frac{\partial}{\partial y_j} + x_j \frac{\partial^2}{\partial x_j^2}\frac{\partial}{\partial y_j} - x_j \frac{\partial^3}{\partial y_j^3} \\ = &\, y_j \frac{\partial^2}{\partial x_j^3} + 3y_j \frac{\partial}{\partial x_j}\frac{\partial^2}{\partial y_j^2} - 3x_j \frac{\partial^2}{\partial x_j^2}\frac{\partial}{\partial y_j} - x_j \frac{\partial^3}{\partial y_j^3}\end{aligned} \tag{179}$$

Here, the additional second order terms stem from the commutation operations along the calculation, but eliminate each other.

$$\mathcal{O}_4(\mathrm{Im}(A_j^2 B_j^2) = -\frac{1}{8}\frac{\partial^3}{\partial x_j^3}\frac{\partial}{\partial y_j} + \frac{1}{8}\frac{\partial}{\partial x_j}\frac{\partial^3}{\partial y_j^3} + \frac{1}{8}\frac{\partial^3}{\partial x_j^3}\frac{\partial}{\partial y_j} - \frac{1}{8}\frac{\partial}{\partial x_j}\frac{\partial^3}{\partial y_j^3} = 0 \tag{180}$$

And thus we find;

$$\begin{aligned}
\text{INT} &= U\sum_j \left[\mathcal{O}_1(\text{Im}(A_j^2B_j^2)) + O_3(\text{Im}(A_j^2B_j^2))\right] \\
&= 2U\sum_j \Bigg[-\frac{\partial}{\partial x_j}(+x_j^2y_j + y_j^3) + \frac{\partial}{\partial y_j}(x_jy_j^2 + x_j^3) \\
&\quad + y_j\left(\frac{\partial^2}{\partial x_j^3} + 3\frac{\partial}{\partial x_j}\frac{\partial^2}{\partial y_j^2}\right) - x_j\left(\frac{\partial^3}{\partial y_j^3} + 3\frac{\partial}{\partial^2 x_j^2}\frac{\partial}{\partial y_j}\right)\Bigg]
\end{aligned} \tag{181}$$

Here, the second order contribution stems from the calculations for the third order terms and comes from the commutations of the operators. For the decay term we find;

$$\begin{aligned}
\text{DECAY} &= -\sum_j \frac{\gamma_j}{2}\Bigg[\left(\alpha_j^* - \frac{\partial}{\partial\alpha_j}\right)\left(\alpha_j + \frac{\partial}{\partial\alpha_j^*}\right) + \left(\alpha_j^* + \frac{\partial}{\partial\alpha_j}\right)\left(\alpha_j - \frac{\partial}{\partial\alpha_j^*}\right) \\
&\quad -2\left(\alpha_j + \frac{\partial}{\partial\alpha_j^*}\right)\left(\alpha_j^* + \frac{\partial}{\partial\alpha_j}\right)\Bigg]\mathcal{W} \\
&= -\sum_j \frac{\gamma_j}{2}\Bigg[\left(x_j - iy_j - \frac{1}{2}\frac{\partial}{\partial x_j} + i\frac{1}{2}\frac{\partial}{\partial y_j}\right)\left(x_j + iy_j + \frac{1}{2}\frac{\partial}{\partial x_j} + i\frac{1}{2}\frac{\partial}{\partial y_j}\right) \\
&\quad + \left(x_j - iy_j + \frac{1}{2}\frac{\partial}{\partial x_j} - i\frac{1}{2}\frac{\partial}{\partial y_j}\right)\left(x_j + iy_j - \frac{1}{2}\frac{\partial}{\partial x_j} - i\frac{1}{2}\frac{\partial}{\partial y_j}\right) \\
&\quad -2\left(x_j + iy_j + \frac{1}{2}\frac{\partial}{\partial x_j} + i\frac{1}{2}\frac{\partial}{\partial y_j}\right)\left(x_j - iy_j + \frac{1}{2}\frac{\partial}{\partial x_j} - i\frac{1}{2}\frac{\partial}{\partial y_j}\right)\Bigg]\mathcal{W} \\
&= -\sum_j \frac{\gamma_j}{2}\Bigg[\left(x_j^2 + y_j^2 + ix_j\frac{1}{2}\frac{\partial}{\partial y_j} - iy_j\frac{1}{2}\frac{\partial}{\partial x_j} - \frac{1}{4}\frac{\partial^2}{\partial x_j^2} - \frac{1}{4}\frac{\partial^2}{\partial y_j^2}\right) \\
&\quad + \left(x_j^2 + y_j^2 - ix_j\frac{1}{2}\frac{\partial}{\partial y_j} + iy_j\frac{1}{2}\frac{\partial}{\partial x_j} - \frac{1}{4}\frac{\partial^2}{\partial x_j^2} - \frac{1}{4}\frac{\partial^2}{\partial y_j^2}\right) \\
&\quad -2\left(x_j^2 + y_j^2 + x_j\frac{1}{2}\frac{\partial}{\partial x_j} + y_j\frac{1}{2}\frac{\partial}{\partial y_j} + \frac{1}{4}\frac{\partial^2}{\partial x_j^2} + \frac{1}{4}\frac{\partial^2}{\partial y_j^2}\right)\Bigg]\mathcal{W} \\
&= \frac{1}{2}\sum_j \gamma_j\left(x_j\frac{\partial}{\partial x_j} + y_j\frac{\partial}{\partial y_j} + \frac{\partial^2}{\partial x_j^2} + \frac{\partial^2}{\partial y_j^2}\right)\mathcal{W}
\end{aligned} \tag{182}$$

When we put all this information together we find the equation of motion for the Wigner function in

terms of x_j and y_j;

$$\begin{aligned}\frac{d}{dt}\hat{\rho}(t) \leftrightarrow \partial_t \mathcal{W} = &\sum_j \left[\frac{\partial}{\partial x_j}\left(2J(y_{j+1}+y_{j-1}) - 2U(x_j^2 y_j + y_j^3) + \frac{\gamma_j}{2}x_j\right)\right]\mathcal{W} \\ &+ \sum_j \left[\frac{\partial}{\partial y_j}\left(-2J(x_{j+1}+x_{j-1}) + 2U(x_j y_j^2 + x_j^3) + \frac{\gamma_j}{2}y_j\right)\right]\mathcal{W} \\ &+ \frac{1}{2}\sum_j \gamma_j \left(\frac{\partial^2}{\partial x_j^2} + \frac{\partial^2}{\partial y_j^2}\right)\mathcal{W} \\ &+ U\sum_j \left[y_j\left(\frac{\partial^2}{\partial x_j^3} + 3\frac{\partial}{\partial x_j}\frac{\partial^2}{\partial y_j^2}\right) - x_j\left(\frac{\partial^3}{\partial y_j^3} + 3\frac{\partial^2}{\partial x_j^2}\frac{\partial}{\partial y_j}\right)\right]\mathcal{W}\end{aligned} \tag{183}$$

And for the truncated Wigner we throw away all higher order interaction terms;

$$\begin{aligned}\partial_t \mathcal{W} = &\sum_j \left[\frac{\partial}{\partial x_j}\left(2J(y_{j+1}+y_{j-1}) - 2U(x_j^2 y_j + y_j^3) + \frac{\gamma_j}{2}x_j\right)\right]\mathcal{W} \\ &+ \sum_j \left[\frac{\partial}{\partial y_j}\left(-2J(x_{j+1}+x_{j-1}) + 2U(x_j y_j^2 + x_j^3) + \frac{\gamma_j}{2}y_j\right)\right]\mathcal{W} \\ &+ \frac{1}{2}\sum_j \gamma_j \left(\frac{\partial^2}{\partial x_j^2} + \frac{\partial^2}{\partial y_j^2}\right)\mathcal{W}\end{aligned} \tag{184}$$

This is our result.

D.3 Wigner function for a coherent state

Since the initial state is well characterized by a coherent state in each well we are interested in the Wigner function of this initial state. We start by calculating the scalar product for coherent states:

$$\begin{aligned}\langle\alpha|\psi\rangle &= \exp(-\frac{1}{2}|\alpha|^2)\exp(-\frac{1}{2}|\psi|^2)\sum_{nm}\frac{{\alpha^*}^n\psi^m}{\sqrt{n!}\sqrt{m!}}\langle n|m\rangle \\ &= \exp(-\frac{1}{2}|\alpha|^2)\exp(-\frac{1}{2}|\psi|^2)\sum_{nm}\frac{{\alpha^*}^n\psi^m}{\sqrt{n!}\sqrt{m!}}\delta_{nm} \\ &= \exp(-\frac{1}{2}|\alpha|^2)\exp(-\frac{1}{2}|\psi|^2)\sum_{n}\frac{\alpha^*\psi^n}{n!} \\ &= \exp(\alpha^*\psi - \frac{1}{2}|\alpha|^2 - \frac{1}{2}|\psi|^2).\end{aligned} \tag{185}$$

We apply the definition of the Wigner function;

$$\begin{aligned}
\mathcal{W} &= \frac{1}{\pi}\int d^2\beta \mathrm{e}^{(\alpha\beta^*-\alpha^*\beta)}\langle\alpha-\frac{\beta}{2}|\psi\rangle\langle\psi|\alpha+\frac{\beta}{2}\rangle \\
&= \frac{1}{\pi}\int d^2\beta \mathrm{e}^{(\alpha\beta^*-\alpha^*\beta)}\mathrm{e}^{((\alpha^*-\frac{\beta}{2}^*)\psi-\frac{1}{2}|\alpha-\frac{\beta}{2}|^2-\frac{1}{2}|\psi|^2)}\exp^{((\alpha+\frac{\beta}{2})\psi^*-\frac{1}{2}|\alpha+\frac{\beta}{2}|^2-\frac{1}{2}|\psi|^2)} \\
&= \frac{1}{\pi}\int d^2\beta \mathrm{e}^{(\alpha\beta^*-\alpha^*\beta)}\mathrm{e}^{(\alpha^*\psi+\alpha\psi^*-\frac{1}{2}\beta^*\psi+\frac{1}{2}\beta\psi^*-\alpha\alpha^*-\frac{1}{4}\beta\beta^*-|\psi|^2)} \\
&= \frac{1}{\pi}\mathrm{e}^{(\alpha^*\psi+\alpha\psi^*-\alpha\alpha^*-|\psi|^2)}\int d^2\beta \mathrm{e}^{\alpha\beta^*-\alpha^*\beta-\frac{1}{2}\beta^*\psi+\frac{1}{2}\beta\psi^*-\frac{1}{4}\beta\beta^*)} \\
&= \frac{1}{\pi}\mathrm{e}^{(-|\alpha-\psi|^2)}\int d^2\beta \mathrm{e}^{((\alpha-\psi)\beta^*-(\alpha-\psi)^*\beta-\beta\beta^*)} \\
&= \frac{1}{\pi}\mathrm{e}^{(-2|\alpha-\psi|^2)}\int d^2\beta \mathrm{e}^{(|\alpha-\psi|^2+(\alpha-\psi)\beta^*-(\alpha-\psi)^*\beta-\beta\beta^*)} \\
&= \frac{1}{\pi}\mathrm{e}^{(-2|\alpha-\psi|^2)}\int d^2\beta \mathrm{e}^{((\alpha-\psi-\beta)(\alpha-\psi+\beta)^*)} = \frac{2}{\pi}\mathrm{e}^{(-2|\alpha-\psi|^2)},
\end{aligned} \tag{186}$$

which is our result.

E Chapter 2 - Comparison to literature

In Sec. 3.6 we have observed deviations from our result for the dynamical equation of the truncated Wigner function, compared to the ones presented in Ref. [7]. We were able to trace these differences back to the usage of wrong operator correspondence which itself has been copied from [14]. Also the equations from [7] show inconsistencies, such as a global shift in energy and wrong factors upfront the noise terms, even under consideration of the wrong operator correspondences. The details in the calculations supporting these statements are presented in the following section of the Appendix material.

E.1 Rewriting the Wigner function in momentum state basis

To show that the operator correspondences from [14] are in fact not accurate, we follow the line of argument presented in this piece of literature. Therefore we need the expression of the Wigner function in the basis of x and p. The Wigner function expanded in the basis of x is well known. We execute a change of basis so we also have the expansion of the basis in p.

$$\begin{aligned}
W(x,p) &= \frac{1}{\pi\hbar}\int dy\langle x+y|\rho|x-y\rangle\exp(-2iyp/\hbar) \\
&= \frac{1}{\pi\hbar}\int\int\int dy\ d\bar{p}\ d\tilde{p}\langle x+y|\bar{p}\rangle\langle\bar{p}|\rho|\tilde{p}\rangle\langle\tilde{p}|x-y\rangle\exp(-2iyp/\hbar)
\end{aligned} \tag{187}$$

We use $\langle x|p\rangle = \sqrt{h}\exp(iyp/\hbar)$ and $\int dy\exp(iyp/\hbar) = h\delta(p)$. Thus we can perform the integration over y;

$$W(x,p) = \frac{1}{\pi\hbar}\int\int\ d\bar{p}\ d\tilde{p}\ \langle\bar{p}|\rho|\tilde{p}\rangle\delta(\bar{p}+\tilde{p}-2p)\exp(-ix(\bar{p}-\tilde{p})/\hbar) \tag{188}$$

We may substitute $a = \frac{1}{2}(\bar{p} + \tilde{p})$ and $b = \frac{1}{2}(\bar{p} - \tilde{p})$ and $d\bar{p}\ d\tilde{p} = da\ db$.

$$\begin{aligned} W(x,p) &= \frac{1}{\pi\hbar}\int\int\ da\ db\ \langle a+b|\rho|a-b\rangle\delta(2a-2p)\exp(-2ixb/\hbar) \\ &= \frac{1}{\pi\hbar}\int\int db\ \langle p+b|\rho|p-b\rangle\exp(-2ixb/\hbar) \end{aligned} \tag{189}$$

Which is the Wigner function expanded in the momentum state basis.

E.2 Operator correspondence in x and p

With our expansions of the Wigner function both in the basis of x and in the basis of p we can calculate the operator correspondences within this representation.

For the Wigner function expanded in the x-basis vectors we find the following:

$$\begin{aligned} \left(x + \frac{i\hbar}{2}\frac{\partial}{\partial p}\right) W(x,p) &= \frac{1}{\pi\hbar}\int dy \left(x + \frac{i\hbar}{2}\frac{\partial}{\partial p}\right)\langle x+y|\rho|x-y\rangle\exp(-2iyp/\hbar) \\ &= \frac{1}{\pi\hbar}\int dy \left(x + \frac{i\hbar}{2}\cdot\frac{-2iy}{\hbar}\right)\langle x+y|\rho|x-y\rangle\exp(-2iyp/\hbar) \\ &= \frac{1}{\pi\hbar}\int dy\,(x+y)\,\langle x+y|\rho|x-y\rangle\exp(-2iyp/\hbar) \\ &= \frac{1}{\pi\hbar}\int dy\langle x+y|\hat{x}\rho|x-y\rangle\exp(-2iyp/\hbar) \end{aligned} \tag{190}$$

$$\Rightarrow \left(x + \frac{i\hbar}{2}\frac{\partial}{\partial p}\right) W(x,p) \longleftrightarrow \hat{x}\rho \tag{191}$$

$$\begin{aligned} \left(x - \frac{i\hbar}{2}\frac{\partial}{\partial p}\right) W(x,p) &= \frac{1}{\pi\hbar}\int dy \left(x - \frac{i\hbar}{2}\frac{\partial}{\partial p}\right)\langle x+y|\rho|x-y\rangle\exp(-2iyp/\hbar) \\ &= \frac{1}{\pi\hbar}\int dy \left(x - \frac{i\hbar}{2}\cdot\frac{-2iy}{\hbar}\right)\langle x+y|\rho|x-y\rangle\exp(-2iyp/\hbar) \\ &= \frac{1}{\pi\hbar}\int dy\,(x-y)\,\langle x+y|\rho|x-y\rangle\exp(-2iyp/\hbar) \\ &= \frac{1}{\pi\hbar}\int dy\langle x+y|\rho\hat{x}|x-y\rangle\exp(-2iyp/\hbar) \end{aligned} \tag{192}$$

$$\Rightarrow \left(x - \frac{i\hbar}{2}\frac{\partial}{\partial p}\right) W(x,p) \longleftrightarrow \rho\hat{x}. \tag{193}$$

For the Wigner function expanded in the p-basis vectors we find the following:

$$\left(p - \frac{i\hbar}{2}\frac{\partial}{\partial x}\right) W(x,p) = \frac{1}{\pi\hbar}\int dy \left(p - \frac{i\hbar}{2}\frac{\partial}{\partial x}\right) \langle p+y|\rho|p-y\rangle \exp(-2iyx/\hbar)$$

$$= \frac{1}{\pi\hbar}\int dy \left(p - \frac{i\hbar}{2}\cdot\frac{-2iy}{\hbar}\right) \langle p+y|\rho|p-y\rangle \exp(-2iyx/\hbar) \tag{194}$$

$$= \frac{1}{\pi\hbar}\int dy \,(p+y) \,\langle p+y|\rho|p-y\rangle \exp(-2iyx/\hbar)$$

$$= \frac{1}{\pi\hbar}\int dy \langle p+y|\hat{p}\rho|p-y\rangle \exp(-2iyx/\hbar)$$

$$\Rightarrow \left(p - \frac{i\hbar}{2}\frac{\partial}{\partial x}\right) W(x,p) \longleftrightarrow \hat{p}\rho \tag{195}$$

$$\left(p + \frac{i\hbar}{2}\frac{\partial}{\partial x}\right) W(x,p) = \frac{1}{\pi\hbar}\int dy \left(p + \frac{i\hbar}{2}\frac{\partial}{\partial x}\right) \langle p+y|\rho|p-y\rangle \exp(-2iyx/\hbar)$$

$$= \frac{1}{\pi\hbar}\int dy \left(p + \frac{i\hbar}{2}\cdot\frac{-2iy}{\hbar}\right) \langle p+y|\rho|p-y\rangle \exp(-2iyx/\hbar) \tag{196}$$

$$= \frac{1}{\pi\hbar}\int dy \,(p-y) \,\langle p+y|\rho|p-y\rangle \exp(-2iyx/\hbar)$$

$$= \frac{1}{\pi\hbar}\int dy \langle p+y|\rho\hat{p}|p-y\rangle \exp(-2iyx/\hbar)$$

$$\Rightarrow \left(p + \frac{i\hbar}{2}\frac{\partial}{\partial x}\right) W(x,p) \longleftrightarrow \rho\hat{p} \tag{197}$$

The operator correspondences in the coherent state bais easily follow the relation between x, p and α, α^*, presented in [14].

E.3 Energy Shift in the Wigner function assuming wrong operator correspondences

We are showing that the term missing in our results when compared to the results from [7] can be indeed attributed to a global shift in energy. Therefore we explicitly calculate the time evolution of the chemical potential in the formulation of the phase space method.

Since we aim to understand the term presented in [7] we also use the incorrect operator correspondences from [14] used in this article. We translate the time evolution of the chemical potential term using these operator correspondences:

$$[\mathcal{H}_{\text{chem}}, \hat{\rho}(t)] = -\mu \sum_j (\hat{a}_j^\dagger \hat{a}\rho - \rho \hat{a}_j^\dagger \hat{a})$$

$$\leftrightarrow -\mu \sum_j \left(\left(\alpha_j^* - \frac{1}{2}\frac{\partial}{\partial \alpha_j}\right)\left(\alpha_j + \frac{1}{2}\frac{\partial}{\partial \alpha_j^*}\right) - \left(\alpha_j^* + \frac{1}{2}\frac{\partial}{\partial \alpha_j}\right)\left(\alpha_j - \frac{1}{2}\frac{\partial}{\partial \alpha_j^*}\right)\right) \mathcal{W}. \tag{198}$$

Again we split α and α^* into real and imaginary part and find:

$$\begin{aligned}\left(\alpha_j^* - \frac{1}{2}\frac{\partial}{\partial\alpha_j}\right)\left(\alpha_j + \frac{1}{2}\frac{\partial}{\partial\alpha_j^*}\right) &= \left(x_j - iy_j - \frac{1}{4}\frac{\partial}{\partial x_j} + i\frac{1}{4}\frac{\partial}{\partial y_j}\right)\left(x_j + iy_j + \frac{1}{4}\frac{\partial}{\partial x_j} + i\frac{1}{4}\frac{\partial}{\partial y_j}\right)\\ &= x_j^2 + ix_jy_j - ix_jy_j + y_j^2 + \frac{x_j}{4}\frac{\partial}{\partial x_j} + i\frac{x_j}{4}\frac{\partial}{\partial y_j} - i\frac{y_j}{4}\frac{\partial}{\partial x_j} + \frac{y_j}{4}\frac{\partial}{\partial y_j} - \frac{x_j}{4}\frac{\partial}{\partial x_j}\\ &+ i\frac{x_j}{4}\frac{\partial}{\partial y_j} - i\frac{y_j}{4}\frac{\partial}{\partial x_j} - \frac{y_j}{4}\frac{\partial}{\partial y_j} - \frac{1}{16}\frac{\partial^2}{\partial x_j^2} - i\frac{1}{16}\frac{\partial}{\partial x_j}\frac{\partial}{\partial y_j} + i\frac{1}{16}\frac{\partial}{\partial x_j}\frac{\partial}{\partial y_j} - \frac{1}{16}\frac{\partial}{\partial y_j^2}\\ &= x_j^2 + y_j^2 + ix_j\frac{1}{2}\frac{\partial}{\partial y_j} - iy_j\frac{1}{2}\frac{\partial}{\partial x_j} - \frac{1}{16}\frac{\partial^2}{\partial x_j^2} - \frac{1}{16}\frac{\partial}{\partial y_j^2}.\end{aligned} \tag{199}$$

And also:

$$\begin{aligned}\left(\alpha_j^* + \frac{1}{2}\frac{\partial}{\partial\alpha_j}\right)\left(\alpha_j - \frac{1}{2}\frac{\partial}{\partial\alpha_j^*}\right) &= \left(x_j - iy_j + \frac{1}{4}\frac{\partial}{\partial x_j} - i\frac{1}{4}\frac{\partial}{\partial y_j}\right)\left(x_j + iy_j - \frac{1}{4}\frac{\partial}{\partial x_j} - i\frac{1}{4}\frac{\partial}{\partial y_j}\right)\\ &= x_j^2 + ix_jy_j + ix_jy_j + y_j^2 - \frac{x_j}{4}\frac{\partial}{\partial x_j} - i\frac{x_j}{4}\frac{\partial}{\partial y_j} + i\frac{y_j}{4}\frac{\partial}{\partial x_j} - \frac{y_j}{4}\frac{\partial}{\partial y_j} + \frac{x_j}{4}\frac{\partial}{\partial x_j}\\ &- i\frac{x_j}{4}\frac{\partial}{\partial y_j} + i\frac{y_j}{4}\frac{\partial}{\partial x_j} + \frac{y_j}{4}\frac{\partial}{\partial y_j} - \frac{1}{16}\frac{\partial^2}{\partial x_j^2} - i\frac{1}{16}\frac{\partial}{\partial x_j}\frac{\partial}{\partial y_j} + i\frac{1}{16}\frac{\partial}{\partial x_j}\frac{\partial}{\partial y_j} - \frac{1}{16}\frac{\partial}{\partial y_j^2}\\ &= x_j^2 + y_j^2 - ix_j\frac{1}{2}\frac{\partial}{\partial y_j} + iy_j\frac{1}{2}\frac{\partial}{\partial x_j} - \frac{1}{16}\frac{\partial^2}{\partial x_j^2} - \frac{1}{16}\frac{\partial}{\partial y_j^2}.\end{aligned} \tag{200}$$

Combined we find the following result:

$$\begin{aligned}-i[\mathcal{H}_{\text{chem}}, \hat{\rho}(t)] &= -i\mu\sum_j\left(\left(x_j^2 + y_j^2 + ix_j\frac{1}{2}\frac{\partial}{\partial y_j} - iy_j\frac{1}{2}\frac{\partial}{\partial x_j} - \frac{1}{16}\frac{\partial^2}{\partial x_j^2} - \frac{1}{16}\frac{\partial}{\partial y_j^2}\right)\right.\\ &\left. - \left(x_j^2 + y_j^2 - ix_j\frac{1}{2}\frac{\partial}{\partial y_j} + iy_j\frac{1}{2}\frac{\partial}{\partial x_j} - \frac{1}{16}\frac{\partial^2}{\partial x_j^2} - \frac{1}{16}\frac{\partial}{\partial y_j^2}\right)\right)\mathcal{W}\\ &= \mu\sum_j\left(x_j\frac{\partial}{\partial y_j} - y_j\frac{\partial}{\partial x_j}\right)\mathcal{W},\end{aligned} \tag{201}$$

which is exactly the missing term, thus proving our statement.

E.4 Computation of the decay term assuming wrong operator correspondences

Since we stated that the decay terms presented in [7] include wrong prefactors, hiding the usage of wrong operator correspondences and therefore partially compensating for the errors made by the wrong correspondences, we explicitly calculate the decay term under the assumptions made in [7].

For the decay term we find:

$$
\begin{aligned}
\text{DECAY} = -\sum_j \frac{\gamma_j}{2} \Bigg[& \left(\alpha_j^* - \frac{1}{2}\frac{\partial}{\partial \alpha_j}\right)\left(\alpha_j + \frac{1}{2}\frac{\partial}{\partial \alpha_j^*}\right) + \left(\alpha_j^* + \frac{1}{2}\frac{\partial}{\partial \alpha_j}\right)\left(\alpha_j - \frac{1}{2}\frac{\partial}{\partial \alpha_j^*}\right) \\
& -2\left(\alpha_j + \frac{1}{2}\frac{\partial}{\partial \alpha_j^*}\right)\left(\alpha_j^* + \frac{1}{2}\frac{\partial}{\partial \alpha_j}\right)\Bigg] \mathcal{W} \\
= -\sum_j \frac{\gamma_j}{2} \Bigg[& \left(x_j - iy_j - \frac{1}{4}\frac{\partial}{\partial x_j} + i\frac{1}{4}\frac{\partial}{\partial y_j}\right)\left(x_j + iy_j + \frac{1}{4}\frac{\partial}{\partial x_j} + i\frac{1}{4}\frac{\partial}{\partial y_j}\right) \\
& + \left(x_j - iy_j + \frac{1}{4}\frac{\partial}{\partial x_j} - i\frac{1}{4}\frac{\partial}{\partial y_j}\right)\left(x_j + iy_j - \frac{1}{4}\frac{\partial}{\partial x_j} - i\frac{1}{4}\frac{\partial}{\partial y_j}\right) \\
& -2\left(x_j + iy_j + \frac{1}{4}\frac{\partial}{\partial x_j} + i\frac{1}{4}\frac{\partial}{\partial y_j}\right)\left(x_j - iy_j + \frac{1}{4}\frac{\partial}{\partial x_j} - i\frac{1}{4}\frac{\partial}{\partial y_j}\right)\Bigg] \mathcal{W} \\
= -\sum_j \frac{\gamma_j}{2} \Bigg[& \left(x_j^2 + y_j^2 + ix_j\frac{1}{4}\frac{\partial}{\partial y_j} - iy_j\frac{1}{4}\frac{\partial}{\partial x_j} - \frac{1}{16}\frac{\partial^2}{\partial x_j^2} - \frac{1}{16}\frac{\partial^2}{\partial y_j^2}\right) \\
& + \left(x_j^2 + y_j^2 - ix_j\frac{1}{4}\frac{\partial}{\partial y_j} + iy_j\frac{1}{4}\frac{\partial}{\partial x_j} - \frac{1}{16}\frac{\partial^2}{\partial x_j^2} - \frac{1}{16}\frac{\partial^2}{\partial y_j^2}\right) \\
& -2\left(x_j^2 + y_j^2 + x_j\frac{1}{4}\frac{\partial}{\partial x_j} + y_j\frac{1}{4}\frac{\partial}{\partial y_j} + \frac{1}{16}\frac{\partial^2}{\partial x_j^2} + \frac{1}{16}\frac{\partial^2}{\partial y_j^2}\right)\Bigg] \mathcal{W} \\
= \frac{1}{2}\sum_j \frac{\gamma_j}{4} & \left(2x_j\frac{\partial}{\partial x_j} + 2y_j\frac{\partial}{\partial y_j} + \frac{\partial^2}{\partial x_j^2} + \frac{\partial^2}{\partial y_j^2}\right)\mathcal{W},
\end{aligned}
\tag{202}
$$

which supports our statement in direct comparison.

F Chapter 2 - Failed attempts to reduce complexity to second order

We are challenged to consider the third-order terms from Eq. (76) in our approach. We could try to solve the equations directly. However, we are interested in taking advantage of the numerical feasibility inherent to the truncated Wigner approach. Thus we are challenged to approximate our equations in a way that they only produce second-order differential equations. We tried several more or less naive ideas to do so, always aware that they were technically wrong, however in the hope that we could motivate terms in our equations that cause some improvement. These attempts have failed. We present them as negative results, motivating a more nuanced method on how to incorporate the truncated terms into our framework of stochastic equations Eq. (84) and Eq. (85).

F.1 First attempt

We employ a methodology analogous to the one described in Sec. 3.5.2, wherein the equation of motion for the Wigner function is mapped onto the Fokker-Planck equation, which is subsequently mapped onto

the Langevin equation. A notable challenge arises when attempting to extend the Feynman-Kac formula to accommodate third-order derivatives, necessitating the approximation of these derivatives to second-order terms in a manner that retains physical relevance. The simplest possible approach is to represent one of the derivatives with respect to x_j and y_j as follows:

$$\frac{\partial}{\partial x_j} \approx \frac{x_{j+1} - x_{j-1}}{2}, \tag{203}$$

$$\frac{\partial}{\partial y_j} \approx \frac{y_{j+1} - y_{j-1}}{2}. \tag{204}$$

This is surely wrong. However, these approximations allow for the reduction of third-order derivatives to second-order terms, opening a route for our method in the framework of the Fokker-Planck and Langevin equations. This is enabling the effective mapping of third-order terms to their second-order counterparts, offering a simplified yet insightful exploration of the system's dynamics. Our approximation strategy yields two options, preserving the symmetries of the original equation concerning x_j and y_j, because we can either replace $\partial/\partial x_j$ or $\partial/\partial y_j$;

$$\mathcal{A} = U \sum_j \left[y_j \frac{x_{j+1} - x_{j-1}}{2} \left(\frac{\partial^2}{\partial x_j^2} + 3\frac{\partial^2}{\partial y_j^2} \right) - x_j \frac{y_{j+1} - y_{j-1}}{2} \left(\frac{\partial^2}{\partial y_j^2} + 3\frac{\partial^2}{\partial x_j^2} \right) \right] \mathcal{W}$$

$$\frac{U}{2} = \sum_j \left[\frac{\partial^2}{\partial x_j^2} y_j(x_{j+1} - x_{j-1}) - 3x_j(y_{j+1} - y_{j-1}) + \frac{\partial^2}{\partial y_j^2} 3y_j(x_{j+1} - x_{j-1}) - x_j(y_{j+1} - y_{j-1}) + \right] \mathcal{W}$$

$$= \sum_j \frac{U}{2} \begin{pmatrix} \frac{\partial^2}{\partial x_j^2} \left[y_j(x_{j+1} - x_{j-1}) - 3x_j(y_{j+1} - y_{j-1}) \right]^{1/2} & 0 \\ 0 & \frac{\partial^2}{\partial x_j^2} \left[3y_j(x_{j+1} - x_{j-1}) - x_j(y_{j+1} - y_{j-1}) \right]^{1/2} \end{pmatrix}^2 \mathcal{W} \tag{205}$$

$$\mathcal{B} = U \sum_j \left[y_j \left(\frac{x_{j+1} - x_{j-1}}{2} \frac{\partial^2}{\partial x_j^2} + 3\frac{y_{j+1} - y_{j-1}}{2} \frac{\partial}{\partial x_j} \frac{\partial}{\partial y_j} \right) - x_j \left(\frac{y_{j+1} - y_{j-1}}{2} \frac{\partial^2}{\partial y_j^2} + 3\frac{x_{j+1} - x_{j-1}}{2} \frac{\partial}{\partial x_j} \frac{\partial}{\partial y_j} \right) \right] \mathcal{W}$$

$$= \frac{U}{2} \sum_j \left[y_j(x_{j+1} - x_{j-1}) \frac{\partial^2}{\partial x_j^2} + 3y_j(y_{j+1} - y_{j-1}) \frac{\partial}{\partial x_j} \frac{\partial}{\partial y_j} \right.$$

$$\left. -x_j(y_{j+1} - y_{j-1}) \frac{\partial^2}{\partial y_j^2} + 3x_j(x_{j+1} - x_{j-1}) \frac{\partial}{\partial x_j} \frac{\partial}{\partial y_j} \right] \mathcal{W} \tag{206}$$

Regarding the term $\mathcal{B}$, we observe two critical aspects:

(i) The equation includes terms with mixed derivatives, which, when translated into a diffusion matrix, manifest as off-diagonal entries. This characteristic suggests the presence of coupling between different degrees of freedom in the system, indicative of correlated diffusion processes.

(ii) It is infeasible to directly map this term onto a Fokker-Planck equation in the conventional form with a diffusion matrix of the shape $\hat{B}\hat{B}^T$. The unequal off-diagonal elements in the diffusion matrix (inherent in the mixed derivatives terms) forbid a straightforward representation as a product of a matrix and its transpose. Consequently, this term may be interpreted as an analogue to asymmetric diffusion, a phenomenon where the diffusion rate varies in an anisotropic manner across different axes.

Given the challenges in mapping term $\mathcal{B}$ onto a standard Fokker-Planck framework due to its asymmetric diffusion characteristics, our analysis proceeds by focusing on equation $\mathcal{A}$. This decision is predicated on the assumption that $\mathcal{A}$ offers a more tractable foundation for exploring the dynamics at hand without the complexities introduced by the mixed derivative terms found in $\mathcal{B}$.

In this context we uncover the following description in terms of the Fokker-Planck formulation:

$$\vec{z_j} = (x_j, y_j)^T \tag{207}$$

$$\vec{A_j}(t) = \begin{pmatrix} 2J(y_{j+1} + y_{j-1}) - 2U(x_j^2 y_j + y_j^3) + \frac{\gamma_j}{2} x_j \\ -2J(x_{j+1} + x_{j-1}) + 2U(x_j y_j^2 + x_j^3) + \frac{\gamma_j}{2} y_j \end{pmatrix} \tag{208}$$

$B_j(\vec{z}, t) = \gamma_j \mathbf{1}$

$$+ \frac{\sqrt{U}}{\sqrt{2}} \begin{pmatrix} [y_j(x_{j+1} - x_{j-1}) - 3x_j(y_{j+1} - y_{j-1})]^{1/2} & 0 \\ 0 & [3y_j(x_{j+1} - x_{j-1}) - x_j(y_{j+1} - y_{j-1}))]^{1/2} \end{pmatrix} \tag{209}$$

Again we apply the Feynman-Kacs equation;

$$\frac{d\vec{z}}{dt} = \vec{A}(\vec{z}, t) + B(\vec{z}, t)\vec{E}(t) \tag{210}$$

Then we find;

$$\frac{dx_j}{dt} = -2J(y_{j+1} + y_{j-1}) + 2U(x_j^2 y_j + y_j^3) - \frac{\gamma_j}{2} x_j + \left[\sqrt{\gamma_j} + \frac{\sqrt{U}}{\sqrt{2}} \left(y_j(x_{j+1} - x_{j-1}) - 3x_j(y_{j+1} - y_{j-1}) \right)^{1/2} \right] \zeta_j \tag{211}$$

$$\frac{dy_j}{dt} = 2J(x_{j+1} + x_{j-1}) - 2U(x_j y_j^2 + x_j^3) - \frac{\gamma_j}{2} x_j + \left[\sqrt{\gamma_j} + \frac{\sqrt{U}}{\sqrt{2}} \left(3y_j(x_{j+1} - x_{j-1}) - x_j(y_{j+1} - y_{j-1}) \right)^{1/2} \right] \eta_j \tag{212}$$

Consequently, our analysis resolves to the formulation of a Langevin equation, wherein the random force is influenced not only by the decay rate, as previously noted, but also by both the real and imaginary components of the amplitude within the local wells. This is all good but surely must be tested against reality. We present two parameter regimes, one of strong coupling ($U = 0.4J$) and one of weaker coupling ($U = 0.1J$) and observe if the results get better or worse with our correction term, compared to the truncated Wigner equations without. In Fig. 16 we see that the results are numerically unstable. This is hardly surprising, as our equations do not exclude the possibility of negative values under the square-root term. Also, experiments with modified versions of these equations have failed. It seems like there are some fundamental issues with symmetry breaking in these equations.

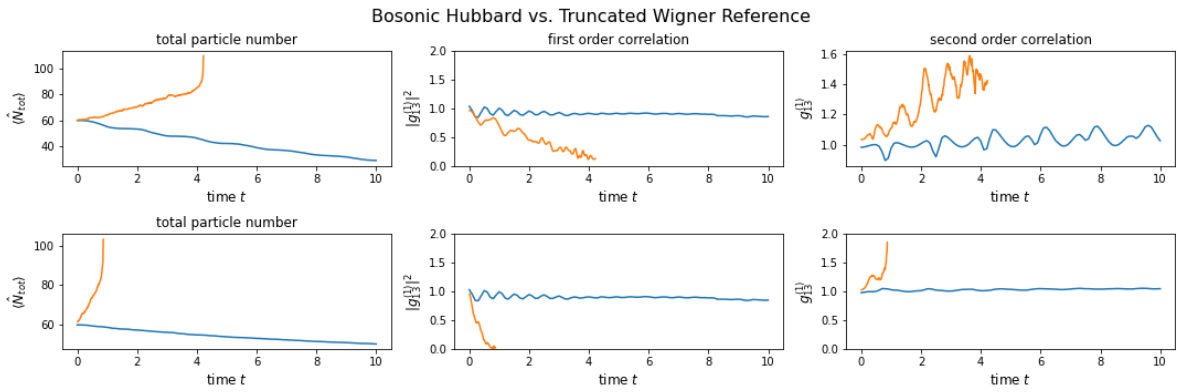

Figure 16: We present a negative result that shows the observables, calculated with Eq. (211) and Eq. (212). The results are divergent. The blue lines represent the Bose-Hubbard simulations. The yellow lines represent the Wigner simulations with the additional correction term. The upper row corresponds to week on-site energy $U = 0.1J$ and the lower row corresponds to strong on-site energy $U = 0.4J$.

F.2 Second attempt

One may rightfully attribute earlier failed attempts to the highly naive reduction from third order to lower order. We have also tried a more subtle variant where we approximated the third order by a Taylor expansion;

$$\frac{\partial^3 f(x)}{\partial^3 x} \approx \frac{6}{x_0^3}\left[f(x+x_0) - f(x) - \frac{\partial f(x)}{\partial x}x_0^2 - \frac{\partial^3 f(x)}{\partial^3 x}\frac{x_0}{2}\right] \tag{213}$$

$$\frac{\partial 2 f(x)}{\partial^2 x} \approx \frac{2}{x_0^2}\left[f(x+x_0) - f(x) - \frac{\partial f(x)}{\partial x}x_0\right] \tag{214}$$

Where we used Eq. (213) for the pure third order derivatives and Eq. (214) for the mixed order derivatives. In our context, $f(x)$ is the Wigner function. It is strictly speaking not possible to map the resulting equations on a Fokker-Planck equation of the form used above. Also, new versions of stochastic equations Eq. (84) and Eq. (85) inspired by the results when inserting Eq. (213) and Eq. (214) in the third order term of Eq. (76) produced unsuccessful results. In contrast to the earlier attempt the result was not completely divergent. It became numerically divergent, either for large U/J, or for small x_0. Also, any meta-stable results were worse than without the correction term. In other words, the equations were not convincing. We have also tried several different experimental additional terms, with the idea that we simply add noise terms that preserve the symmetries of the third order term, such as $\mathcal{F}(x,y) = -\mathcal{F}(y,x)$. Other attempts went in the direction of adding correlated noise instead of white noise. We learned that any attempt to include the higher-order terms of the Wigner function in our stochastic equations needs a more meaningful foundation.

References

[1] N. Bolik and S. Wimberger. Spontaneous-emission-induced ratchet in atom-optics kicked-rotor quantum walks. *Phys. Rev. A*, 109:063307, Jun 2024.

[2] C. Groiseau, A. Gresch, and S. Wimberger. Quantum walks of kicked Bose–Einstein condensates. *Journal of Physics A: Mathematical and Theoretical*, 51(27):275301, Jun 2018.

[3] S. Wimberger, I. Guarneri, and S. Fishman. Quantum resonances and decoherence for δ-kicked atoms. *Nonlinearity*, 16(4):1381, May 2003.

[4] N. Bolik. Topological phases and symmetries in 1d quantum walks. Bachelor Thesis, University of Heidelberg, 2022.

[5] D. Witthaut, F. Trimborn, H. Hennig, G. Kordas, T. Geisel, and S. Wimberger. Beyond mean-field dynamics in open Bose-Hubbard chains. *Physical Review A*, 83(6), June 2011.

[6] G. Kordas, S. Wimberger, and D. Witthaut. Dissipation-induced macroscopic entanglement in an open optical lattice. *Europhysics Letters*, 100(3):30007, Nov 2012.

[7] G. Kordas, S. Wimberger, and D. Witthaut. Decay and fragmentation in an open Bose-Hubbard chain. *Phys. Rev. A*, 87:043618, Apr 2013.

[8] N. Bolik, C. Groiseau, J. H. Clark, G. S. Summy, Y. Liu, and S. Wimberger. Detecting topological phase transitions in a double kicked quantum rotor. *Phys. Rev. A*, 106:043318, Oct 2022.

[9] N. Bolik, C. Groiseau, J. H. Clark, A. Gresch, S. Dadras, G. S. Summy, Y. Liu, and S. Wimberger. Light-shift-induced behaviors observed in momentum-space quantum walks. *Phys. Rev. A*, 106:033307, Sep 2022.

[10] J. Kempe. Quantum random walks: An introductory overview. *Contemporary Physics*, 44(4):307–327, 2003.

[11] R. Portugal. *Quantum Walks and Search Algorithms*. Springer International Publishing, New York, 2018.

[12] N. B. Lovett, S. Cooper, M. Everitt, M. Trevers, and V. Kendon. Universal quantum computation using the discrete-time quantum walk. *Phys. Rev. A*, 81:042330, Apr 2010.

[13] M. A. Nielsen and I. L. Chuang. *Quantum Computation and Quantum Information*. Cambridge University Press, 2000.

[14] C. W. Gardiner and P. Zoller. *Quantum Noise*. Springer Berlin, Heidelberg, second edition, 2000.

[15] M. O. Scully and M. S. Zubairy. *Quantum optics*. Cambridge University Press, Cambridge, 1997.

[16] G. Trautmann, C. Groiseau, and S. Wimberger. Parrondo's paradox for discrete-time quantum walks in momentum space. *Fluctuation and Noise Letters*, 21(06):2250053, 2022.

[17] O. Morsch and M. Oberthaler. Dynamics of Bose-Einstein condensates in optical lattices. *Rev. Mod. Phys.*, 78:179–215, Feb 2006.

[18] I. Bloch, J. Dalibard, and W. Zwerger. Many-body physics with ultracold gases. *Rev. Mod. Phys.*, 80:885–964, Jul 2008.

[19] S. Dadras, A. Gresch, C. Groiseau, S. Wimberger, and G. S. Summy. Experimental realization of a momentum-space quantum walk. *Physical Review A*, 99(4):043617, 2019.

[20] S. Dadras, A. Gresch, C. Groiseau, S. Wimberger, and Gil S. Summy. Quantum walk in momentum space with a Bose-Einstein condensate. *Phys. Rev. Lett.*, 121:070402, Aug 2018.

[21] C. Groiseau. Discrete-time quantum walks in momentum space. Master's thesis, Heidelberg University, 2017.

[22] D. Witthaut, E. M. Graefe, S. Wimberger, and H. J. Korsch. Bose-Einstein condensates in accelerated double-periodic optical lattices: Coupling and crossing of resonances. *Physical Review A*, 75(1), January 2007.

[23] M. J. Werner and P. D. Drummond. Robust algorithms for solving stochastic partial differential equations. *Journal of Computational Physics*, 132(2):312–326, 1997.

[24] A. Sinatra, C. Lobo, and Y. Castin. The truncated Wigner method for Bose-condensed gases: limits of validity and applications. *Journal of Physics B: Atomic, Molecular and Optical Physics*, 35(17):3599–3631, August 2002.

[25] M. J. Steel, M. K. Olsen, L. I. Plimak, P. D. Drummond, S. M. Tan, M. J. Collett, D. F. Walls, and R. Graham. Dynamical quantum noise in trapped Bose-Einstein condensates. *Physical Review A*, 58(6):4824–4835, December 1998.

[26] J. Dujardin, A. Argüelles, and P. Schlagheck. Elastic and inelastic transmission in guided atom lasers: A truncated wigner approach. *Physical Review A*, 91(3), March 2015.

[27] A. Polkovnikov. Phase space representation of quantum dynamics. *Annals of Physics*, 325(8):1790–1852, August 2010.

[28] J. F. Sherson, C. Weitenberg, M. Endres, M. Cheneau, I. Bloch, and S. Kuhr. Single-atom-resolved fluorescence imaging of an atomic mott insulator. *Nature*, 467(7311):68–72, September 2010.

[29] W. S. Bakr, J. I. Gillen, A. Peng, S. Fölling, and M. Greiner. A quantum gas microscope for detecting single atoms in a hubbard-regime optical lattice. *Nature*, 462(7269):74–77, November 2009.

[30] M. Puchalski, D. Kędziera, and K. Pachucki. D1 and D2 lines in 6Li and 7Li including QED effects. *Physical Review A*, 87, 03 2013.

[31] G. Barontini, R. Labouvie, F. Stubenrauch, A. Vogler, V. Guarrera, and H. Ott. Controlling the dynamics of an open many-body quantum system with localized dissipation. *Phys. Rev. Lett.*, 110:035302, Jan 2013.

[32] C. Gross, T. Zibold, E. Nicklas, J. Estève, and M. K. Oberthaler. Nonlinear atom interferometer surpasses classical precision limit. *Nature*, 464(7292):1165–1169, March 2010.

[33] G. H. Weiss. *Aspects and Applications of the Random Walk*. North Holland, Amsterdam, 1994.

[34] A. D. Mirlin, Y. V. Fyodorov, F. M. Dittes, J. Quezada, and T. H. Seligman. Transition from localized to extended eigenstates in the ensemble of power-law random banded matrices. *Phys. Rev. E*, 54:3221–3230, Oct 1996.

[35] P. Olla. Return times for stochastic processes with power-law scaling. *Phys. Rev. E*, 76:011122, Jul 2007.

[36] P. M. Preiss, R. Ma, M. E. Tai, A. Lukin, M. Rispoli, P. Zupancic, Y. Lahini, R. Islam, and M. Greiner. Strongly correlated quantum walks in optical lattices. *Science*, 347(6227):1229–1233, 2015.

[37] W. Dür, R. Raussendorf, V. M. Kendon, and H. Briegel. Quantum walks in optical lattices. *Physical Review A*, 66(5):052319, 2002.

[38] K. Eckert, J. Mompart, G. Birkl, and Maciej L. One-and two-dimensional quantum walks in arrays of optical traps. *Physical Review A*, 72(1):012327, 2005.

[39] A. Steffen, A. Alberti, W. Alt, N. Belmechri, S. Hild, M. Karski, A. Widera, and D. Meschede. Digital atom interferometer with single particle control on a discretized space-time geometry. *Proceedings of the National Academy of Sciences*, 109(25):9770–9774, 2012.

[40] T. Groh, S. Brakhane, W. Alt, D. Meschede, J. K. Asbóth, and A. Alberti. Robustness of topologically protected edge states in quantum walk experiments with neutral atoms. *Physical Review A*, 94(1):013620, 2016.

[41] M. Karski, L. Förster, J. Choi, A. Steffen, W. Alt, D. Meschede, and A. Widera. Quantum walk in position space with single optically trapped atoms. *Science*, 325(5937):174–177, 2009.

[42] CM. Chandrashekar. Implementing the one-dimensional quantum (Hadamard) walk using a Bose-Einstein condensate. *Physical Review A*, 74(3):032307, 2006.

[43] B. C. Travaglione and G. J. Milburn. Implementing the quantum random walk. *Physical Review A*, 65(3):032310, 2002.

[44] F. Zähringer, G. Kirchmair, R. Gerritsma, E. Solano, R. Blatt, and C. Roos. Realization of a quantum walk with one and two trapped ions. *Phys. Rev. Lett.*, 104(10):100503, 2010.

[45] H. Schmitz, R. Matjeschk, C. Schneider, J. Glueckert, M. Enderlein, T. Huber, and T. Schaetz. Quantum walk of a trapped ion in phase space. *Phys. Rev. Lett.*, 103(9):090504, 2009.

[46] D. J. Wineland, C. Monroe, W. M. Itano, D. Leibfried, B. E. King, and D. M. Meekhof. Experimental issues in coherent quantum-state manipulation of trapped atomic ions. *Journal of Research of the National Institute of Standards and Technology*, 103(3):259, 1998.

[47] H. B. Perets, Y. Lahini, F. Pozzi, M. Sorel, R. Morandotti, and Y. Silberberg. Realization of quantum walks with negligible decoherence in waveguide lattices. *Phys. Rev. Lett.*, 100(17):170506, 2008.

[48] A. Peruzzo, M. Lobino, J. Matthews, N. Matsuda, A. Politi, K. Poulios, X Zhou, Y. Lahini, N. Ismail, K. Wörhoff, et al. Quantum walks of correlated photons. *Science*, 329(5998):1500–1503, 2010.

[49] F. Cardano, A. D'Errico, A. Dauphin, M. Maffei, B. Piccirillo, C. de Lisio, G. De Filippis, V. Cataudella, E. Santamato, L. Marrucci, et al. Detection of zak phases and topological invariants in a chiral quantum walk of twisted photons. *Nature Communications*, 8:15516, 2017.

[50] C. Chen, X. Ding, J. Qin, Y. He, Y. Luo, M. Chen, C. Liu, X. Wang, W. Zhang, H. Li, et al. Observation of topologically protected edge states in a photonic two-dimensional quantum walk. *Phys. Rev. Lett.*, 121(10):100502, 2018.

[51] H. Tang, X. Lin, Z. Feng, J. Chen, J. Gao, K. Sun, C. Wang, P. Lai, X. Xu, Y. Wang, et al. Experimental two-dimensional quantum walk on a photonic chip. *Sci. Adv.*, 4(5):eaat3174, 2018.

[52] K. Poulios, R. Keil, D. Fry, J. Meinecke, J. Matthews, A. Politi, M. Lobino, M. Gräfe, M. Heinrich, S. Nolte, et al. Quantum walks of correlated photon pairs in two-dimensional waveguide arrays. *Phys. Rev. Lett.*, 112(14):143604, 2014.

[53] A. Schreiber, K. N. Cassemiro, V. Potoček, A. Gábris, P. J. Mosley, E. Andersson, I. Jex, and C. Silberhorn. Photons walking the line: a quantum walk with adjustable coin operations. *Phys. Rev. Lett.*, 104(5):050502, 2010.

[54] V. M. Kendon. A random walk approach to quantum algorithms. *Philosophical Transactions of the Royal Society A: Mathematical, Physical and Engineering Sciences*, 364(1849):3407–3422, Oct 2006.

[55] J. H. Clark, C. Groiseau, Z. N. Shaw, S. Dadras, C. Binegar, S. Wimberger, G. S. Summy, and Y. Liu. Quantum to classical walk transitions tuned by spontaneous emissions. *Phys. Rev. Research*, 3:043062, Oct 2021.

[56] F. Schwabl. *Quantenmechanik (QM I): Eine Einführung*. Springer Berlin, Heidelberg, 2007.

[57] G. Summy and S. Wimberger. Quantum random walk of a Bose-Einstein condensate in momentum space. *Phys. Rev. A*, 93:023638, Feb 2016.

[58] *Excitation of molecular rotation by periodic microwave pulses. A testing ground for Anderson localization*, page 87–98. Cambridge University Press, 1995.

[59] A. L. Wagner. Topology in 1d quantum walks, Bachelor thesis, Heidelberg University 2018. [`https://www.thphys.uni-heidelberg.de/~wimberger/theses.html`].

[60] M. Raizen. Quantum chaos with cold atoms. *Advances in Atomic, Molecular, and Optical Physics*, 41(43):199, 1999.

[61] M. Sadgrove and S. Wimberger. A pseudo-classical method for the atom-optics kicked rotor: from theory to experiment and back. *Adv. At. Mol. Opt. Phys.*, 60:315, 2011.

[62] M. Delvecchio, F. Petiziol, and S. Wimberger. Resonant quantum kicked rotor as a continuous-time quantum walk. *Condensed Matter*, 5(1):4, 2020.

[63] J. Ni, W. K. Lam, S. Dadras, M. F. Borunda, S. Wimberger, and G. S. Summy. Initial-state dependence of a quantum resonance ratchet. *Phys. Rev. A*, 94:043620, Oct 2016.

[64] J. Ni, W. K. Lam, S. Dadras, M. Borunda, S. Wimberger, and G. S. Summy. Initial-state dependence of a quantum resonance ratchet. *Physical Review A*, 94(4):043620, 2016.

[65] S. Schlunk, M. B. d'Arcy, S. A. Gardiner, D. Cassettari, R. M. Godun, and G. S. Summy. Signatures of quantum stability in a classically chaotic system. *Phys. Rev. Lett.*, 90:054101, Feb 2003.

[66] S. Chai and M. F. Andersen. Enhancing survival resonances with engineered dissipation. *Phys. Rev. Res.*, 2:033194, Aug 2020.

[67] M. F. Andersen and S. Wimberger. Classical model for survival resonances close to the Talbot time. *Phys. Rev. A*, 105:013322, Jan 2022.

[68] C. Groiseau and S. Wimberger. Spontaneous emission in quantum walks of a kicked Bose-Einstein condensate. *Phys. Rev. A*, 99:013610, Jan 2019.

[69] S. Wimberger. Applications of fidelity measures to complex quantum systems. *Phil. Trans. Royal Soc. A (London)*, 374:20150153, Jun 2016.

[70] R. Sajjad, J. L. Tanlimco, H. Mas, A. Cao, E. Nolasco-Martinez, E. Q. Simmons, F. L. N. Santos, P. Vignolo, T. Macrì, and D. M. Weld. Observation of the quantum boomerang effect. *Phys. Rev. X*, 12:011035, Feb 2022.

[71] J. H. S. Toh, K. C. McCormick, X. Tang, Y. Su, XW. Luo, C. Zhang, and S. Gupta. Observation of many-body dynamical delocalization in a kicked ultracold gas, 2021. arXiv 2106.13773.

[72] D. A. Steck. Sodium D line data. *https://steck.us/alkalidata/*, 1998.

[73] S. Dadras, A. Gresch, C. Groiseau, S. Wimberger, and G. S. Summy. Experimental realization of a momentum-space quantum walk. *Phys. Rev. A*, 99:043617, Apr 2019.

[74] L. Deng, E. W. Hagley, J. Denschlag, J. E. Simsarian, M. Edwards, C. W. Clark, K. Helmerson, S. L. Rolston, and W. D. Phillips. Temporal, matter-wave-dispersion talbot effect. *Phys. Rev. Lett.*, 83:5407–5411, Dec 1999.

[75] Y. Liu, 2022. private communication.

[76] K. Singh. Floquet engineering with ultracold lithium in optical lattices. *UC Santa Barbara*, 2019. https://escholarship.org/uc/item/2k34w3cz.

[77] C. Ryu, M. F. Andersen, A. Vaziri, M. B. d'Arcy, J. M. Grossman, K. Helmerson, and W. D. Phillips. High-order quantum resonances observed in a periodically kicked Bose-Einstein condensate. *Phys. Rev. Lett.*, 96:160403, Apr 2006.

[78] S. Chakraborty, A. Das, A. Mallick, and C. M. Chandrashekar. Quantum ratchet in disordered quantum walk. *Annalen der Physik*, 529(8):1600346, 2017.

[79] F. L. Moore, J. C. Robinson, C. F. Bharucha, Bala Sundaram, and M. G. Raizen. Atom optics realization of the quantum δ-kicked rotor. *Phys. Rev. Lett.*, 75:4598–4601, Dec 1995.

[80] B.G. Klappauf, W.H. Oskay, D.A. Steck, and M.G. Raizen. Quantum chaos with cesium atoms: pushing the boundaries. *Physica D*, 131(1):78–89, 1999.

[81] R. Blümel, S. Fishman, and U. Smilansky. Excitation of molecular rotation by periodic microwave pulses. A testing ground for Anderson localization. *Journal of Chemical Physics*, 84(5):2604–2614, 03 1986.

[82] J. Ni, S. Dadras, W. K. Lam, R. K. Shrestha, M. Sadgrove, S. Wimberger, and G. S. Summy. Hamiltonian ratchets with ultra-cold atoms. *Annalen der Physik*, 529(8):1600335, 2017.

[83] M. Sadgrove, M. Horikoshi, T. Sekimura, and K. Nakagawa. Rectified momentum transport for a kicked Bose-Einstein condensate. *Phys. Rev. Lett.*, 99:043002, Jul 2007.

[84] M. Sadgrove, S. Kumar, and K. Nakagawa. Enhanced factoring with a Bose-Einstein Condensate. *Phys. Rev. Lett.*, 101:180502, Oct 2008.

[85] W. H. Oskay, D. A. Steck, and M. G. Raizen. Timing noise effects on dynamical localization. *Chaos, Solitons and Fractals*, 16(3):409–416, 2003.

[86] S. Diehl, A. Micheli, A. Kantian, B. Kraus, H. P. Büchler, and P. Zoller. Quantum states and phases in driven open quantum systems with cold atoms. *Nature Physics*, 4(11):878–883, September 2008.

[87] S. Diehl, E. Rico, M. A. Baranov, and P. Zoller. Topology by dissipation in atomic quantum wires. *Nature Physics*, 7(12):971–977, October 2011.

[88] D. Witthaut, F. Trimborn, and S. Wimberger. Dissipation induced coherence of a two-mode bose-einstein condensate. *Phys. Rev. Lett.*, 101:200402, Nov 2008.

[89] F. Verstraete, M. M. Wolf, and J. I. Cirac. Quantum computation, quantum state engineering, and quantum phase transitions driven by dissipation, 2008. arXiv 0803.1447.

[90] H. Krauter, C. A. Muschik, K. Jensen, W. Wasilewski, J. M. Petersen, J. I. Cirac, and E. S. Polzik. Entanglement generated by dissipation and steady state entanglement of two macroscopic objects. *Physical Review Letters*, 107(8), 2011.

[91] I. Bloch. Quantum coherence and entanglement with ultracold atoms in optical lattices. *Nature*, 453(7198):1016–1022, June 2008.

[92] M. V. Berry. interview by nina hall: 'caustics, catastro- phes and quantum chaos'. *Phys. Rev. A*, 1997.

[93] C. W. Gardiner. *Stochastic Methods*. Springer, Berlin, fourth edition, 2009.

[94] J. Pitman and M. Yor. A guide to brownian motion and related stochastic processes, 2018. arXiv 1802.09679.

[95] E. M. de Jager. On the origin of the korteweg-de vries equation, 2011. arXiv math/0602661.

[96] S. Jian-Jun. The proper analytical solution of the korteweg-de vries-burgers equation. *Journal of Physics A: Mathematical and General*, 20(2):L49–L56, February 1987.

[97] J Rogel-Salazar. The gross–pitaevskii equation and bose–einstein condensates. *European Journal of Physics*, 34(2):247–257, January 2013.

[98] N. Benedikter, G. de Oliveira, and B. Schlein. Quantitative derivation of the gross-pitaevskii equation. *Communications on Pure and Applied Mathematics*, 68(8):1399–1482, September 2014.

[99] Q. Chauleur. Finite volumes for the gross-pitaevskii equation, 2024. arXiv 2402.03821.

[100] M Abid, C Huepe, S Metens, C Nore, C.T Pham, L.S Tuckerman, and M.E Brachet. Gross–pitaevskii dynamics of bose–einstein condensates and superfluid turbulence. *Fluid Dynamics Research*, 33(5):509–544, 2003. Collection of Papers written by Regional Editors.

[101] HH. Peng, J. Deng, S. Lou, and Q. Wang. High precision solutions to quantized vortices within gross–pitaevskii equation. *Communications in Theoretical Physics*, 74(9):095002, August 2022.

[102] M. P. Kawatra and R. K. Pathria. Quantized vortices in an imperfect bose gas and the breakdown of superfluidity in liquid helium ii. *Phys. Rev.*, 151:132–137, Nov 1966.

[103] N. Pradhan, P. Kumar, R. Kanamoto, T. N. Dey, M. Bhattacharya, and P. K. Mishra. Cavity optomechanical detection of persistent currents and solitons in a bosonic ring condensate. *Phys. Rev. Res.*, 6:013104, Jan 2024.

[104] L. Boßmann and S. Teufel. Derivation of the 1d gross–pitaevskii equation from the 3d quantum many-body dynamics of strongly confined bosons. *Annales Henri Poincaré*, 20(3):1003–1049, November 2018.

[105] F. M. Cucchietti, B. Damski, J. Dziarmaga, and W. H. Zurek. Dynamics of the Bose-Hubbard model: Transition from a Mott insulator to a superfluid. *Physical Review A*, 75(2), February 2007.

[106] J. Kisker and H. Rieger. Bose-glass and mott-insulator phase in the disordered boson hubbard model. *Physical Review B*, 55(18):R11981–R11984, May 1997.

[107] T. Tomita, S. Nakajima, I. Danshita, Y. Takasu, and Y. Takahashi. Observation of the mott insulator to superfluid crossover of a driven-dissipative Bose-Hubbard system. *Science Advances*, 3(12), December 2017.

[108] D. Jaksch, C. Bruder, J. I. Cirac, C. W. Gardiner, and P. Zoller. Cold bosonic atoms in optical lattices. *Phys. Rev. Lett.*, 81:3108–3111, Oct 1998.

[109] R. V. Pai and R. Pandit. Superfluid, Mott-insulator, and mass-density-wave phases in the one-dimensional extended Bose-Hubbard model. *Phys. Rev. B*, 71:104508, Mar 2005.

[110] G. Roux, T. Barthel, I. P. McCulloch, C. Kollath, U. Schollwöck, and T. Giamarchi. Quasiperiodic Bose-Hubbard model and localization in one-dimensional cold atomic gases. *Physical Review A*, 78(2), August 2008.

[111] I. B. Spielman, W. D. Phillips, and J. V. Porto. Mott-insulator transition in a two-dimensional atomic Bose gas. *Phys. Rev. Lett.*, 98:080404, Feb 2007.

[112] P. Anders, E. Gull, L. Pollet, M. Troyer, and P. Werner. Dynamical mean field solution of the Bose-Hubbard model. *Phys. Rev. Lett.*, 105:096402, Aug 2010.

[113] A. Vardi and J. R. Anglin. Bose-Einstein condensates beyond mean field theory: Quantum backreaction as decoherence. *Phys. Rev. Lett.*, 86:568–571, Jan 2001.

[114] W. Koller and N. Dupuis. Variational cluster perturbation theory for Bose–Hubbard models. *Journal of Physics: Condensed Matter*, 18(41):9525, Sep 2006.

[115] B. Capogrosso-Sansone, Söyler, N. Prokof'ev, and B. Svistunov. Monte carlo study of the two-dimensional Bose-Hubbard model. *Phys. Rev. A*, 77:015602, Jan 2008.

[116] P. Barmettler and C. Kollath. Quantum gases in optical lattices, 2013. arXiv 1312.5772.

[117] H. P. Breuer and F. Petruccione. *The theory of open quantum systems.* Oxford University Press, Great Clarendon Street, 2002.

[118] H. M. Price and N. R. Cooper. Mapping the berry curvature from semiclassical dynamics in optical lattices. *Phys. Rev. A*, 85:033620, Mar 2012.

[119] P. Barmettler and C. Kollath. Controllable manipulation and detection of local densities and bipartite entanglement in a quantum gas by a dissipative defect. *Phys. Rev. A*, 84:041606, Oct 2011.

[120] J. Anglin. Cold, dilute, trapped bosons as an open quantum system. *Phys. Rev. Lett.*, 79:6–9, Jul 1997.

[121] M. Trujillo-Martinez, A. Posazhennikova, and J. Kroha. Nonequilibrium josephson oscillations in bose-einstein condensates without dissipation. *Phys. Rev. Lett.*, 103:105302, Sep 2009.

[122] D. Poletti, JS. Bernier, A. Georges, and C. Kollath. Interaction-induced impeding of decoherence and anomalous diffusion. *Phys. Rev. Lett.*, 109:045302, Jul 2012.

[123] H. Pichler, A. J. Daley, and P. Zoller. Nonequilibrium dynamics of bosonic atoms in optical lattices: Decoherence of many-body states due to spontaneous emission. *Phys. Rev. A*, 82:063605, Dec 2010.

[124] H. J. Carmichael. *An open systems approach to quantum optics*. Springer-Verlag, Berlin Heidelberg, 1993.

[125] J. Dalibard, Y. Castin, and K. Mølmer. Wave-function approach to dissipative processes in quantum optics. *Phys. Rev. Lett.*, 68:580–583, Feb 1992.

[126] J. Estève, C. Gross, A. Weller, S. Giovanazzi, and M. K. Oberthaler. Squeezing and entanglement in a bose–einstein condensate. *Nature*, 455(7217):1216–1219, October 2008.

[127] C. Gross. Spin squeezing, entanglement and quantum metrology with bose–einstein condensates. *Journal of Physics B: Atomic, Molecular and Optical Physics*, 45(10):103001, May 2012.

[128] D. T. Smithey, M. Beck, J. Cooper, M. G. Raymer, and A. Faridani. Complete experimental characterization of the quantum state of a light mode via the wigner function and the density matrix: application to quantum phase distributions of vacuum and squeezed-vacuum states. *Physica Scripta*, 1993(T48):35, Jan 1993.

[129] F. Trimborn, D. Witthaut, and S. Wimberger. Mean-field dynamics of a two-mode bose–einstein condensate subject to noise and dissipation. *Journal of Physics B: Atomic, Molecular and Optical Physics*, 41(17):171001, Aug 2008.

[130] I. Tikhonenkov, J. R. Anglin, and A. Vardi. Quantum dynamics of Bose-Hubbard Hamiltonians beyond the Hartree-Fock-Bogoliubov approximation: The Bogoliubov back-reaction approximation. *Phys. Rev. A*, 75:013613, Jan 2007.

[131] G. S. Ng, H. Hennig, R. Fleischmann, T. Kottos, and T. Geisel. Avalanches of bose–einstein condensates in leaking optical lattices. *New Journal of Physics*, 11(7):073045, Jul 2009.

[132] R. Livi, R. Franzosi, and GL. Oppo. Self-localization of Bose-Einstein condensates in optical lattices via boundary dissipation. *Phys. Rev. Lett.*, 97:060401, Aug 2006.

[133] K. Koor, Y. Qiu, L. C. Kwek, and P. Rebentrost. A short tutorial on wirtinger calculus with applications in quantum information, 2023.

[134] D. Lucente, M. Viale, A. Gnoli, A. Puglisi, and A. Vulpiani. Revealing the nonequilibrium nature of a granular intruder: The crucial role of non-gaussian behavior. *Phys. Rev. Lett.*, 131:078201, Aug 2023.

[135] M. Bianucci, M. Bologna, and R. Mannella. Colored stochastic multiplicative processes with additive noise unveil a third-order PDE, defying conventional FPE and Fick-law paradigms, 2024. arXiv preprint 2404.14229.

[136] M. B. d'Arcy, R. M. Godun, M. K. Oberthaler, D. Cassettari, and G. S. Summy. Quantum enhancement of momentum diffusion in the delta-kicked rotor. *Phys. Rev. Lett.*, 87:074102, Jul 2001.

Erklärung

Hiermit versichere ich, dass ich diese Arbeit selbstständig verfasst habe. Während des schreibens hat das in Overleaf integrierte Sprachtool Vorschläge zur besseren Formulierung der Sätze in englischer Sprache gegeben, die ich teilweise übernommen habe. Für die Implementierung der Spntanemissionen im ersten Hauptteil half mir Casper Groiseau mit seiner Expertise. Weiterhin wurden mir zu Beschleunigung des Forschungsprozesses für die Implementierung des offenen Bose-Hubbard Systems und die Implementierung der Truncated-Wigner Methode durch meinen Betreuer Codes vorheriger Studenten bereitgestellt. Diese habe ich für meine Forschungszwecke modifiziert und weiterentwickelt. Neben den angegebenen Quellen und Hilfsmitteln habe ich keine weiteren verwendet.

Heidelberg, den 16 Juli, 2024